Evaluation of Earth gravity field models used for precise satellite orbit determination through applications of Satellite Laser Ranging data

by

Mihloti Christina Botai

Submitted in partial fulfilment of the requirements for the degree

DOCTOR OF PHILOSOPHY

in the Faculty of Natural & Agricultural Sciences

University of Pretoria

Pretoria

South Africa

February 2013

Evaluation of Earth gravity field models used for precise satellite orbit determination through applications of Satellite Laser Ranging data

Author : Mihloti Christina Botai

Supervisor : Prof. Ludwig Combrinck

Department : [1]Department of Geography, Geoinformatics and Meteorology, University of Pretoria, Pretoria 0002, South Africa

: [2]Hartebeesthoek Radio Astronomy Observatory (HartRAO), P.O. Box 443, Krugersdorp 1740, South Africa

Degree : Doctor of Philosophy

Abstract

One of the applications of the Satellite Laser Ranging (SLR) technique is the derivation of gravity field models; these models have various geophysical and geodynamical applications. Gravity field modelling has reached a new era where the latest satellite missions (CHAMP, GRACE and GOCE) are thought to provide significant improvement of global gravity field information in terms of quality and spatial resolution. In particular, the recent satellite missions carry on-board Global Navigation Satellite System (GNSS) receivers, accelerometers, K/Ka-band microwave system (e.g. in GRACE) and gradiometers (e.g. in GOCE) allowing measurements of gravity field with unprecedented accuracy in contrast to the unsteady and fragmented orbit tracking by unevenly distributed SLR ground stations.

Numerous gravity field models have been derived based on the newly available data sets by various research groups globally. Due to the availability of high quality SLR and satellite data, some of the older gravity field models are being updated as new models with higher degree and order are developed. Notwithstanding the significant progress in gravity field modelling, research focusing on assessing the accuracy and precision of the existing gravity field models has largely remained insufficient. The difference between the observed and computed satellite orbit (which is often expressed as the O-C range residuals) is used as a parameter for Precise Orbit Determination (POD) of satellites. Furthermore, O-C range residuals computed during SLR analysis are used as proxy parameters for evaluating the accuracy of gravity field models.

The work presented in this thesis firstly reviewed and evaluated the accuracy of gravity field models released between 1990 and 2008. The accuracy of the gravity field models was examined by analysing the O-C residuals computed from LAGEOS 1 and 2 data analysis based on a set of twelve gravity field models. The results demonstrated that in general, there has been an improvement in the accuracy of gravity field models released between 1990 and 2008 by a factor of 2 based on improvements in the O-C residuals. Additionally, the influence of SLR tide parameterization (the IERS 2010 solid Earth and pole tide models) on the O-C residuals across five gravity field models has been assessed and results illustrate that the solid Earth and pole tides parameterization influence on the O-C residuals is dependent on the type of gravity field model. In order to ascertain the significance of mean differences in the Standard Deviations (SD) of O-C residuals based on the tide parameterization options, the student's *t*-test was used. Results suggest that in general the O-C residuals derived from SLR LAGEOS 1 data have insignificant mean SD differences across the tide parameterizations. On the other hand analysis of SLR observations of LAGEOS 2 resulted in statistically significant mean SD differences in the O-C based on EIGEN-CG03C, EGM2008 and AIUB-GRACE01S gravity field models. The J_2 coefficient forms part of the SLR Data Analysis Software (SDAS) package output products and was investigated in this thesis due to its role in understanding mass-redistribution within the Earth system (i.e. the equatorial bulge due to centrifugal force and rotation). In particular, the J_2 coefficient computed from SLR analysis of LAGEOS 1 and 2 data sets and based on the four selected gravity field models were compared with a priori J_2 coefficients from the four models and those published in the literature. The results indicated that the J_2 coefficients computed from the SDAS package were in agreement with the published coefficients. For geophysical applications, the relationship between the J_2 parameter and LOD and AAM was investigated by use of data adaptive analysis methodology (the empirical mode decomposition). The results demonstrated that some degree of synchronization exists between the signal components of J_2 and LOD and J_2 and AAM.

Keywords: Satellite Laser Ranging tracking, Earth's gravitational field, gravity field models, orbit sensitivity analysis, orbit parameter estimation, J_2 spherical harmonic coefficient.

List of publications

The following contributions have been published and/or in/to various peer review journals as part of this work.

1. Investigating the effect of tide parameterization on the accuracy of gravity field models (Submitted).

2. Analysis of Earth's oblateness and geophysical excitation functions related to polar motion (Submitted).

3. Botai, M.C. and Combrinck, L. Global geopotential models from Satellite Laser Ranging data with geophysical applications: A review. *South African Journal of Science*. 2012:108(3/4); 1-10.

4. Botai, M.C. and Combrinck, L. Investigating the accuracy of gravity field models using Satellite Laser Ranging data. *South African Journal of Geology*, 2011; 114.3-4:539-544.

5. Botai, M.C. and Combrinck, L. Investigating the variability of Earth gravity field's J_2 spherical harmonic coefficient using Satellite Laser Ranging data. 11th SAGA Biennial Technical Meeting and Exhibition, Swaziland, 2009:603-606.

Declaration

I, Mihloti Christina Botai, hereby declare that the work on which this thesis is based, which I hereby submit for the degree Doctor of Philosophy, Faculty of Natural and Agricultural Sciences at the University of Pretoria, is my own work except where acknowledgements indicate otherwise. This work has not previously been submitted by me for another degree at this or any other tertiary institution.

……..

7 February 2013

Dedication

I dedicate my dissertation work to my wonderful family, specially my husband Dr. Joel Botai for his unconditional love, wisdom, patience and support during my PhD research and to our precious children (particularly our daughter, Mong'are Palmira whose little life journey began during the course of my research), you are the joy of our lives. A special dedication goes to my mother and grandfather who passed away during the course of my doctorate work. I also dedicate this dissertation to my supervisor Prof. Ludwig Combrinck for believing in me, without his support and guidance none of this work would have been possible.

Acknowledgements

This thesis is the result of research I carried out at Hartebeesthoek Radio Astronomy Observatory under the Space Geodesy programme while registered at the University of Pretoria. I would like to thank all of those people who helped make this dissertation possible.

- First and foremost I wish to deeply thank my principal adviser, Prof. Ludwig Combrinck for his generous guidance, support and enthusiasm, which made this thesis possible. I dearly thank him for all the patience he has had with me and for the corrections to my scientific errors. This thesis would not be possible if he did not dedicate much time and effort to read my endless drafts and more importantly my intellectual development. Thank you for assistance, encouragement and leadership throughout my graduate study.
- I wish to thank HartRAO for creating an ethical research environment and for giving me an opportunity to work in it.
- I gratefully acknowledge the financial support provided for my academic studies by the National Research Foundation and Inkaba yeAfrica, a joint Germany-South Africa geosciences initiative.
- On a personal note, I wish to thank my late parents who have given me life and always encouraged me to pursue my dreams and to my late grandparents for their love and support during my academic studies.
- Special thanks go to my dear husband, Dr. Joel Botai for the patience, unconditional love and support that he has given me throughout my studies and to our children Nelson, Michael and Palmira for continually inspiring me to do better for our family.
- I also wish to thank my friends Joyce, Johanna and Musa for being there for me throughout the entire doctorate program. You guys have been wonderful people to hang out with and you really helped me stay in touch with the real world, it was a wonderful journey.
- Furthermore, I thank my colleagues, Marion for editing work, Roelf for his kind help with computers during data processing and Marisa for the friendships we have built and wonderful discussions we have had while working together.
- Lastly I thank the Heavenly Father for giving me the ability, courage, perseverance and the will to commence and complete my research.

Table of contents

List of Tables

List of Figures

Acronyms

AAM	: Atmospheric Angular Momentum
BE-B	: Beacon Explorer-B
CDDIS	: Crustal Dynamics Data Information System
CGS	: Centro de Geodasia Spaziale
CHAMP	: CHAllenging Minisatellite Payload
CoM	: Centre-of-Mass
CRF	: Celestial Reference Frame
DORIS	: Doppler Orbitography and Radiolocation Integrated by Satellite
EIGEN	: European Improved Gravity model of the Earth by New techniques
EEMD	: Ensemble Empirical Mode Decomposition
EMD	: Empirical Mode Decomposition
EOP	: Earth orientation parameters
GEM	: Goddard Earth Models
GGM	: Global Geopotential Model
GFZ	: GeoForschungs Zentrum
GLONASS	: Global Orbiting Navigation Satellite System
GNSS	: Global Navigation Satellite Systems
GRACE	: Gravity Recovery and Climate Experiment
GSFC	: Goddard Space Flight Center
GOCE	: Gravity field and steady-state Ocean Circulation Explorer
GPS	: Global Positioning System
HartRAO	: Hartebeesthoek Radio Astronomy Observatory
IAG	: International Association of Geodesy
IERS	: International Earth Rotation and Reference System
ILRS	: International Laser Ranging Service
IMF	: Intrinsic Mode Functions
JCET/GSFC	: Joint Centre for Earth System Technology/Goddard Space Flight Centre
JGM	: Joint Gravity Models

LAGEOS	: LAser GEOdynamics Satellite
LOD	: Length-Of-Day
MSL	: Mean Sea Level
NCAR	: National Center for Atmospheric Research
NCEP	: National Centers for Environmental Prediction
NIMA	: National Imagery and Mapping Agency
O-C	: Observed minus Computed
OSU	: Ohio State University
PGR	: Post-Glacial Rebound
POD	: Precise Orbit Determination
PPN	: Parameterized Post Newtonian
SBA	: Special Bureau for the Atmosphere
SDAS	: SLR Data Analysis Software
SLR	: Satellite Laser Ranging
TAI	: International Atomic Time
TEG	: Texas Earth Gravity
TOF	: Time-Of-Flight
UTC	: Universal Time
VLBI	: Very Long Baseline Interferometry
ZD	: Zenith Delay

1. Introduction

1.1. Background

The gravity field of Earth is a conservative field of force which is constantly changing. In essence, the gravitational potential at an external point is the sum of the gravitational potential, the potential of centrifugal forces and a varying component resulting from tidal effects from the Moon and Sun as well as from the motion of the Earth's poles. The strength and direction of the gravity field exhibits spatial-temporal variations. For example, due to the rotation of Earth, the Earth's gravity field at the poles is not the same as the gravity at the equator. Density, mass re-distribution and dynamics of the Earth's surface are often inferred from the gravity field and its spatial-temporal variability (Chen *et al*., 2005a). The gravity field of Earth plays a significant role in various fields of research such as geophysics, oceanography, hydrology, glaciology, geodesy and solid Earth science. In particular, the gravity field of Earth may be applied in geodynamics for example to observe time varying physical processes such as the post glacial uplift or sea level changes (Rummel *et al*., 2002). In geodesy, the gravity field of Earth may be used for precise satellite orbit determination (Rummel *et al*., 2002; Svehla and Rothacher, 2004).

The gravity field of Earth is often measured by use of geodetic satellite data collected from Satellite Laser Ranging (SLR) observations. These orbiting satellites are affected by both gravitational and non-gravitational accelerations (e.g. atmospheric drag, radiation pressure, etc.). During analysis of SLR observations, spatial-temporal variability and dynamics of the gravity field of Earth are inferred from analysing satellite orbit perturbations induced by the gravity field. A number of gravity field models (expressed as a set of coefficients consisting of a series expansion of spherical harmonics) have been derived since the mid 1960s by use of SLR tracking data and sometimes combined with terrestrial and altimeter data (e.g., Schwintzer *et al*., 1991, Lemoine *et al*., 1998, Foerste *et al*., 2006 and others). Accuracy of these models in terms of precise orbit determination (POD) depends on data availability, quality, type and geographical coverage.

The inherent biases in most of the existing gravity field models have not been extensively studied. These biases could be as a result of utilizing data from satellite missions that were not designed for gravity measurements. This is particularly true in cases where the

orbital parameters of the satellite in question are not suited for accurate gravity field recovery. In addition, SLR measurements often used for gravity field computation (i.e., time of flight measurements) are weather dependent. In most areas, approximately 50% of the time weather conditions such as cloud cover and rain do not allow for laser ranging. Furthermore, terrestrial gravity data and satellite altimeter data may also bias some of the gravity field models (e.g., the combined and tailored category of the gravity field models) since the geometry of the observations is not uniform (the data are not globally distributed). Difficulties in modelling the non-gravitational forces of most of the geodetic satellites (in particular the low Earth orbits) also limit the plausibility of achieving significant improvement in gravitational field modelling.

Nowadays the use of the on-board GPS/gradiometer receiver from the latest satellite missions (CHAMP, GRACE and GOCE) allows POD with unprecedented accuracy and almost complete spatial and temporal coverage. The data collected from these missions have resulted in the determination of a variety of new global gravity field models (e.g., EIGEN1, AIUB-CHAMP01S, EIGEN-CG04S, AIUB-GRACE01S, EIGEN-5C and many others) as well as updating the old gravity field models (e.g., EGM96 to EGM2008 and EIGEN-CG01C to EIGEN-CG03C, EIGEN-1S to EIGEN-6S, GGM02C to GGM03C, AIUB-GRACE01S to AIUB-GRACE013S). Today there are more than 100 global geopotential models (GGMs) derived by different research groups around the world. The ongoing development of geopotential models could be attributed to the availability of new data sets (with high quality and quick turn-around time) particularly from the recent advanced satellite missions as well as the SLR tracking data of multiple satellites.

Furthermore, development and improvement in gravity field modelling is anticipated as quantitative data become available in the future due to improvement of SLR technology. In particular, the employment of longer data spans from CHAMP, GRACE and GOCE with advanced processing software algorithms and empirical models are expected to increase the resolution and further improve the accuracy in gravity field models. Furthermore, the existence of numerous satellite missions not necessarily dedicated to gravity field research (e.g., COSMIC and SWARM missions) but equipped with space-borne GPS receivers are expected to contribute to the development of more accurate gravity field models (Prange *et al.*, 2008). These expectations however require that the accuracy and precision of existing gravity field models be assessed and validated. The research reported in this thesis focuses on investigating the accuracy

of different gravity field models using a new SLR analysis software package developed at Hartebeesthoek Radio Astronomy Observatory (HartRAO); it was named SLR Data Analysis Software (SDAS) by Combrinck (2010). The SDAS package was developed based on a modified spacecraft dynamics library provided by Montenbruck and Gill (2001). Some of its technical details are reported in Combrinck and Suberlyak, (2007). The software was designed by Combrinck (coding started in August 2004) and has been significantly updated and modified by him since the initial application report of 2007, and has been specifically modified to allow testing of different gravitational models.

1.2. Significance of the research

The International Laser Ranging Service (ILRS) has continued to make SLR observation data sets available to the scientific community (about four decades of data) since its formation in 1998. This service coordinates its operations, data dissemination and analysis through working groups, data and analysis centres. Unfortunately, none of the SLR analysis, lunar and associate analysis centres are in Africa. This research effort is a demonstration of preparedness towards the development of the first SLR analysis centre on the African continent. To analyse SLR data particularly for POD and geodetic parameter estimation only a few known software packages such as NASA/GSFC GEODYN II (Pavlis *et al*., 1999; Pavlis *et al*., 2006), NASA/GSFC SOLVE software, SATellite ANalysis (SATAN) software (Sinclair and Appleby, 1986), GFZ analysis software package EPOSOC and the University of Texas Orbit Processor (UTOPIA) are currently widely used by the analysis centres. However, the SDAS package (which is continuously updated and improved) will have to be augmented with several algorithms before it can be used to participate as an ILRS analysis centre, in order to produce standard analysis centre products, such as Earth Orientation Parameters (EOPs). These upgrades are in progress and new features are regularly added.

A number of gravity field models have been developed based on a combination of SLR, terrestrial and satellite altimeter data since the mid 1960s. The progressive development of gravity field modelling is often characterized by an improvement in spatial and temporal resolution and by the increased degree and order (of the spherical harmonics) of a geopotential field. Some of the new gravity field model developments (i.e. those models derived from CHAMP and GRACE satellite data) are followed by a validation phase that is often limited

spatially. Despite the continuous gravity field model development, research on the over-all accuracy of these models has not been reported. The present research contributes towards investigating the accuracy of some of the selected gravity field models and model categories (e.g. satellite-only, combined and tailored gravity field models). In general, the scientific contribution of the research reported in this thesis is particularly relevant to the SLR community, space geodesy and in general to Earth system science.

1.3. Aim and objectives

The overall aim of the present research is to study the accuracy of various gravity field models based on the SLR analysis software developed at HartRAO. In particular the LAser GEOdynamics Satellite (LAGEOS) 1 and 2 SLR data sets were considered in calculating the SLR range residuals i.e. the Observed-Computed (O-C) residuals. The specific objectives of this project were to:

- Analyse the historical development of gravity field models
- Calculate the range residuals using the SLR analysis software developed at HartRAO based on different geopotential models
- Investigate the accuracy of selected gravity field models using LAGEOS 1 and 2 data
- Investigate the contributions of Earth and pole tides on the O-C range residuals across selected gravity field models by use of different tide parameterization in the SDAS package.
- Compare the SDAS estimated J_2 with those published in the literature as well as investigating possible association of the J_2 coefficient with other geophysical parameters such as atmospheric and ocean angular momentum and the length of day.

1.4. Outline of the thesis

This thesis consists of seven chapters. In Chapter 2 an overview of space geodetic techniques is provided focussing on the SLR observational technique and its scientific applications. The data and methods used (analysis strategy) for data processing are described in Chapter 3. Chapter 4 contains the results of studies on the general improvement in gravity field modelling. In addition, results on the accuracy of gravity field models based on POD are presented. A

sensitivity analysis study is presented in Chapter 5. In Chapter 6 the J_2 coefficient estimated by the SDAS package from EGM96, GRIM5C1, GGM03C and AIUB-GRACE01S gravity field models is compared with the a priori J_2 for the four models. Furthermore, a linkage between J_2 and geophysical parameters, the length-of-day and atmospheric angular momentum was assessed. Lastly, Chapter 7 summarizes the research carried out, highlights research findings and provides recommendations for further research.

2. Space geodetic techniques and their data applications

To know the history of science is to recognize the mortality of any claim to universal truth, Evelyn Fox Keller, 1995.

2.1. Introduction

The launch of artificial satellites as early as 1957 has presented an unprecedented prospect of using the long period of available satellite data to study the size, shape and rotation of Earth as well as the variations in the Earth's gravity field. This is known as the three pillars of geodesy[1] (geokinematics, rotation and gravity field) in modern geodesy. In particular, the use of satellites for geodetic applications led to the development of satellite geodesy[2]. Satellite geodesy observations are achieved through space based techniques, particularly SLR and satellite positioning (e.g., Global Navigation Satellite Systems (GNSS)). The SLR technique measures the travel time (converted to range and corrected for a number of range delay parameters) of a transmitted laser pulse from the ground tracking station to the orbiting satellite in space and back to the ground station with an accuracy of approximately a centimetre. Applications of SLR measurements include the determination of the Earth's gravity field, monitoring of motion of the tracking station network with respect to the geocentre as well as calibration of geodetic microwave techniques (e.g. calibration of satellite orbits where the satellites are equipped with radar altimeters). On the other hand satellite based positioning and navigation systems, in particular the Global Positioning System (GPS), have opened unlimited possibilities for its use e.g. in geodetic control surveying and navigations (Seeber, 2003). For example, GPS data have been used for precise land navigation and have contributed to the establishment of precise geodetic control and the determination of GPS elevations above sea level.

Very Long Baseline Interferometry (VLBI), a technique which was developed in the late 1960's, has been broadly used in various fields of geodynamics such as global plate tectonic measurements and studies of variations in the Earth's rotation (Ryan *et al.*, 1993; Eubanks *et al.*, 1993). This technique has also resulted in the establishment and maintenance of an accurate and

[1] Geodesy can be defined as the science that determines the size and shape of the earth, the precise positions and elevations of points, and lengths and directions of lines on the Earth's surface, and the variations of terrestrial gravity (definition adopted from the International Association of Geodesy (IAG)).
[2] Satellite geodesy is a branch of geodesy which is concerned with satellite orbits, motion, perturbations and satellite based positioning (Seeber, 2003).

stable inertial (celestial) reference system which replaced the fundamental star catalogues. Here, a catalogue of Quasars (stable and distant radio sources) is used for defining the International Celestial Reference Frame (ICRF). The three techniques (SLR, GNSS and VLBI) together with Doppler Orbitography and Radio positioning by Satellites (DORIS) and even the Lunar Laser Ranging (LLR) technique, are the precise geodetic measurement methods and are often referred to as space geodetic methods or techniques (Koyama *et al.*, 1998). Space geodetic techniques are the fundamental tools for modern geodesy whose scope encompasses the provision of services to both society and the scientific community. Since these techniques have different characteristics in many aspects, it is preferred to collocate them (locate them on the same site) in order to compare the different and independently obtained results with each other thus improving their individual reliability. In this chapter the key space geodetic milestones are described and then a brief discussion of the principle and the main observables of the three space geodetic techniques (i.e., SLR, VLBI and GNSS) follow. A detailed focus is given to the SLR technique since it is used in this study. Here the discussion includes the properties of SLR, modelling factors that affect the accuracy of SLR measurements and some applications.

2.2. Milestones in space geodesy

Going back in history, geodesy together with its counterparts e.g. surveying, positioning and navigation merely meant measuring of angles as shown in Figure 1. To achieve such measurements the scale was roughly introduced by known distances between two sides of interest. Measurements using cross-staffs were often used to perform relative, local and absolute positioning (Beutler, 2004). A cross-staff is a mechanical device used to measure the angle between two objects (e.g., stars), see for example Figure 2. Historically the cross-staff was used in navigation to help sailors orient themselves, astronomers to study the sky, and by surveyors interested in taking accurate measurements. The cross-staff consists of a long pole with a series of markings and a sliding bar mounted at a perpendicular angle called a transom. To use a cross-staff, the navigator would position the end of the pole on the cheek just below the eye, and pick two objects to sight to, such as the horizon and the Sun. The navigator would then slide the transom along the cross-staff until one end lines up with one object and the opposite end lines up with the other object. Once the transom is in position, the marking covered by the transom

indicates the angle between the two objects, which can be used to calculate latitude and to collect other information.

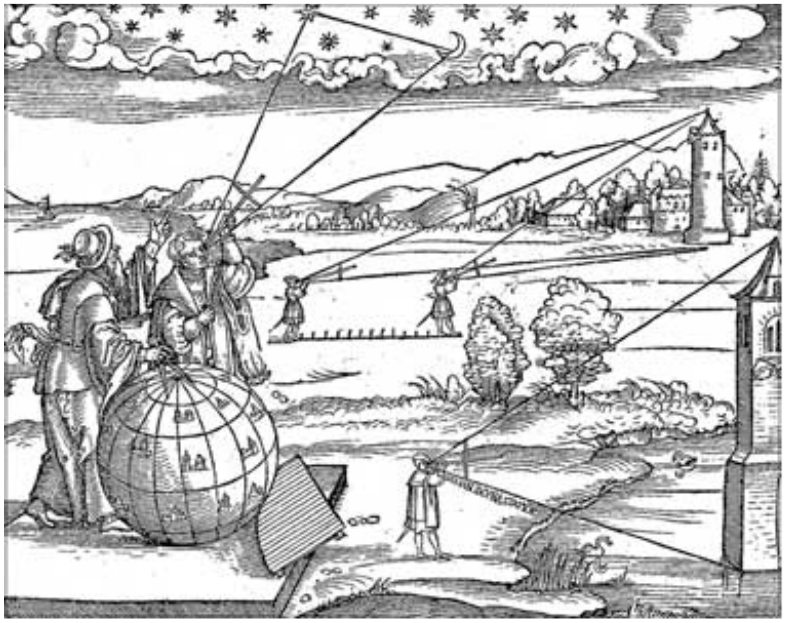

Figure 1. Historical technique of geodesy, surveying, positioning and navigation. Source: http://www.reformation.org.

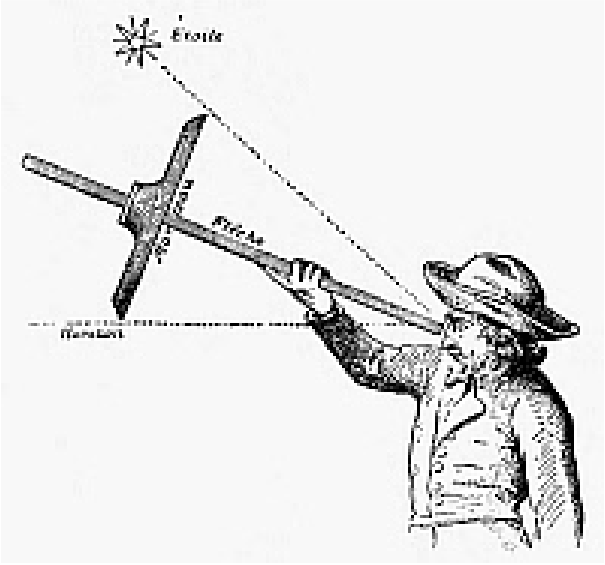

Figure 2. Cross-staff. Source: http://www.granger.com.

The geographical latitude of a site could be established by determining the elevation of the Sun or the polar star Polaris[3] and then looking up the latitude from a pre-calculated table. On the other hand, the longitude was determined by calculating the time difference between the unknown site and Greenwich (0° longitude). The time difference parameter was normally derived either by observing the Sun and measuring the local solar time or by observing certain stars and measuring their sidereal time. Problems related to the realisation of Greenwich time at the unknown observing time were solved by measuring lunar angular distances, lunar distances and angles between bright stars and the Moon. Increased accuracy in lunar orbit prediction allowed angular distances between the Moon and stars to be precisely predicted and tabulated in astronomical and nautical almanacs as a function of Greenwich local time (Beutler, 2004).

The development of new instruments such as marine chronometers (these are highly accurate clocks kept aboard ships and used to determine longitude through celestial navigation) resulted in dramatic improvement in navigation accuracy (Beutler, 2004). For instance, the cross-staff method was quickly replaced by more sophisticated optical devices which included telescopes. This innovative development allowed the determination of more accurate star fundamental catalogues and improvement in predicting motion of planets. Disciplines of fundamental astronomy emerged from the interaction between positioning, navigation, geodesy and surveying. Under such disciplines the terrestrial reference system was realized based on the geographical coordinates of a network of astronomical observatories with an accuracy of about 100 m (Beutler 2004). On the other hand the celestial reference frame was realized by using the derived-fundamental catalogues of stars. The transformation between the terrestrial reference and celestial reference frames enabled the monitoring of Earth rotation in inertial space and on the Earth's surface. Such monitoring revealed that the motion of the Earth's rotation exhibited short periodic variations. For example the Length-Of-Day (LOD) was noticed to slowly increase by about 2 ms per century. In addition, discoveries of the Earth's rotation axis moving on the Earth's surface (these are polar motion effects) were also reported in the literature. Historically, surveying and navigational equipment were too inaccurate to measure observables such as changes in LOD or polar motion, but as equipment and techniques improved, it was quickly

[3] Polaris is a bright star situated close to the North Celestial Pole (http://solar.physics.montana.edu). This type of star never rises or sets as the night progresses, but instead seems to be glued to the sky and is always in the North. So if one is lost in the Northern Hemisphere, one can always figure out direction by finding Polaris.

determined that the dynamics of the rotation of the Earth was not simply a case of undisturbed slow and predictable rotation.

The determination of the Earth's gravitational field also plays an essential role in geodesy and surveying. In the pre-space geodesy era, the gravity field of Earth was determined solely by *in situ* measurements on or near the surface of the Earth. Terrestrial instruments, which included gravimeters[4] and zenith cameras, were developed for gravity field measurements. These instruments however were suited for modelling the local as well as regional properties of the Earth's gravitational field. The desire to model the global properties of the gravity field of the Earth resulted in the development of satellite gravity missions. The use of artificial satellite missions led to the development of satellite geodesy (Kaula, 1966). Today there are four primary techniques, namely SLR, VLBI, GNSS and DORIS that are used in space geodetic observations for the purpose of studying the size, figure and deformation of the Earth and determination of its gravity field and the field's spatial and temporal variations. Apart from scientific interest, contributions from space geodetic techniques may also be applied in most societal areas ranging from disaster prevention and mitigation, to the provision of resources such as energy, water and food and also gaining an understanding of climate change.

2.3. Modern space geodetic techniques

Space geodetic techniques which include SLR, GNSS and VLBI and DORIS are fundamental tools of geodesy. Principles and properties of GNSS, VLBI and SLR methods are briefly reviewed in the following sections. For more information on DORIS the reader is referred to the following published literatures, Gambis (2004), Willis *et al*. (2006) and Coulot *et al*. (2007).

2.3.1. GNSS observable

Global Navigation Satellite System is a term used to describe a group of satellite based navigation systems that allow for the determination of positions anywhere on Earth. Currently the most commonly used GNSS consist of three main satellite technologies: the American controlled GPS, the Russian controlled Global Orbiting Navigation Satellite System (GLONASS) and the European GALILEO system. Each of these satellite systems consists

[4] A gravimeter is a specialized type of accelerometer designed for measuring the local gravitational field of the Earth (Zolfaghari and Gharebaghi, A., 2008).

mainly of three segments: (a) space segment, (b) control segment and (c) user segment (Aerospace Corporation, 2003). The GPS is the most utilized system for positioning, navigation and timing purposes and GPS satellites act as reference points from which receivers on the ground determine their positions. The navigation principle is based on the measurement of pseudo ranges between the user and at least three satellites. Ground stations precisely monitor the orbit of every satellite by measuring the travel time of the signals transmitted from the satellite distances between receiver and satellites. Resulting measurements include position, direction and speed.

In GNSS observations, measurements are often carried out using pseudo-range (or code range) and carrier phase. The primary observable is the phase measurement, which has applications in high precision positioning. Code or pseudo-range measurements are derived from the time difference between signal reception at receiver r and signal transmission at satellite, s. The time of signal transmission is equal to the time of reception less the signal travel time. Generally, the basic code observation equation is reported in Verhagen (2005) and is given by Equation (1)

$$P^{s}_{r,j}(t) = c\left[t_r(t) - t^{s}(t - \tau^{s}_{r,j})\right] + e^{s}_{r,j}(t), \qquad (1)$$

where $P^{s}_{r,j}$ is the code observation at receiver r from satellite s on frequency $j[m]$, t is the time observation in GPS time $[s]$, c is the speed of light in vacuum $[m/s]$, t_r is the reception time at receiver $r[s]$, t^{s} is transmission time from satellite $s[s]$, τ is the signal travel time $[s]$ and e the code measurement error. Since the receiver clock time and satellite clock time are not exactly equal to GPS time, the respective clock errors dt_r and dt^{s} ought to be accounted for as described in Equation (2)

$$t_r(t) = t + dt_{r(t)}$$
$$t^{s}(t - \tau^{s}_{r}) = t - \tau^{s}_{r,j} + dt^{s}(t - \tau^{s}_{r}). \qquad (2)$$

Substituting this Equation (1) yields

$$P^{s}_{r,j}(t) = c\tau^{s}_{r,j} + c[dt_r(t) - dt^{s}(t - \tau^{s}_{r})] + e^{s}_{r,j}(t). \qquad (3)$$

Correcting $\tau^{s}_{r,j}$ for instrumental delays at the satellite and the receiver as well as for atmospheric effects and multipath effects yield

$$\begin{aligned}\tau^{s}{}_{r,j} &= \delta\tau^{s}{}_{r,j} + d_{r,j} + d^{s}{}_{r,j} \\ \delta\tau^{s}{}_{r,j} &= \frac{1}{c}\left[\rho^{s}{}_{r} + da^{s}{}_{r,j} + dm^{s}{}_{r,j}\right],\end{aligned} \tag{4}$$

where $\delta\tau$ is the signal travel time from satellite antenna to receiver antenna $[s]$, d_r is the instrumental code delay in receiver $[s]$, d^s the instrumental code delay in satellite $[s]$, ρ the geometric distance between satellite and receiver $[m]$, $[da]$ the atmospheric code error and dm is the code multipath error $[m]$. With these corrections, the generalized code observation equation (see Verhagen, 2005) becomes

$$\begin{aligned}P^{s}{}_{r,j}(t) = \rho^{s}{}_{r}(t, t-\tau^{s}{}_{r}) + da^{s}{}_{r,j}(t) + dm^{s}{}_{r,j}(t) + \\ c[dt_r(t) - dt^{s}(t-\tau^{s}{}_{r}) + d_{r,j}(t) + d^{s}{}_{,j}(t-\tau^{s}{}_{r}] + e^{s}{}_{r,j}(t).\end{aligned} \tag{5}$$

Phase observation is a very precise but ambiguous measure of the geometric distance between a satellite and the receiver. Phase measurement equals the difference between the phase of the receiver-generated carrier signal at reception time, and the phase of the carrier signal generated in the satellite transmission time. The basic carrier phase observation equation is given by Equation (6)

$$\varphi^{s}{}_{r,j}(t) = \varphi_{r,j}(t) - \varphi^{s}{}_{r,j}(t-\tau^{s}{}_{r}) + N^{s}{}_{r,j} + \varepsilon^{s}{}_{r,j}(t). \tag{6}$$

Here φ is the carrier phase observation [cycles], N is an integer carrier phase ambiguity and ε is the phase measurement error. The phases on the right hand site simplify as expressed in Equation (7)

$$\begin{aligned}\varphi_{r,j}(t) &= f_j t_r(t) + \varphi_{r,j}(t_0) = f_j(t + dt_r(t)) + \varphi_{r,j}(t_0) \\ \varphi^{s}{}_{,j}(t) &= f_j t^{s}(t-\tau^{s}{}_{r}) + \varphi^{s}{}_{,j}(t_0) = f_j(t - \tau^{s}{}_{r,j} + dt^{s}(t-\tau^{s}{}_{r})) + \tau^{s}{}_{,j}(t_0).\end{aligned} \tag{7}$$

Here, f is the nominal carrier frequency $\left[s^{-1}\right]$, $\varphi_r(t_0)$ is the initial phase in the receiver at zero time [cycles] and $\varphi^s(t_0)$ is the initial phase in the satellite at zero time [cycles]. Inserting these expressions the carrier phase observation equation becomes

$$\varphi^{s}{}_{r,j}(t) = f_j\left[\tau^{s}{}_{r,j} + dt_r(t) - dt^{s}(t-\tau^{s}{}_{r}\right] + \left[\varphi_{r,j}(t_0) - \varphi^{s}{}_{,j}(t_0)\right] + N^{s}{}_{r,j} + \varepsilon^{s}{}_{r,j}(t). \tag{8}$$

Multiplying this equation with the nominal wavelength of the carrier signal

$$\phi_j = \lambda_j \varphi_j \qquad \text{with} \quad \lambda_j = \frac{c}{f_j}, \tag{9}$$

yields the carrier phase observation equation in meters as

$$\begin{aligned} \phi^s{}_{r,j}(t) = \rho^s{}_r(t, t-\tau^s{}_r) + \delta a^s{}_{r,j}(t) + c\left[dt_r(t) - dt^s(t-\tau^s{}_r) + \delta_{r,j}(t) + \delta^s{}_{,j}(t-\tau^s{}_r\right] \\ + \left[\phi_{r,j}(t_0) + \phi^s{}_{,j}(t_0)\right] + \lambda_j N^s{}_{r,j} + \varepsilon^s{}_{r,j}(t). \end{aligned} \tag{10}$$

2.3.2. The VLBI observable

Very Long Baseline Interferometry (VLBI) as a technique measures the delay in the arrival times of radio signals produced by a distant source being monitored simultaneously at two terrestrial antennas; see for example schematic representation in Figure 3. The time difference between the arrivals of the signal at each radio telescope is derived by correlation (at the correlator). These time delays and/or its derivative are used to calculate precisely the distance and direction of the baselines between the telescopes. Extragalactic objects that generate radio signals are often considered as point sources due to their great distance. In practice, for the purpose of geodetic VLBI, these sources (quasars) are carefully selected to ensure that they exhibit low proper motion and minimal source structure, so as to appear fixed and point-like. When this happens the time dependence of the time delay is generated via the Earth's motion, although it is dependent on the source location and the baseline vector between the two antennas.

In VLBI measurements the main observed quantities include the geometric delay, phase delay, group delay, the delay rate, and correlated amplitude. The geometric delay is directly related to the fringe phase as a function of frequency. It is as a result of the combination of the geometry of baseline and the direction to the radio source. Mathematically this delay observable can be described as in Tanir *et al.* (2006) and is expressed in Equation (11)

$$\tau_g = -\frac{1}{c}\vec{B}\cdot\vec{k}, \tag{11}$$

where c is the speed of light, $\vec{B}$ is the baseline vector between two stations and $\vec{k}$ is the unit vector towards the observed source. The baseline vector $\vec{B}$ can be transformed between the terrestrial geocentric system and celestial geocentric system. Such a transformation may be formulated as in Tanir *et al.* (2006) and is described as per Equation (12)

$$\vec{B}_c(t) = PNUXY\vec{B}_T(t). \tag{12}$$

In Equation (12) $\vec{B}_c(t)$ is the baseline vector in the celestial system and $\vec{B}_T$ is the baseline vector in the terrestrial system. In addition, (P,N,U,X,Y) represents a transformation term with respect to the Earth orientation parameters, e.g. precession and nutation model, a priori information for Earth rotation $(UT1)$ and polar motion (x_p, y_p). The baseline vector in the terrestrial reference frame takes into account corrections for: solid Earth tides, plate tectonics, ocean tide loading, atmospheric loading, hydrological loading, ionospheric correction, tropospheric correction and clock correction. Taking into consideration these corrections for geometric delay and transformation between the celestial and terrestrial system the geometric delay equation may be rewritten as

$$\tau_{obs} = -\frac{\vec{B}_T}{c} YXUNP\vec{k}_c + \tau_{tides} + \tau_{p.tect} + \tau_{o.load} + \tau_{h.load} + \tau_{ion} + \tau_{trop} + \tau_{clock} \ldots . \tag{13}$$

Here, τ_{obs} is the observed geometrical delay, B_T corresponds to the baseline vector in the terrestrial system and k_c is the source vector in the celestial system.

The phase delay is given by the ratio of the observed fringe phase and the reference angular frequency,

$$\tau_\phi = \frac{\phi_T}{2\pi\nu} + \frac{n}{\nu}. \tag{14}$$

where n is an unknown integer. The group delay is the derivative of the fringe phase with respect to angular frequency and is described by Equation (15)

$$\tau_G = \left(\frac{1}{2\pi}\right) \times \left(\frac{\partial \phi_T}{\partial \nu}\right). \tag{15}$$

The phase delay rate is defined as time rate of change of the phase delay and is given by Equation (16)

$$\dot{\tau} = \frac{\partial \tau_\phi}{\partial t} = \left(\frac{1}{2\pi\nu}\right) \times \left(\frac{\partial \phi_T}{\partial t}\right). \tag{16}$$

The correlated or visibility amplitude of the radio source signal is given by Equation (17)

$$V = \left(\frac{S_c}{S_t}\right). \tag{17}$$

Here, S_c is the correlated amplitude and S_t is the total amplitude or total flux.

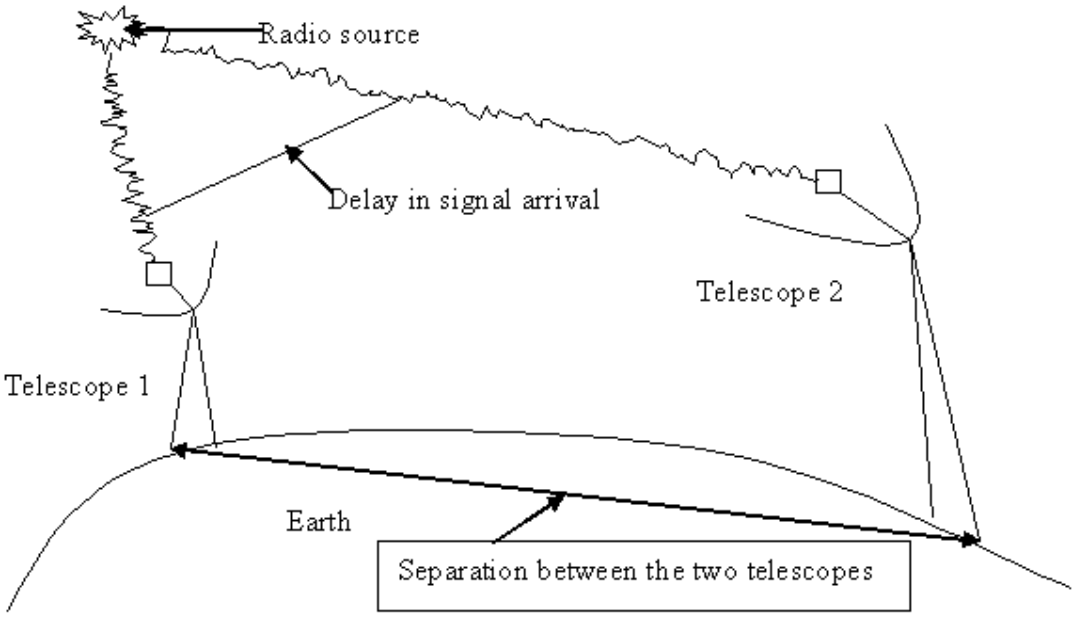

Figure 3. Schematic representation of VLBI concept.

2.3.3. SLR observable

Satellite Laser Ranging (SLR) is a technique that measures the two-way travel time of a short laser pulse which is reflected by an orbiting satellite. This method of measurement is applied to orbiting satellites equipped with special mirrors known as retro-reflectors (which are made from glass prisms). A schematic diagram illustrating the operation of a typical SLR system is presented in Figure 4. In a typical SLR system, a transmitting telescope emits short laser pulses with energy between 10 and 100 mJ at a pulse repetition frequency ranging between 5 and 20 Hz. Some modern systems have lower power levels and higher firing rates up to 2 kHz. The emitted laser pulse has a typical duration of two hundred or less picoseconds, most often specified by the Full Width Half Maximum (FWHM) of the pulse.

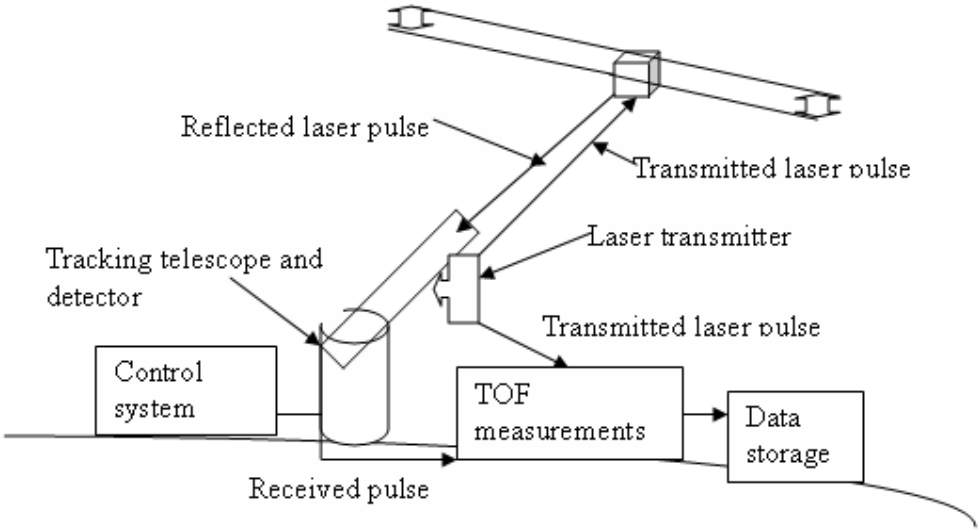

Figure 4. Schematic representation of a typical SLR system (adopted from Degnan, 1985).

Laser pulses propagate through the atmosphere to the orbiting satellite. Pulses which illuminate any of the retro-reflectors are reflected back through the atmosphere to the ground station were they are collected via the receiving telescope. The receiving telescope collects and focuses the reflected pulse energy onto a transmission photocathode (radiation sensor located inside a vacuum envelope of a photomultiplier) device of a photomultiplier (or a Single-Photon Avalanche Diode (SPAD)). A photomultiplier is a versatile and sensitive detector of radiant energy in the ultraviolet, visible, and near infrared regions of the electromagnetic spectrum.

When photons enter the glass vacuum tube, they impinge on the photocathode. The electron yield of this effect depends on the material of the cathode and is quantified as the ratio of emitted electrons to the number of incident photons. This is called the quantum efficiency, ε, and for SLR systems the efficiency is typically on the order of 10-15 percent (Degnan, 1985), a recently developed PMT with GaAsP photocathode and gating option (Hamamatsu R5916U-64) has a quantum efficiency of ~ 40% . Photoelectrons are emitted and directed by an appropriate electric field to an adjacent electrode or dynode within the envelope. As a result of the acceleration between the dynodes, the number of emitted electrons multiplies from step to step (this is similar to a cascading process). A number of secondary electrons are emitted at the dynode for each impinging primary photoelectron. These secondary electrons in turn are directed to a second dynode and so on until a final gain of perhaps 10^6 is achieved. The electrons

from the last dynode are collected by an anode which provides the signal current that is read out. This signal current which represents the round-trip Time-Of-Flight (TOF) of the pulse is stored by the system computer along with other information such as station positions and its velocities.

A basic equation representing an approximate TOF is given by Equation (18)

$$d = \frac{c \times t}{2}, \tag{18}$$

where c is the speed of light and t is the TOF. The speed of light is the signal propagation speed and a factor of two is included to reduce the round trip distance to the one way range. In order to obtain the best possible range precision[5] from the ground station to the satellite numerous corrections corresponding to internal delays in the transmission and detection systems are to be taken into account. Considering such parameter corrections Equation (18) can be expanded into Equation (19)

$$d = \frac{1}{2} c\Delta t + \Delta d_0 + \Delta d_s + \Delta d_b + \Delta d_r + \eta. \tag{19}$$

In Equation (19), Δt is the measured TOF and is mostly affected by uncertainties in the signal identification. The preferred resolution for the measured TOF is often a few picoseconds. In addition, the measured TOF needs to be tied to universal time (because of the satellite's motion relative to the Earth). The Δd_0 term corresponds to the eccentric correction on the ground, which is the intersection of the vertical axis and horizontal axis and is used as a reference point in the laser system. Similarly, Δd_s corresponds to the eccentric correction at the satellite and gives a geometrical relationship between the centre of each corner cube and the centre of mass (COM) of the satellite. The ILRS has COM corrections for different satellites and different laser frequencies (e.g. 1.01 m for AJISAI (Sasaki and Hashimoto, 1987) and 0.251 m for LAGEOS 2 (Minott *et al.*, 1993)). The Δd_b term in Equation (19) corresponds to the signal delay in the ground system. The geometric reference point and the electrical reference point is often not exactly at the same physical point; this correctional parameter is often determined through calibration with older systems that were calibrated with respect to a defined terrestrial target. The electrical delay and optical delay must be measured and constantly checked afterwards, to ensure that system dependent changes do not adversely affect measurement accuracies.

[5] Range precision refers to the degree of agreement of repeated measurements of the same property expressed quantitatively as the standard deviation computed from the results of a series of measurements.

Furthermore, Δd_r is the refraction correction as a result of atmospheric conditions which affect the propagation velocity of laser pulses. Laser pulses experience a delay in the lower part of the atmosphere, which makes measurements of these parameters along the total path difficult. Therefore atmospheric models are used that incorporate variables such as SLR site pressure and temperature and are supported by measured data at the laser site. Lastly, η are random systematic and observation errors related to un-modelled residual effects.

3.3.3.1. Historical development of SLR

The first SLR experiment campaign began in the 1960s with the development of the first (Ruby based) SLR station tracking satellites such Beacon Explorer-B (BE-B) (Osorio, 1992). Since then numerous satellite missions have been launched for different applications such as geodetic, Earth sensing and radio navigation and a global network of SLR stations has been established, replacing the old Baker-Nunn optical camera (Combrinck, 2010). A historical overview of such missions is summarised in Table 1.

Table 1. Timeline of artificial satellites which were tracked by global SLR stations.

Name	Launch date	Height (km)	Mission application
Starlette	1975	960	Gravity, tides, orbit determination
Lageos 1	1976	5900	Earth rotation, gravity, orbit, crustal deformation
Ajisai	1986	1500	Crustal deformation, gravity, orbit determination
Etalon 1/2	1989	19100	Crustal determination, Earth rotation
ERS-1	1991	780	Altimetry, orbit determination
Lageos 2	1992	5900	Crustal deformation, gravity, orbit determination
Stella	1993	810	Gravity, tides, orbit determination
ERS-2	1995	785	Altimetry, orbit determination
GFO-1	1998	800	Oceanography
CHAMP	2000	454	Gravity field, orbit determination
GRACE	2002	485	Gravity field, orbit determination
Larets	2003	691	Orbit determination
GOCE	2009	295	Gravity field, geoid

3.3.3.2. Global network of SLR stations

The current global network of SLR stations involved in artificial satellite tracking consists of over 40 stations and their global distribution is depicted in Figure 5. Most of the SLR tracking stations are located in the Northern Hemisphere leaving the Southern Hemisphere with weak

coverage. In Africa there are two stations, Helwan in Egypt and MOBLAS-6 (see Figure 6) located at HartRAO in South Africa. The space geodetic fundamental station HartRAO is involved with the International Laser Ranging Service (ILRS) activities as well as the other services of the International Association of Geodesy (IAG). This SLR tracking station is relatively isolated in Africa and more active than Helwan, hence plays a very important role as far as data coverage is concerned.

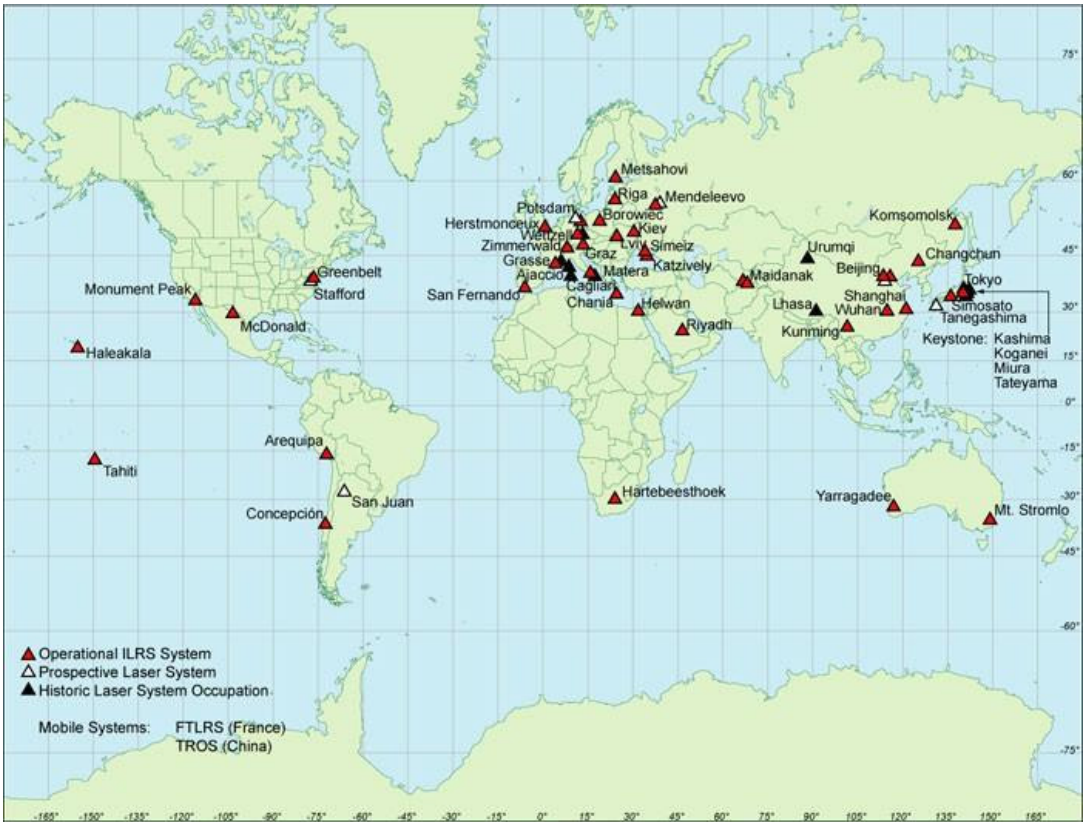

Figure 5. ILRS tracking network. Source: http://www.nasa.gov.

Figure 6. MOBLAS-6 at HartRAO. Source: http://www.hartrao.ac.za.

2.4. Modelling strategies in SLR

2.4.1. Forces acting on an orbiting satellite

2.4.1.1. Two-body problem

The two-body problem addresses the relative dynamics of two point masses attracted to each other by gravity. Its concept in SLR is primarily equivalent to modelling the forces of the motion between two gravitating masses, M and m (e.g., satellites around the Earth). In particular, the two-Body problem is founded on the assumptions that:

- the motion of the spacecraft is governed by attraction to a single central body,
- the central body and satellite are both homogeneous spheres or points of equivalent mass and
- only gravitational forces act on the bodies.

From Newton's law of gravitation, the force F on mass m orbiting about a spherically symmetrical body of mass M at distance r from the centre of mass is defined by Equation (20) as reported in Seeber (2003),

$$F = -\frac{GMm}{r^2}. \tag{20}$$

Here G is the gravitational constant.

Under the basic assumptions of the two-body problem the corresponding vector acceleration following Newton's second law of motion is given by Equation (21),

$$\ddot{r} = -\frac{G(M+m)}{r^3}\vec{r}, \tag{21}$$

where the vector from the centre of mass of the central body to the satellite is given by $\vec{r}$, M is the mass of the central body and m is the mass of the satellite. In addition, assuming that M is the main attracting mass and the mass of the satellite, m is extremely small such that compared to the central body M (e.g., $m \leq M$) the acceleration vector may be written as in Equation (22),

$$\ddot{r} = -\frac{GM}{r^3}\vec{r}. \tag{22}$$

Equation (22) can be solved through an analytical integration method to yield the position and velocity of mass m at future epochs. This is possible only if the initial conditions of position and velocity are known. In a case where perturbing forces act on an orbiting satellite then the satellite will experience additional accelerations due to the perturbing forces. In such case, the equation of motion may be written as in Equation (23),

$$\ddot{r} = -\frac{GM}{r^3}\vec{r} + \sum k_s, \tag{23}$$

where $\vec{r}$ is the position vector of the centre of mass of the satellite and k_s is a perturbing vector (which is in general the summation of all the perturbing forces acting on an orbiting satellite) and can be expressed as in Equation (24)

$$k_s = \bar{a}_g + \bar{a}_{ng} + \bar{a}_{emp}. \tag{24}$$

Here $\bar{a}_g$ is the sum of the gravitational forces acting on the satellite, $\bar{a}_{ng}$ is the sum of the non-gravitational forces acting on the surface of the satellite and $\bar{a}_{emp}$ represent the unmodelled forces which act on the satellite due to either a functionally incorrect or incomplete description

of the various forces acting on the satellite (Seeber, 2003). The gravitational forces, $\bar{a}_g$ acting on an orbiting satellite consist of a series of perturbations that are often expressed by Equation (25),

$$\bar{a}_g = \bar{P}_{geo} + \bar{P}_{set} + \bar{P}_{ot} + \bar{P}_{rd} + \bar{P}_{smp} + \bar{P}_{rel}, \tag{25}$$

where $\bar{P}_{geo}$ is the geo-potential force due to the gravitational attraction of the Earth, $\bar{P}_{set}$ and $\bar{P}_{ot}$ define perturbations due to solid Earth tides and ocean tides respectively, $\bar{P}_{rd}$ is due to rotational deformation of the Earth, $\bar{P}_{smp}$ are perturbations due to the Sun, Moon and planets and $\bar{P}_{rel}$ describes perturbations due to general relativity (Seeber, 2003). The non-gravitational forces acting on an orbiting satellite are given by Equation (26) as

$$\bar{a}_{ng} = \bar{P}_{drag} + \bar{P}_{solar} + \bar{P}_{earth} + \bar{P}_{thermal}. \tag{26}$$

Here $\bar{P}_{drag}$ is the atmospheric drag acting on a satellite, $\bar{P}_{solar}$ is due to solar radiation pressure, $\bar{P}_{earth}$ describes perturbation due to Earth radiation pressure (related to the albedo of Earth, typically 10% of the acceleration due to direct solar radiation pressure), $\bar{P}_{thermal}$ is the perturbation due to thermal radiation imbalance resulting from non-uniform temperature distribution on different satellite surfaces.

2.4.1.2. Gravitational field of the Earth

The Earth's gravity field is one of the most dominant forces that causes perturbations on an orbiting satellite. This force is often described in terms of spherical harmonic functions (Rapp, 1998). Harmonic functions may be defined as functions that satisfy Laplace's equation of the form given by Equation (27),

$$\nabla^2 U = 0. \tag{27}$$

In Equation (27), U represents a model of the Earth's gravity potential energy and ∇^2 is the Laplace operator expressed as in Equation (28),

$$\nabla^2 = \frac{\partial^2}{\partial x^2} + \frac{\partial^2}{\partial y^2} + \frac{\partial^2}{\partial z^2}. \tag{28}$$

Expressing the Laplace's equation in terms of spherical polar coordinates (where $x = r\sin\theta\cos\varphi$, $y = r\sin\theta\sin\varphi$ and $z = r\cos\theta$ with $r \in [0,\infty]$, $\theta \in [0,\pi]$ and $\varphi \in [0,2\pi]$) yields Equation (29) (Heiskanen & Moritz, 1967),

$$\nabla^2 U = \frac{1}{r^2}\frac{\partial}{\partial r}\left(r^2\frac{\partial U}{\partial r}\right) + \frac{1}{r^2\sin\theta}\frac{\partial}{\partial\theta}\left(\sin\theta\frac{\partial U}{\partial\theta}\right) + \frac{1}{r^2\sin^2\theta}\frac{\partial^2 U}{\partial\lambda^2} = 0. \qquad (29)$$

Here r is the Earth's geocentric radius, θ is the geocentric co-latitude and λ is the geocentric longitude. Equation (29) can be solved to obtain the gravity potential of the Earth in terms of spherical harmonics. For further details on how the gravity potential is derived from Equation (29), see Tapley *et al.* (2004a). In particular, the gravity potential can be expressed in the form described by Equation (30),

$$U(r,\varphi,\lambda) = \frac{GM}{r} + \frac{GM}{r}\sum_{n=2}^{N_{\max}}\sum_{m=0}^{l}\left(\frac{a}{r}\right)^l P_{nm}(\sin\varphi)\left[C_{nm}\cos m\lambda + S_{nm}\sin m\lambda\right]. \qquad (30)$$

Here, U is the gravity potential, GM is the Earth's gravity constant, (r,φ,λ) represent the magnitude of the radius vector, the latitude and the longitude respectively, n, m are the degree and order of spherical harmonics, P_{nm} are the Legendre functions and $\{C_{nm}, S_{nm}\}$ are the spherical harmonic (Stokes') coefficients (Tapley *et al.*, 2004a). The associated Legendre function for a given order m and degree n is defined by Equation (31),

$$P_{nm} = \left(1-x^2\right)^{m/2}\frac{d^m P_n(x)}{dx^m}, \qquad (31)$$

where $P_n(x)$ is the Legendre function which is expressed as a function of the independent variable x as depicted in Equation (32),

$$P_x(x) = \frac{1}{2^n n!}\frac{d^n}{dx^n}\left(x^2-1\right)^n. \qquad (32)$$

In most cases the spherical harmonic coefficients, $\{C_{nm}, S_{nm}\}$ are preferably given in normalized form, in which the order of magnitude remains approximately constant. This is due to the fact that these coefficients decrease numerically with large orders of magnitude with increase of degree and order of spherical harmonics. Computationally, these large differences could lead to round-off errors, although with modern computers and compilers, it is less a problem currently than say thirty years ago. In the SDAS software, any format is read (normalized or unnormalized) and converted to an internal (unnormalized) format for numerical processing.

The standard normalization factor is defined as in Equation (33) see Montenbruck and Gill (2001),

$$C_{nm} = \sqrt{\frac{(n-m)!(2n+1)(2-\delta_{0m})}{(n+m)!}}\,\bar{C}_{nm}, \tag{33}$$

and

$$S_{nm} = \sqrt{\frac{(n-m)!(2n+1)(2-\delta_{0m})}{(n+m)!}}\,\bar{S}_{nm}, \tag{34}$$

where C_{nm} and S_{nm} are the standard coefficients used in Equation (30), $\bar{C}_{nm}$ and $\bar{S}_{nm}$ are the normalized coefficients and $\delta_{0\mathrm{m}}$ is the Kronecker delta between 0 and m. For normalization purpose Equation (32) can multiplied by,

$$\begin{cases} \sqrt{(2n+1)}, & \text{if m=0 or} \\ \sqrt{2(2n+1)\dfrac{(n-m)!}{(n+m)!}}, & \text{if m} \geq 1. \end{cases} \tag{35}$$

Assuming that,

$$P_n^{(m)}(x) = \frac{d^m P_n(x)}{dx^m}. \tag{36}$$

In terms of the fully normalized coefficients, Equation (30) can be rewritten as in Equation (37),

$$U(r,\varphi,\lambda) = \frac{GM}{r} + \frac{GM}{r}\sum_{n=2}^{N_{\max}}\sum_{m=0}^{l}\left(\frac{a}{r}\right)^l \bar{P}_{nm}(\sin\varphi)\left[\bar{C}_{nm}\cos m\lambda + \bar{S}_{nm}\sin m\lambda\right]. \tag{37}$$

where, r is the geocentric radius of the computation point, $\{\bar{C}_{nm}, \bar{S}_{nm}\}$ are fully normalised spherical harmonic coefficients of degree n and order m, $\bar{P}_{nm}(\cos\theta)$ are fully normalized associated Legendre functions of degree n and order m. The spherical harmonics, $\{\bar{C}_{nm}, \bar{S}_{nm}\}$ may be classified as zonal (here, $m=0$ and the zeros of $\{\bar{C}_{nm}, \bar{S}_{nm}\}$ depict that the sphere is divided into latitudinal zones), sectorial (here $m=n$) and tesseral (in this case $m \neq n$). A typical example of zonal spherical harmonic functions is the J_2 coefficient which is equivalent to, $J_n = -J_{n0} = -\bar{C}_{n0}$. The J_2 (oblateness) coefficient is the main contributor of mass distribution near the Earth's polar axis causing the shape of Earth's rotation to deviate from a perfect sphere

(Montenbruck and Gill, 2001). Figure 7 illustrates some examples of spherical harmonic functions. A typical geopotential model is often described by these spherical harmonic coefficients.

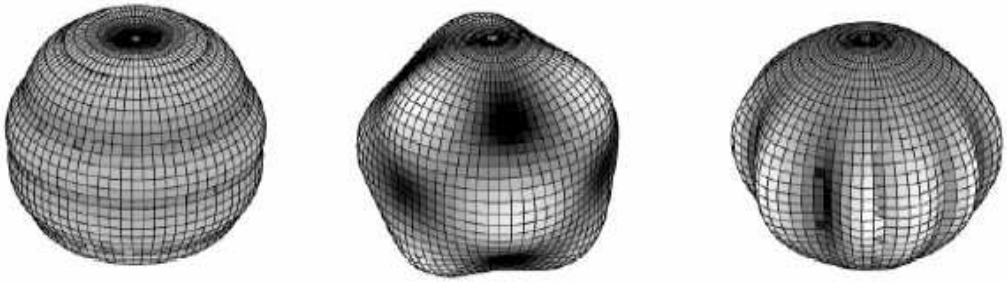

Figure 7. Examples of spherical harmonic functions of degree n and order m. (a) zonal (b) tesseral (c) sectoral (Laxon, 2003).

2.4.1.3. Third body effects

Satellites undergo acceleration originating from gravitational forces from the Sun, Moon and planets. These third body effects can dominate atmospheric drag effects in the case of high altitude satellites when the atmospheric drag effect begins to diminish. Generally, the effects from the three body perturbing forces are commonly described as per Equation (38) as reported in Tapley *et al*. (2004a),

$$\bar{P}_{smp} = \sum_{j=1}^{n_p} GM_j \left(\frac{\vec{\Delta}_j}{\Delta_j^3} - \frac{\vec{r}_j}{r_j^3} \right). \tag{38}$$

Here it is assumed that the gravity fields of the celestial bodies are perfect spheres. In Equation (38) j represents a specific body, GM_j denotes the gravitational parameter of each j, the position of the body j relative to the satellite is given by $\vec{\Delta}_j$, and $\vec{r}_j$ is the position vector of the body j relative to Earth.

2.4.1.4. Solid Earth tides

The solid Earth tides often manifest as an indirect effect from the attraction of Moon and Sun. They cause a deformation of the Earth's figure and therefore of the Earth's gravity field, which can be expressed as a deviation of the harmonic coefficients. The deviations of the Earth's

harmonic coefficients of the second and third order of spherical harmonics due to solid tides can be expressed by Equation (39) (McCarthy and Petit, 2003),

$$\Delta\bar{C}_{nm} - i\Delta\bar{S}_{nm} = \frac{k_{nm}}{2n+1}\sum_{j=2}^{3}\frac{GM_j}{GM_E}\left(\frac{R_e}{r_j}\right)^{n+1}\bar{P}_{nm}\left(\sin\Phi_j\right)e^{-im\lambda_j} \quad \left(\text{with } \bar{S}_{n0}=0\right). \qquad (39)$$

Here k_{nm} is the nominal degree Love number for degree n and order m, R_e is the equatorial radius of the Earth, GM_E is the gravitational parameter for the Earth, GM_j represents the gravitational parameters for the Moon $(j=2)$ and Sun $(j=3)$, r_j corresponds to the distance from geocentre to Moon or Sun, Φ_j is the body fixed geocentric latitude of Moon or Sun, λ_j corresponds to the Earth fixed east longitude (from Greenwich) of Moon or Sun and lastly, $\bar{P}_{nm}$ is the normalized associated Legendre function. The force acting on a satellite due to solid Earth tides is described by Equation (40),

$$\bar{P}_{set} = \sum_{j=1}^{2}\frac{k_2}{2}\frac{GM_{S,M}}{\vec{r}_{S,M}^{\,3}}\frac{a^5{}_E}{\vec{r}_{Sat}^{\,4}}\left[\left(3-15\cos^2\theta\right)\frac{\vec{r}_{sat}}{\vec{r}}+6\cos\theta\frac{\vec{r}_{S,M}}{r_{S,M}}\right]. \qquad (40)$$

In Equation (40), $\vec{r}$ is the radius vector of satellite (sat), Sun (S) and Moon (M), θ is the angle between radius vectors $\vec{r}_{sat}$ and $\vec{r}_{S,M}$, a_E is the equatorial radius of Earth, GM is the gravitational constant of the Sun and Moon.

2.4.1.5. Ocean Tides

The deformation of the Earth's gravity field caused by ocean loading tides can also be manifested in the deviations of the harmonic coefficients. A full description of equations describing the ocean tides model can be found in McCarthy and Petit (2003) and Petit and Luzum (2010). The equation describing ocean loading has been reported in McCarthy and Petit (2003) and Petit and Luzum (2010) and is given in Equation (41),

$$\Delta C_{nm} - i\Delta S_{nm} = F_{nm}\sum_{s(n,m)}\bar{\sum_{+}}\left(C^{\pm}{}_{snm} \mp S^{\pm}{}_{snm}\right)e^{\pm i\theta_f}, \qquad (41)$$

where,

$$F_{nm} = \frac{4\pi G\rho_w}{g}\sqrt{\frac{(n+m)!}{(n-m)!(2n+1)(2-\delta_{om})}}\left(\frac{1+k'_n}{2n+1}\right). \qquad (42)$$

Here g is mean equatorial gravity, k'_n is the load deformation coefficients, C_{snm}, S_{snm} are ocean tide coefficients for the tide constituent s, and θ is the argument of tide constituent s.

2.4.1.6. Pole tides

The pole tides given by Equation (43) are generated by the centrifugal effect of polar motion

$$\begin{aligned}\Delta v &= -\left(\frac{\Omega^2 r^2}{2}\right)\sin 2\theta\left(m_1\cos\lambda + m_2\sin\lambda\right)\\ &= -\left(\frac{\Omega^2 r^2}{2}\right)\sin 2\theta R_e\left[\left(m_1 - im_2\right)e^{i\lambda}\right],\end{aligned} \tag{43}$$

where $\left(m_1,\ m_2\right)$ are wobble variables. The deformation which constitutes the pole tide produces a perturbation given by,

$$-\frac{\Omega^2 r^2}{2}\,sin\,2\theta R_e\left[k_2\left(m_1 - im_2\right)e^{i\lambda}\right], \tag{44}$$

in the external potential. For the purpose of satellite orbit determination this perturbation is related to changes in the geopotential coefficients $\bar{C}_{21}$ and $\bar{S}_{21}$.

2.4.1.7. Relativistic effects

The relativistic correction to the acceleration of an orbiting satellite is commonly accounted as per Equation (45) recommended by the IERS 2003, published by McCarthy and Petit (2003) and Petit and Luzum (2010),

$$\begin{aligned}\Delta\ddot{\vec{r}} = \frac{GM_\oplus}{c^2 r^3}\Bigg\{&\left[2\left(\beta+\gamma\right)\frac{GM_\oplus}{r} - \gamma\left(\dot{\vec{r}}\cdot\dot{\vec{r}}\right)\right]\vec{r} + 2\left(1+\gamma\right)\left(\vec{r}\cdot\dot{\vec{r}}\right)\dot{\vec{r}}\Bigg\}.\\ &\left(1+\gamma\right)\frac{GM_\oplus}{c^2 r^3}\left[\frac{3}{r^2}\left(\vec{r}\times\dot{\vec{r}}\right)\left(\vec{r}\cdot\vec{J}\right) + \left(\dot{\vec{r}}\times\vec{J}\right)\right] + \left\{\left(1+2\gamma\right)\left[\dot{\vec{R}}\times\left(\frac{-GM_s\vec{R}}{c^2 R^3}\right)\right]\times\dot{\vec{r}}\right\}\end{aligned} \tag{45}$$

In Equation (45) the correction includes:

- first term, the non-linear Schwarzschild field of the Earth $\left(\approx 10^{-9}\ \mathrm{m\ s^{-2}}\right)$,
- second term, Lense-Thirring precession (frame dragging) $\left(\approx 10^{-11}\ \mathrm{m\ s^{-2}}\right)$,
- third term, de Sitter (geodetic) precession $\left(\approx 10^{-11}\ \mathrm{m\ s^{-2}}\right)$.

The approximate magnitude of acceleration presented here refers to LAGEOS as calculated by the SDAS package. In addition, c in Equation (45) is the speed of light, β, γ are the Parameterized Post Newtonian (PPN) parameters (these are parameters used to describe the classical tests of general relativity; in general relativity the two parameters are given by $(\beta,\gamma)=(1,1)$), $\vec{r}$ is the position of the satellite relative to the Earth, $\vec{R}$ is the position of the Earth relative to the Sun, $\vec{J}$ is the Earth's angular momentum per unit mass, $GM_{\oplus}$ is the gravitational coefficient of Earth and GM_s the gravitational coefficient of the Sun. Although the effects of these parameters are very small for the purpose of POD they need to taken into account as there are some long-term periodic and secular effects in the orbit (Huang and Liu 1992).

2.4.1.8. Solar radiation pressure

Solar radiation pressure describes an exchange of momentum between photons absorbed and reflected by the surfaces of an orbiting satellite (Ziebart, 2001). This conveyed force causes acceleration which is dependent on the solar flux, the satellite's mass m and cross-section A. According to Montenbruck and Gill (2001), the solar radiation pressure contributions to the total perturbative acceleration is described as per Equation (46),

$$\bar{P}_{solar} = -\nu P_e C_R \frac{A}{m}\frac{\vec{r}_e}{r_e^3} AU^2. \qquad (46)$$

where P_e is the radiation flux from the Sun, $\vec{r}_e$ is the geocentric position of the Sun, C_R is the reflection coefficient $(C_R = 1.13)$ and ν is the eclipse factor and it determines the amount of solar radiation acting on the satellite as it passes through umbra and penumbra regions. The conditions for the eclipse factor functions are $\nu = 0$ if the satellite is in the shadow region (umbra phase), $\nu = 1$ if the satellite is in full sunlight and $0 < \nu < 1$ if the satellite is in partial shadow (penumbra phase).

2.4.1.9. Atmospheric drag

Satellites orbiting the Earth at low Earth altitude are also affected by drag force (the component of the resultant dynamic fluid force that acts in opposition to the relative motion of the object with respect to the fluid) (Montenbruck and Gill, 2001). Although the air density is extremely low at altitudes higher than 1000 km, the high velocity of a satellite often leads to significant (de-)acceleration. The acceleration due to air drag can be obtained by Equation (47) according to Montenbruck and Gill (2001),

$$\bar{P}_{drag} = -\frac{1}{2} C_D \frac{A}{m} \rho v_r^2 \vec{e}_v . \tag{47}$$

Here, C_D is a dimensionless quantity describing the satellite's interaction with the atmosphere (also referred to as the satellite's drag coefficient); m is the total mass of the satellite; $\vec{e}_v = \vec{v}_r / v_r$ is a unit vector describing the direction of the acceleration due to drag and is anti-parallel to the satellite velocity vector; v_r is the magnitude of the satellite's velocity relative to the atmosphere; A is the projected area in the direction of the velocity vector relative to the atmosphere and lastly, ρ the atmosphere's mass density.

2.4.2. Tropospheric delay modelling

SLR observations are highly affected by the residual errors arising from inaccurate modelling the effect of delay of the signal propagation through the neutral atmosphere (i.e., the troposphere and stratosphere). Early atmospheric correction models used during SLR analysis include one developed by Marini and Murray (1973). Later, the shortcomings of Marini and Murray's atmospheric model (e.g., inaccurate mapping function component of the model) were pointed out by Mendes *et al.* (2002). Today, mapping functions derived by Mendes *et al.* (2002) are widely used in combination with any zenith delay (ZD) model to predict atmospheric delay in the line-of-sight direction.

In general, the atmospheric delay contribution is described by McCarthy and Petit (2003) and is expressed here by Equation (48),

$$d_{atm}^{z} = 10^{-6} \int_{r_s}^{r_a} N dz = \int_{r_s}^{r_a} (n-1)\, dz. \tag{48}$$

Splitting the ZD into hydrostatic $\left(d_h^z\right)$ and non-hydrostatic $\left(d_{nh}^z\right)$ components, Equation (48) can be rewritten as described by Equation (49),

$$d_{atm}^z = d_h^z + d_{nh}^z = 10^{-6}\int_{r_s}^{r_a} N_h dz + 10^{-6}\int_{r_s}^{r_a} N_{nh} dz. \tag{49}$$

In Equation (49), $N = (n-1)\times 10^6$ is the total group refractivity of moist air, n is the total refractivity index of moist air, N_h and N_{nh} are the hydrostatic and non-hydrostatic components of the refractivity, r_s is the geocentric radius of the laser station, r_a is the geocentric radius of the top of neutral atmosphere, and d_{atm}^z and dz have length units.

According to Mendes and Pavlis (2004) the hydrostatic ZD can be expressed as in Equation (50),

$$d_h^z = 0.002416579\frac{f_h(\lambda)}{f_s(\phi,H)}P_s, \tag{50}$$

where d_h^z is the zenith hydrostatic delay in meters, and P_s is the surface barometric pressure in hPa. The function $f_s(\phi,H)$ in Equation (50) can be expressed as in Equation (51).

$$f_s(\phi,H) = 1 - 0.00266\cos 2\phi - 0.00000028H. \tag{51}$$

Here ϕ is the geodetic latitude of the station and H is the geodetic height of the station in meters. The dispersion equation for the hydrostatic component is described by Equation (52)

$$f_h(\lambda) = 10^{-2}\times\left[k_1^*\frac{\left(k_0+\sigma^2\right)}{\left(k_0-\sigma^2\right)^2} + k_3^*\frac{\left(k_2+\sigma^2\right)}{\left(k_2-\sigma^2\right)^2}\right]C_{CO_2}. \tag{52}$$

In Equation (52), $k_0 = 238.0185\ \mu\text{m}^{-2}$, $k_2 = 57.362\ \mu\text{m}^{-2}$, $k_1^* = 19990.975\ \mu\text{m}^{-2}$, and $k_3^* = 579.55174\ \mu\text{m}^{-2}$, σ is the wave number, with $\sigma = \lambda^{-1}$, where λ is the wavelength in μm, $C_{CO_2} = 1 + 0.534\times 10^{-6}(x_c - 450)$, where x_c is the carbon dioxide (CO_2) content in parts-per-million (ppm). The expression for non-hydrostatic ZD expressed as in Equation (53),

$$d_{nh}^z = 10^{-4}\left(5.316 f_{nh}(\lambda) - 3.759 f_h(\lambda)\right)\frac{e_s}{f_s(\phi,H)}, \tag{53}$$

where d_{nh}^{z} is the zenith non-hydrostatic delay in meters, and e_s is the surface water vapour pressure in nPa. The dispersion expression for the non-hydrostatic component is given by Equation (54),

$$f_{nh}(\lambda) = 0.003101\left(w_0 + 3w_1\sigma^2 + 5w_2\sigma^4 + 7w_3\sigma 6\right), \tag{54}$$

where $w_0 = 295.235$, $w_1 = 2.6422\ \mu m^2$, $w_2 = -0.032380\ \mu m^4$, and $w_3 = 0.004028\ \mu m^6$. Marini and Murray (1973) have demonstrated that if the atmosphere is assumed to be azimuthally symmetric then the mapping functions for the atmospheric delay are asymptotic in $\sin(\varepsilon)$ near zenith and inverse in $\sin(\varepsilon)$ near the horizontal. The azimuthally symmetric mapping function and the hydrostatic gradient can be calculated from the geopotential heights. In the case where the wet mapping function is not in hydrostatic equilibrium, the vertical distribution of refractivity due to water vapour is utilized. Here the adopted parameters need to reflect both the vertical distribution as well as the changing geometry with height above the surface due to the curvature of the Earth. The adopted parameter for both the hydrostatic and wet mapping functions is a single input along with the site geographic location. The mapping function of a truncated continued fraction in $1/\sin(\varepsilon)$ can be described as per Equation (55) as reported in McCarthy and Petit (2003),

$$m(\varepsilon) = \frac{1 + \dfrac{a}{1 + \dfrac{b}{1+c}}}{\sin\varepsilon + \dfrac{a}{\sin\varepsilon + \dfrac{b}{\sin\varepsilon + c}}}. \tag{55}$$

In Equation (55), $m(\varepsilon)$ is the mapping function, ε is the vacuum elevation of the incoming ray and a, b and c are the coefficients of the mapping function which depend on integrals refractivity through the atmosphere.

2.5. Applications of SLR measurements

2.5.1. International Terrestrial Reference Frame (ITRF)

The SLR observations, in particular from LAGEOS 1 and 2 have played a significant role in providing data that have been used for the establishment of the ITRF[6] (McCarthy and Petit, 2003). The ITRFs are realized through computing global Cartesian coordinates and geophysical parameters such as station coordinates (positions and linear velocities) and Earth Orientation parameters (EOP) (McCarthy and Petit, 2003 and Petit and Luzum, 2010). These coordinates form a single solution which is sent to the International Earth Rotation and Reference System (IERS) where it is used to determine a unique solution of the ITRF. Single solutions from other space geodetic techniques such as GPS, VLBI and DORIS may be combined with the solution from SLR observations to form a four-in-one solution which can then be used to determine, maintain and improve the ITRF precisely**.** In addition, the four-in-one solution provides a unique solution for the measurements of the EOP which are used to describe the irregularities of the Earth rotation with respect to a non-rotating reference frame as well as for satellite positioning (Gambis, 2004).

Generally, the EOP are formed by five components: the X and Y polar motion with respect to the crust, Universal Time (UT1), a nutation correction in ecliptic longitude $(d\varphi)$, and a nutation correction in obliquity $(d\varepsilon)$. Today, the two nutation corrections can be precisely modelled to an accuracy of about 3 cm for about a one year period (Oliveau and Freedman, 1997). The UT1 parameter may be defined as a measure of the angular rotation of the Earth about its spin axis and is usually specified with respect to a reference time defined by atomic clocks (e.g., UT1–UTC) (Freedman *et al*., 1994). This parameter together with X and Y polar motion are known to exhibit rapid variations and are also unpredictable in time. The random variations are due to the interaction of the atmosphere and the crust (Freedman *et al.* 1994) while the UT1 often varies more rapidly than polar motion.

The difference between the astronomically determined duration of the day and 86 400s of International Atomic Time (TAI) is known as the Length-Of_Day (LOD) and is often derived

[6] The ITRF is a set of physical points with precisely determined coordinates in a specific coordinate system attached to the International Terrestrial Reference System (ITRS) (McCarthy and Petit, 2003).

from the UT1 series as a temporal rate of change of the difference (UT1-TAI). The excess LOD, denoted by A is related to the UT1 rate of change given by Equation (56),

$$A = -A_0 \frac{du}{dt}, \tag{56}$$

where A is the excess LOD and A_0 is the nominal LOD (86 400 seconds). When modelling the stochastic behaviour of UT1 and LOD the effects of physical processes (e.g., solid Earth and ocean tides) which influence the rotation rate ought to be taken into account. Such effects can be removed from the two EOP components by applying corrections obtained from conventional tidal models (Yoder *et al.*, 1981). The Earth orientation changes often represented by polar motion, X, Y, the equatorial components in a geographical reference frame, and variations in the LOD (see Figure 8 for variations in LOD and excitations in X and Y polar motion) are often explained by studying variations of atmospheric and/or oceanic angular momentum. Such variations are caused by the exchange of angular momentum between the solid Earth and its geophysical fluid envelope. Eubanks *et al.* (1993) found that variations in the Earth's rate of rotation which corresponds to changes in LOD amount to a few parts in 10^8. Studies by Ponsar *et al.* (2003) suggested that the variations in LOD are caused by interaction between the Earth's core and mantle. Similar studies by Gross *et al.* (2003) related the LOD variations with tidal variations exhibiting periods between 12 hours and 18.6 years. Such variations were believed to be due to the deformation of solid Earth and changes in the strength and direction of the atmospheric winds.

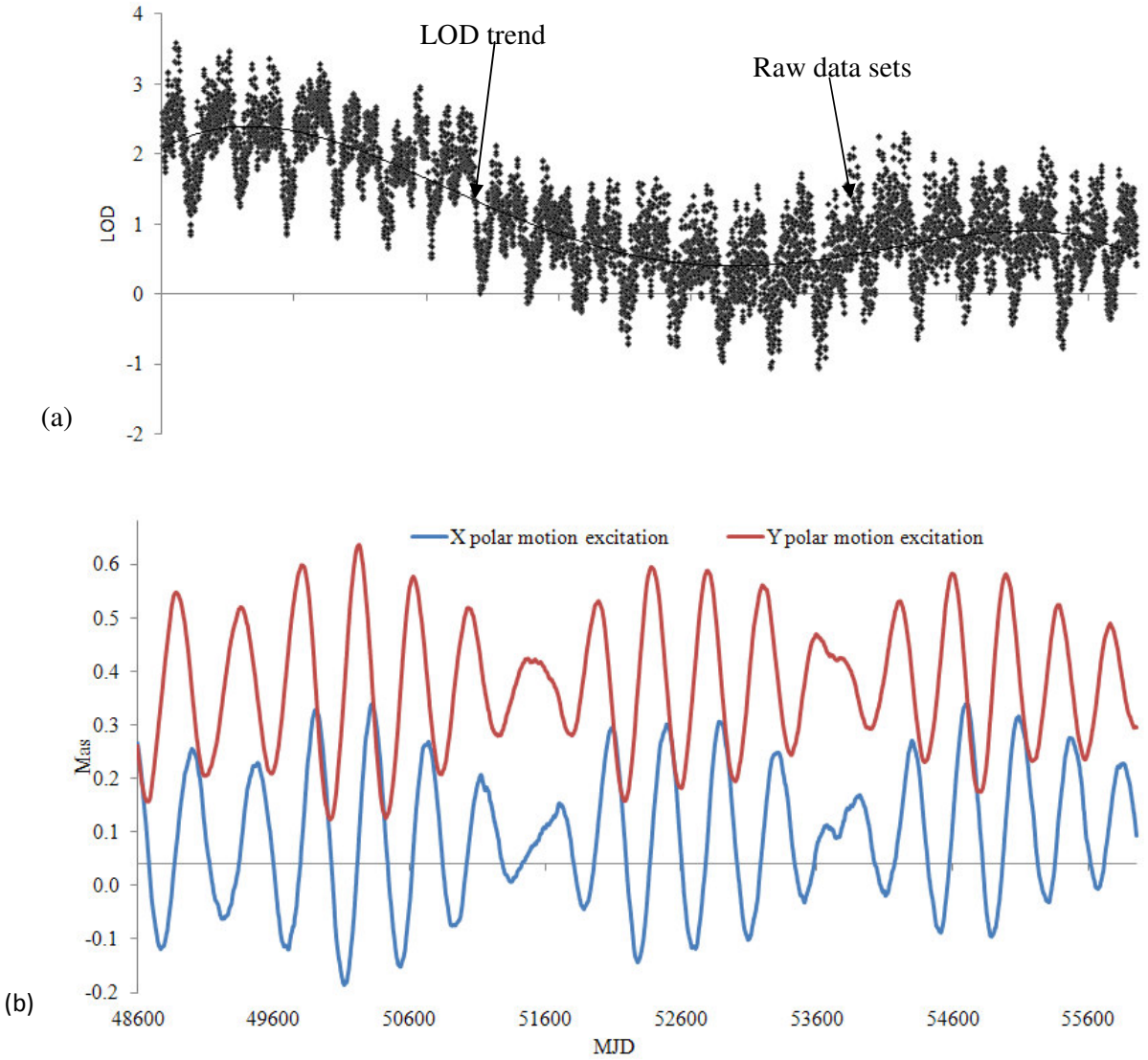

Figure 8. Time series (in Modified Julian Date (MJD)) of Earth rotation extracted from SLR data. (a) LOD variations, (b) X and Y polar motion excitation, data obtained from http://www.iers.org/IERS archive.

2.5.2. Gravity field

Satellite Laser Ranging tracking data have been used to determine the Earth's gravity field both at global and regional scales. Since the orbital motion of artificial satellites is influenced by gravitational forces, precise satellite tracking measurements provide orbit solutions which can be inverted to derive the gravity field. For instance, the long wavelength gravity information can be derived through SLR range measurements by high altitude satellites such as LAGEOS.

However, gravity field determination to higher degree of coefficients using SLR experiences certain drawbacks due to unsteady and fragmentary orbit tracking by ground stations. The recent satellite missions, e.g. CHAMP, GRACE and GOCE are designed to overcome the existing SLR disadvantages. Nowadays the gravity field determination is achieved based on three techniques in the context of CHAMP, GRACE and GOCE satellite missions (Tapley *et al*. 2004b). These techniques include a continued GNSS tracking using on-board GPS receivers and accelerometers for measuring non-gravitational forces such as atmospheric drag and solar radiation pressure. The GRACE satellite is additionally equipped with a K-band microwave system (known as K-band range-rate technique), which measures their separation range-rate with significant accuracy (Tapley *et al*. 2007). This technique is believed to be the most important in terms of gravity field determination for the on-board GRACE mission. Satellite gradiometry equipped on the GOCE mission is the most recent technique used for gravity field determination and non-gravitational accelerations acting on the satellite (Pail *et al*. 2011). The on-board GOCE gradiometer determines the position and velocity of the satellite and is used for estimation of the long wavelength signal of the gravity field. Low-altitude satellites, however, are subjected to non-gravitational forces, particularly from the atmosphere, and these can affect the gravity inversions at all wavelengths.

According to Newton's law, changes in the gravity field are a manifestation of mass redistribution in the Earth system. Any movement of masses in, on or above the Earth will therefore introduce variations in the gravity field of the Earth (Dickey *et al*., 2002; Cox *et al*., 2003). Temporal variations of Earth's gravity field may range between 10 and 100 ppm (variation from the mean) and often occur on a variety of time scales (ranging from hours to thousands of years) (Tapley *et al*., 2004b). Such variations are caused by a variety of phenomena that redistribute mass, including tides raised by the Sun and Moon, and post-glacial rebound. Surface mass change in the atmosphere, oceans, hydrosphere and cryosphere are dominated by seasonal and inter-annual variations while processes such as isostatic glacial recovery and sea-level change give rise to long-term secular or quasi-secular signatures.

Several studies have investigated the long term and the seasonal variations of the Earth's gravity field using data collected from different satellite missions. In particular, the lower order harmonic component of the gravity field with $n=2$ and $m=0$ (hereafter J_2) which characterizes the oblateness of the Earth has attracted a lot of interest from the scientific

community. Early studies of J_2 by for example Yoder *et al*. (1983) showed a secular decrease in J_2 that was consistent with a steady migration of mass from low latitudes towards high latitudes resulting in a linearly decreasing trend. Such a trend was thought to be related to post-glacial rebound (PGR), the Earth's ongoing response to the removal of the ice loads at the end of the last ice age. Long term studies by Cox and Chao (2002) however discovered that J_2 started to increase around 1997, but later exhibited a negative trend (from 2002) as illustrated in Figure 9. This trend is believed to have inverted again with J_2 once more decreasing. Several mechanisms have been suggested to be the causes for this sudden change of the J_2 coefficient. For example, Dickey *et al*. (2002) attributed this change to the surge in sub-polar glacial melting and to mass shifts in the Southern, Pacific, and Indian oceans. In addition to the increasing trend of the J_2 coefficient, Nerem *et al*. (2000) found that the J_2 coefficient might be exhibiting seasonal variability due to a combination of atmospheric pressure variations and variations in the distribution of water in the oceans and on land. Furthermore, Dickey *et al*. (2002) detected inter-annual variability in J_2 which they attributed to climatically driven oscillations in the ocean, storage of water, snow, and ice on land and partly as a result of the effects of anelasticity on the 18.6-year solid Earth tide as suggested by Benjamin, *et al*. (2006).

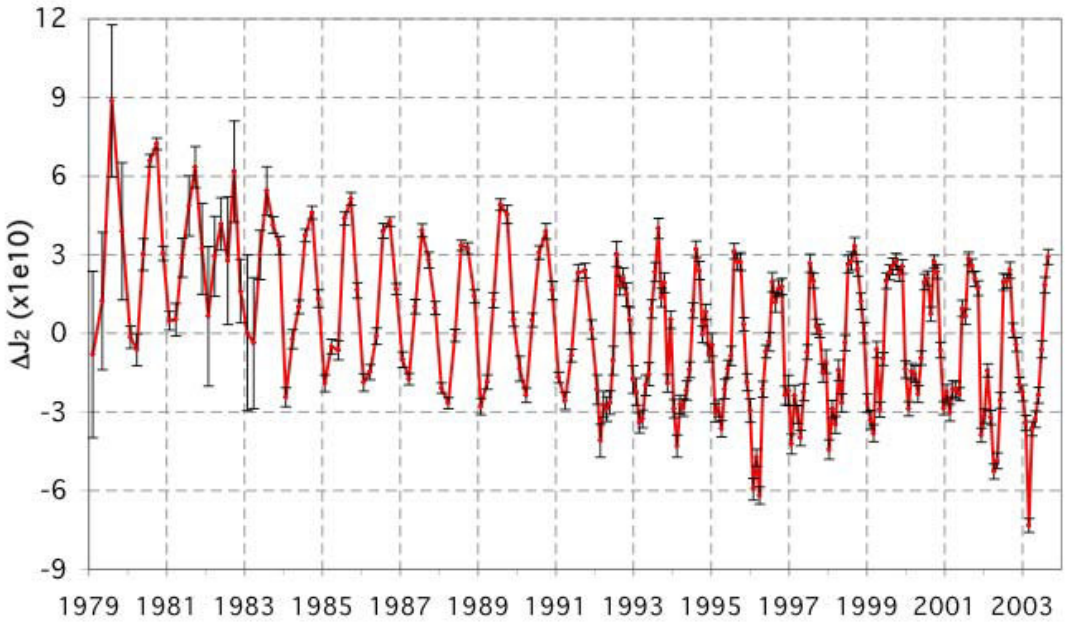

Figure 9. The variability of J_2 coefficient as derived from SLR and DORIS data spanning the period from 1976 to 2006 (Cox and Chao, 2002).

2.5.3. Determination of the geoid

Data from SLR observations have been used for computation of spherical harmonic models. These models can be used to derive the geoid (this is the equipotential surface of the Earth's gravity field that corresponds closely with Mean Sea Level (MSL) in the open oceans, ignoring oceanographic effects) as well as the geoidal height (the separation between the geoid and the ellipsoid) (Eckman, 1998). The geoidal height is often computed from a set of normalized spherical coefficients using Equation (57),

$$N_{GM} = \frac{GM}{r\gamma}\sum_{n=2}^{N_{max}}\left(\frac{a}{r}\right)^n\sum_{m=0}^{n}\left\{\bar{C}^*_{nm}\cos m\lambda + \bar{S}_{nm}\sin m\lambda\right\}\bar{P}_{nm}(\cos\theta). \qquad (57)$$

Here n_{max} is the maximum degree at which the coefficients are known, $\bar{C}^*_{nm}$ are the $\bar{C}_{nm}$ less the zonal coefficients of the normal potential of the selected reference ellipsoid, γ is the normal gravity on the surface of the reference ellipsoid and the rest of the parameters are as given in Equation (37). Determination of the geoid has been one of the main research areas in Geodesy for decades. To this end, geoid heights at any points on the Earth's surface can be determined with accuracy ranging from 30 cm to a few meters (Rapp, 1998). A number of researchers have

addressed the precise determination of geoid height on a local and regional scale for oceanographic and geophysical applications. At a local scale, the geoid can be determined by a combination of GPS derived heights and levelled heights, through gravimetric and geometric approaches. From the GPS derived heights and levelled heights at some points, the geoid heights at these points can be calculated. At a local scale the geoid height measurements are often converted to gravity anomalies or deflections of the vertical (e.g., geoid slope). Several global geoid height and gravity anomaly models have been developed from tracking and modelling the orbits of numerous artificial satellites (Dawod, 2008; Featherstone and Olliver, 2001; Kiamehr and Sjoeberg, 2005).

Global gravity change has also attracted particular attention in the scientific community as it is often related to global sea-level changes. The sources of global sea-level rise often involve the redistribution of mass from the continents to the ocean. The usage of gravity field measurements allows for discrimination between several sources through the continuous monitoring of geoid changes on both global and regional scales as well as on basin scales. Gravity field solutions can be used to numerically estimate components such as thermal expansion (eustatic) and fresh water influx which influence global sea level changes (Cazenave and Nerem, 2004; Jevrejeva *et al*., 2006). Measurements of temporal gravity variations can be also used to determine water storage change in the hydrological system. In particular, since the launch of the GRACE mission in 2002, numerical articles assessing the potential of GRACE recovering hydrological signals have been published. For example, Andersen and Hinderer (2005a) have investigated the potential of inferring inter-annual gravity field changes caused by continental water storage change, as determined from GRACE observations between 2002 and 2003. Contributions from continental water storage change were compared to the output from global hydrological models. Andersen *et al*. (2005b) and Neumeyer *et al*. (2006) correlated large scale hydrological events with the estimated change in the gravity field for certain areas of the world to an accuracy of 0.4 μGal, corresponding to 9 mm of water. On a regional scale, Winsemius *et al*. (2006) compared hydrological model outputs for the Zambezi river basin with estimates derived from GRACE. Monthly storage depths produced by the hydrological model displayed larger amplitudes and were partly out of phase compared to the estimates based on GRACE data.

2.5.4. Precise satellite orbit determination

Precise satellite orbit determination is one of the most essential applications of SLR observations. It involves the estimation of position and velocity of an orbiting satellite at a specific time epoch (Yunck, 1997). Satellite orbit determination is used for geo-location of the satellite sensors and to measure the gravity field and its variations in time. There are currently three ways in which satellite orbit can be calculated, namely: dynamic, kinematic and reduced-dynamic.

2.5.4.1. Dynamic orbit determination

The dynamic orbit determination (Yunck, 1997) utilizes a set of tracking observations and mathematical models that describe the forces acting on an orbiting satellite. Here the force and satellite models are used to compute a model of satellite acceleration over a given time. The acceleration model describes the satellite's instantaneous acceleration as a function of time, position, and velocity. In the dynamic method a nominal trajectory (satellite position as a function of time) is generated by analytically or numerically integrating the acceleration model. The orbit solution is compared with the one predicted by the observations. Selected parameters of the force models acting on the satellite may be adjusted along with an initial satellite position and velocity in the batch least-squares estimation[7] technique in order to minimize the difference between the actual observations and the predicted ranges (O-C residuals). Accuracy of the dynamic orbit determination approach is highly dependent on the satellite force models. Thus the accuracy of orbit determination may be reduced if the satellite forces are mis-modelled. Figure 10 illustrates a schematic representation of the dynamic orbit determination technique.

[7] Least squares estimation is a mathematical algorithm that uses definitive deterministic force models to minimize the RMS of measured O-C residuals. It consist of a sequence of linear LS corrections. A weighting factor is applied to each residual, and it is the square of the weighted residuals, which is minimized.

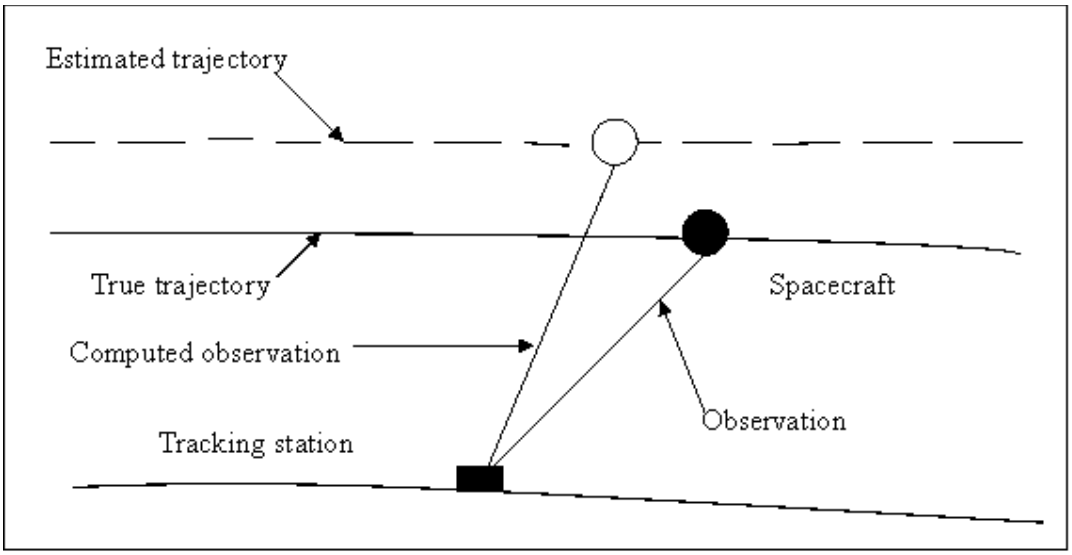

Figure 10. The orbit estimation problem (adopted from Yunck, 1997)

The basic equation describing the motion of an orbiting satellite is given by Equation (58),

$$\ddot{\vec{r}} = -\frac{GM}{r^3}\vec{r} + k_s, \tag{58}$$

where $\ddot{\vec{r}}$ is the acceleration vector of the satellite, $\vec{r}$ is the geocentric position vector of the satellite and k_s represents the sum of all the perturbing accelerations acting on the satellite, where

$$k_s = \ddot{r}_E + \ddot{r}_s + \ddot{r}_m + \ddot{r}_e + \ddot{r}_o + \ddot{r}_D + \ddot{r}_{SP} + \ddot{r}_A . \tag{59}$$

In Equation (59), $\ddot{r}_E$ is the perturbing forces due to the non-spherically and inhomogeneous mass distribution within the Earth system, $\ddot{r}_s$ and $\ddot{r}_m$ are the perturbing forces due to the Sun and the Moon respectively, $\ddot{r}_e$ and $\ddot{r}_o$ correspond to the perturbing forces as a result of the Earth and ocean tides respectively, $\ddot{r}_D$ is the atmospheric drag, $\ddot{r}_{SP}$ and $\ddot{r}_A$ correspond to Earth and solar radiation pressure respectively. A solution to Equation (58) can be obtained by using either analytical or numerical integration. However, for the purpose of precise orbit determination a numerical integration method is mostly preferred. Here, initial conditions (the position and velocity vector, $\left(r, \dot{\vec{r}}\right)$) at a time t_0 may be set as in Equation (60),

$$r(t_0) = r_0,$$
$$\vec{r}(t_0) = \vec{r}_0. \tag{60}$$

Double integration of Equation (58) using initial values of the orbit results yields a solution of the predicted orbit trajectory depicted in Equation (61),

$$r(t) = \iint \vec{r}(t)\,dt + \vec{r}_0 t + r_0\,. \tag{61}$$

The accuracy of the predicted orbit often depends on the epoch state ($r_0, \vec{r}_0$) and the acceleration model $\vec{r}(t)$ together with its physical parameters (Yunck, 1997). This can be achieved by using the least-squares method. Suppose that Z represents a vector of tracking data $(Z,...Z_n)^T$ made over an interval time (often known as the tracking arc). The task is to correct the initial values such that the nominal orbit given by Equation (61) shows a best fit to the pre-processed tracking data (e.g. the actual observations given by Z_i) with respect to the theoretical observations, $\bar{Z}_i$ derived from the solution trajectory. In other words, the aim is to obtain a trajectory $r(t)$ that minimizes a cost function expressed as in Equation (62),

$$J = \sum_{i=1}^{n} \left(Z_i - \bar{Z}_i\left[r(t)\right]\right)^2. \tag{62}$$

Theoretical observations $\bar{Z}_i$ can be obtained through linearization of Equation (62). This allows the differences $\delta Z_1 = Z_i - \bar{Z}_i$ to be formed. The differences in residuals are the observations to be used in a linear adjustment of the nominal trajectory. Let δZ represent the observable vector then the observation equation can be written as in Equation (63),

$$\delta Z = A\vec{x} + n\,. \tag{63}$$

In Equation (63), $\vec{x}$ is the vector of parameters to be estimated which include the six orbital elements $(a, e, i, \Omega, \omega, E)$ as well as adjustments to various dynamic and geometric model parameters, n is the random errors of the observable vector and A is a matrix of partial derivatives of the observations with respect to the elements of $\vec{x}$. Equation (63) is also known as the regression equation and its solution at the estimated epoch can be obtained by an iterative procedure. For further details on the regression equation, refer to Yunck (1997).

2.5.4.2. Kinematic orbit determination

The kinematic orbit determination is purely a geometric technique that depends only on GNSS (e.g. GPS) measurements and cannot be used by SLR. It does not take into account dynamic properties (e.g., gravity field, air drag, etc) of an orbiting satellite. Here the errors emanating from the satellite force models do not affect the accuracy of the kinematic orbit determination. Thus the accuracy is dependent on the availability and accuracy of GNSS data. In kinematic orbit determination the GNSS data are used to estimate the differences of the geometric coordinates, dx, dy and dz between the instantaneous a priori and the actual coordinates of the satellite (Colombo and Luthcke, 2004). The process is achieved by forming observation equations linearized about the a priori positions of the satellite. These equations are then solved to establish dx, dy and dz through a least-squares adjustment fit to the data and finally using the results to correct for the a priori positions. The kinematic orbit determination is mostly used during satellite manoeuvres when it is difficult to precisely describe the satellite dynamic forces using mathematical models (Colombo and Luthcke, 2004).

2.5.4.3. Reduced-dynamic orbit determination

In dynamic and kinematic methods the accuracy of a solution may be reduced due to mismodelling errors and GNSS measurement noise respectively. The reduced-dynamic technique (Yunck *et al*., 1994) may be defined as a method that exhibits half dynamic and half kinematic components and down-weights the errors caused by each method. In reduced-dynamic orbit determination the kinematic components of the dynamic force models are introduced in the form of the process noise model containing two parameters, the correlation time constant T which defines the correlation in the dynamic model error over one update interval and the dynamic model steady state variance V. The weighting of the kinematic and dynamic data is performed via the Kalman filter process noise at each step. When T is set to zero, and V is made large, the orbit determination method becomes kinematic, because deterministic components are not considered in the Kalman filter, and if T is large and V is zero the orbit determination method becomes dynamic, since the stochastic components are not estimated. Thus the reduced-dynamic orbit determination method is achieved by adjusting T and V to balance dynamic, geometric and measurement errors.

2.6. Global geopotential models

A number of spherical harmonic models have been developed over the years by different analysis centres. The development of such models could be attributed to the availability of terrestrial data as well as to the SLR tracking data of multiple satellites. Global Gravity field Models can be classified into three groups, namely, satellite-only, combined and tailored gravity field models (Amos and Featherstone, 2003). In the following a description of the various classes of geopotential gravity field models is provided.

2.6.1. Satellite-only GGMs

The satellite-only GGMs are primarily derived from the analysis of the orbits of tracked artificial Earth satellites. Numerous factors have been attributed to the degradation of the accuracy of the satellite-only models. These include:

a) Power-decay of the gravitational field with altitude,
b) The lack of continuous tracking data from the existing stations,
c) Precession of the Earth-based range measurements to the satellites (as a result of atmospheric refraction),
d) Difficulties in modelling non-gravitational and third body perturbations and,
e) Incomplete sampling of the global gravity field due to the limited number of satellite orbital inclinations available.

Due to these limitations gravity field models with high degree coefficients are often contaminated by noise.

2.6.2. Combined GGMs

The satellite-only models are often combined with terrestrial gravity data, and marine gravity anomalies computed by using satellite radar altimeter and airborne gravity data to yield high-degree (typically 360) combined GGMs. The combined GGMs are subject to the same deficiencies as in satellite-only GGMs. In addition, the combined gravity models are limited in precision due to the poor spatial coverage and the quality of the additional data used as well as other errors emanating from terrestrial gravity anomalies (Heck, 1990). A typical example is the long-wavelength errors in terrestrial gravity anomalies caused by distortions in and offsets among different vertical geodetic datums reported in e.g., Heck (1990).

2.6.3. Tailored GGMs

In tailored gravity field models the spherical harmonic coefficients of the satellite-only models or the combined models are often adjusted and extended to higher degrees by using higher resolution gravity data that may have not necessarily been used previously (Wenzel 1998). This is normally achieved using integral formulas to derive corrections to the existing geopotential coefficients, as opposed to the combination at the normal equation level that is used to construct combined GGMs. Tailored GGMs are only applied over the area in which the tailoring was applied, because spurious effects can occur in areas where no data are available (Kearsley and Forsberg, 1990).

2.6.4. Some remarks on the classification of gravity field models

A number of GGMs have been derived by different groups around the world. These models include the Ohio State University (OSU) series, GeoForschungs Zentrum (GFZ) Potsdam series, Goddard Earth Models (GEM) series, Joint Gravity Models (JGM) series, Texas Earth Gravity (TEG) models, GRIM (GRGS and German Geodetic Research Institute Munich) models and European Improved Gravity model of the Earth by New techniques (EIGEN) models. All the published models have been made available to the scientific community and are freely available to the public for example at the International Centre for Global Earth Models on http://icgem.gfz-potsdam.de/ICGEM. A review of gravity field models derived between 1970 and 1997 can be found in Rapp (1998). Here only developments undergone in the gravity field modelling for the last two decades (e.g., 1990 – 2010) are discussed. Characteristics of these models are summarized in Table 2.

Table 2. Summary of some of the GGMs released between 1990 and 2008. Data: S=satellite tracking data, G = gravity data, A = altimetry data. Geophysical applications of these models include gravity field, satellite orbit determination, station coordinates, reduction of altimeter data, Earth rotation and computation of geoid undulations.

Model	Year	Deg.	Data	Reference
GRIM4C1	1990	50	S, G, A	Schwintzer *et al*. (1991)
OSU91A	1991	360	GEMT2, G, A	Rapp *et al*. (1991)
JGM3	1994	70	S, G, A	Tapley *et al*. (1996)
GRIM4-S4	1995	70	S	Schwintzer *et al*. (1997)
GRIM4-C4	1995	72	S, G, A	Schwintzer *et al*. (1997)
GFZ96	1996	359	PGM055, G, A	Gruber *et al*. (1997)
EGM96	1996	360	EGM96S, G, A	Lemoine *et al*. (1998)
GRIM5C1	1999	120	S, G, A	Gruber *et al*. (2000)
EIGEN-1	2002	119	S (CHAMP)	Reigber *et al*. (2002)
EIGEN-2	2003	140	S (CHAMP)	Reigber *et al*. (2003)
GGM02S	2004	160	S (GRACE)	Tapley *et al*. (2005)
GGM02C	2004	200	S (GRACE), G, A	Tapley *et al*. (2005)
EIGEN-GL04S1	2006	150	S (GRACE, LAGEOS)	Foerste *et al*. (2006)
EIGEN-GL04C	2006	360	S (CHAMP, GRACE), G, A	Foerste *et al*. (2006)
EIGEN-5S	2008	150	S (GRACE, LAGEOS)	Foerste *et al*. (2008)
EIGEN-5C	2008	360	S (CHAMP, GRACE), G, A	Foerste *et al*. (2008)
EGM2008	2008	2190	S (GRACE), G, A	Pavlis *et al*. (2008)

The first considered model is a combined gravity field model, GRIM4C1 reported by Schwintzer *et al*. (1991). This model was computed as a joint collaboration between DGFI and GRGS. The GRIM4C1 model was derived up to degree and order 50 in terms of spherical harmonics. It incorporated GRIM4S1 satellite-solution, mean gravity anomalies and Seasat altimeter derived mean geoid undulations. The OSU91A geopotential model was reported by Rapp *et al*. (1991). This model was an upgraded version of OSU89a and OUS89b. It was computed complete to degree and order 360 in terms of spherical harmonics in a blended form. In the computation of the OSU91A, coefficients to degree 50 were based on a combined solution from GEM-T2 model, surface gravity data and GEOSAT altimeter data. The remaining coefficients (51-360) were derived from a combined solution computed from terrestrial data, altimeter derived anomalies and the topographic anomalies.

The Joint Gravity Model 3 (JGM3) model released in 1994 was reported by Tapley *et al*. (1996). This model was developed by NASA/GSFC and the University of Texas at Austin as part of the Topex Poseidon (T/P) project. This combined model was derived by adding the

geopotential coefficients from the pre-launch model, JGM1 and their associated error covariance with GPS, SLR, DORIS tracking of T/P, laser ranging tracking of LAGEOS 2 and Stella and DORIS tracking of SPOT 2. The model was derived complete to degree and order 70. The GRIM4-S4 and GRIM4-C4 reported by Schwintzer *et al.* (1997) were developed as a joint collaboration between GFZ Potsdam and GRGS Toulouse/Grasse for requirements of geodetic and altimeter satellite missions. The GRIM4-S4 model was derived solely from satellite tracking data complete to degree and order 70. On the other hand, the GRIM4-C4 model was derived based on a least squares adjustment involving a combined solution from the GRIM4-S4 model and surface gravity data from gravimetric and altimeter measurements. This model was computed complete to degree and order 72, corresponding to a spatial resolution of 555 km at the surface of the Earth (Schwintzer *et al.*, 1997). The GRIM4-S4 and GRIM4-C4 models were thought to be efficient for satellite orbit computations especially with orbit altitudes exceeding about 800 km (Schwintzer *et al.*, 1997). The GFZ96 geopotential model, which was an upgrade of the GFZ93 and GFZ95 models, was reported to provide high resolution of GFZ derived models (Gruber *et al.*, 1997). This combined model was computed from the then improved terrestrial data derived from a 3-year ERS-1 mean sea surface and PMG055 solution. The solution was also combined with altimeter derived gravity anomalies and normal equations and potential coefficients of the GRIM4-S4 model as the *a priori* model. The GFZ96 model was derived to degree and order 359.

Lemoine *et al.* (1998) described the combined spherical harmonic model, EGM96, which is complete to degree and order 360 and corresponds to a global resolution of about 55 km. The EGM96 model was developed based on a joint collaboration between NASA Goddard Space Flight Centre (GSFC), the National Imagery and Mapping Agency (NIMA) and the Ohio State University (OSU). This is a blend model were three computational procedures were used. The spherical harmonic coefficients from 2-70 were derived based on a least squares adjustment involving satellite tracking data, terrestrial data and altimeter data of the ocean surface from the T/P, ERS-1, and GEOSAT missions and fill-in gravity anomalies in areas lacking data (Amos and Featherstone, 2003). From degree 71-359 the coefficients were computed from a combined solution based on normal equations derived from the satellite tracking data which were used as a priori values. The remaining coefficients at degree 360 were taken from a quadrature combined solution derived from the a priori satellite model and ERS-1/GEOSAT altimeter-derived

anomalies. The EGM96 geopotential model was believed to provide a more accurate reference surface for the topography as well as improve orbit determination for low orbiting satellites (Lemoine *et al*., 1998). The GRIM5C1 gravity field model reported by Gruber *et al*. (2000) was derived in a German-French joint collaboration between GFZ Potsdam and GRGS Toulouse. The model was computed up to degree and order 120. It incorporated terrestrial and airborne mean gravity anomalies, altimetric gravity anomalies from NIMA and mean gravity anomalies derived from the GRIM5S1 model.

Most of the geopotential models released from 2000 onwards are derived solely from CHAMP, GRACE and GOCE missions plus other satellites, terrestrial and altimeter data. Geopotential models generated from the inclusion of the three satellite missions data are believed to be more accurate when compared with the prior models (e.g., they allow, with an unprecedented accuracy and resolution, the recovery of the mean sea surface topography from the difference between an altimetry-based mean sea surface height model and the gravity model's derived geoid) (Dobslaw *et al*. 2004). The first CHAMP geopotential model, EIGEN-1 reported by Reigber *et al*. (2002) was derived in a German-French joint collaboration complete to degree and order 119. This model was derived by use of GPS tracking and three months on-board accelerometer data from CHAMP. The EIGEN-1 geopotential model was reported to resolve the geoid and gravity with an accuracy of about 20 cm and 1 mGal respectively at a half-wavelength resolution of 550 km (Reigber *et al*., 2002). The EIGEN-2 model reported by Reigber *et al*. (2003) was also derived in a collaboration between Germany and France. This satellite-only model was derived complete to degree and order 140. The model incorporated gravity orbit perturbations, exploiting GPS CHAMP satellite-to-satellite tracking and six months on-board accelerometer data. The accuracy in terms of geoid and gravity for the EIGEN-2 model was reported to be about 10 cm and 0.5 mGal respectively.

Similar to the CHAMP mission, the GRACE mission data set has enabled a homogeneous determination of the geopotential gravity field modelling. The first is the satellite-only model, GGM01S reported by Tapley *et al*. (2004b). The model derived to complete degree and order 120 incorporated GRACE tracking data spanning April to November 2002 adding to a total of 111 selected days and using least squares adjustment. The authors reported an error estimate accuracy of about 2 cm over the land and ocean regions. An improved geopotential model to GGM01 called GGM02 was released in 2005. This model exists both in the GRACE

based satellite-only, GGM02S and the combined model, GGM02C (Tapley *et al*. 2005). The combined geopotential model incorporated the GRACE-only model GGM02S with EGM96 plus 14 months of GRACE data spanning April 2002 to December 2003. It was computed to maximum degree and order of 200 in terms of spherical harmonics. Improvements by a factor of two were reported with error estimates of less than 1 cm geoid height to spherical harmonic at degree 70.

The satellite-only model, EIGEN-GL04S1 described by Foerste *et al*. (2006) has a maximum degree and order of 150. It incorporated GRACE-only (EIGEN-GRACE04S) and GRACE/LAGEOS (EIGEN-GL04S) solutions. EIGEN-GL04S1 was later combined with surface gravity data from altimetry over the oceans and gravimetry over the continents to derive a high resolution gravity model EIGEN-GL04C released in 2006 (Foerste *et al*., 2006). This combined gravity field model is an outcome of the joint gravity field processing between GRGS Toulouse and GFZ Potsdam. The satellite-part of EIGEN-GL04C is based on GRACE and LAGEOS data and the maximum degree and order of this model is 360 in terms of spherical harmonics. The EIGEN-5C model reported by Foerste *et al*. (2008) was also a joint collaboration between GFZ Potsdam and GRGS Toulouse. It is an upgrade of EIGEN-GL04C and has a maximum degree and order of 360. The model is again a combination of GRACE and LAGEOS tracking data combined with addition of gravimetry and altimeter surface data. Combination of the satellite and surface data have been done by combining normal equations obtained from observation equations for the spherical harmonic coefficients. The National Geospatial-Intelligence Agency (NGA) released the first ever global model capable of resolving the Earth's gravity field beyond spherical harmonic degree 2000, a model called EGM2008. A description of this model can be found in Pavlis *et al*. (2008). The EGM2008 gravity field model has a maximum degree and order of 2159. It incorporates improved gravity anomaly data, altimetry-derived gravity anomalies and GRACE based satellite solutions. It allows proper computation of quasigeoid heights, gravity anomalies and vertical deflections and has a spatial resolution of ~5 arc minutes or ~9 km in the latitudinal direction (Pavlis *et al*., 2008).

2.7. Concluding remarks

The continuous design and deployment of satellite missions dedicated to gravity field measurements and the availability of high-precision data have led to the availability of gravity

information with unprecedented spatial-temporal resolution and accuracy. In particular, the advent of satellite data has made it possible to determine the gravity field of the Earth via modelling. To this end, these data sets are the basis for robust gravity field modelling with more than 100 gravity field models released in the scientific community since the early 1960s. Different gravity field models could be characterized by various degrees of spatial-temporal resolution. Despite the many scientific milestones in gravity field modelling, a study evaluating many of the developed gravity field models in the context of POD by use of SLR data have remained inconclusive. In particular, there has not been new SLR analysis software with the capability of POD with sensitivity analysis of gravity field model options. The research work reported in this thesis demonstrates the capability of the SDAS package to investigate the contribution of the different gravity field models applied in POD.

3. Data and analysis

In every branch of knowledge the progress is proportional to the amount of facts on which to build, and therefore to the facility of obtaining data. James Maxwell

3.1. Introduction

This chapter contains a description of the data sources and management involved in SLR data collection (used in this research study). Firstly, the global network of SLR tracking stations is discussed mainly to highlight some of the factors affecting the accuracy of SLR data. The data collected from these tracking stations is discussed focusing on the main steps in data management (i.e. formation of SLR normal points) required to ensure that the collected data is adequate and in good format. In this chapter I also describe the general methods used throughout this project. For the sake of conciseness the analysis methods are described here and not repeated in each presented chapter. However, other chapters may contain methods that are chapter specific. Furthermore, the chapter explains some aspects (e.g., parameterizations) of the software used to analyse the SLR data.

3.2. Data

As already explained in Chapter 2, the main observable in SLR is the distance or range (round-trip, station to satellite and back). Together with this TOF, are other auxiliary (derived parameters) such as the correction information due to atmospheric effects, which are to be applied to the data. Raw SLR data are formatted at the remote station before transmission to operational data centres where the data are translated into the appropriate format. There are about six ILRS accredited analysis centres. Included are the NERC Space Geodesy Facility (NSGF), Joint Centre for Earth System Technology/Goddard Space Flight Centre (JCET/GSFC), Greenbelt, Maryland, USA, GeoForschungs Zentrum (GFZ) German Research Centre for Geosciences, Germany, Centro de Geodasia Spaziale (CGS), Italy, etc. Currently, SLR data are available in two forms: original observations (full-rate data) and compressed range observations generated from the original observations (these are called the normal points) (Noll, 2010).

Full-rate data sets include all the valid satellite returns and are often larger in volume. These data are not routinely provided by all stations in the laser tracking network. The data are useful for both engineering evaluation and scientific applications (e.g., studying the performance of retro-reflectors, discerning satellite signatures, understanding the statistical nature of satellite returns, calibration of satellite targets, validating system quality of laser station co-locations, etc.) (Noll, 2010). Full-rate data which range in size from 10 to 100 kbytes are transmitted to the Crustal Dynamics Data Information System (CDDIS) in files containing all data from a specific tracking station and satellite on a particular day. The CDDIS then combines the transmitted daily files from all tracking stations into a monthly satellite specific file. These files are then made freely available in the ILRS full-rate format in subdirectories by satellite and year.

Satellite Laser Ranging normal points constitute the primary ILRS data product (these products are archived at e.g., http://ilrs.gsfc.nasa.gov). The normal points are compressed data, i.e. the compression involves sampling over time based on certain minimum number of data points within the sampling interval. The length of this normal point interval is primarily dependent upon the satellite altitude; lower orbiting satellites have a shorter normal point interval than high orbit satellites. Normal points are computed via two steps. Firstly, the observed range with the computed reference ranges and thereafter a series of predicted residuals is generated. Suppose that d_0 represents the observed ranges and d_p are the computed reference ranges, the generated observation residuals can be described by Equation (64)

$$d_r = d_0 - d_p. \tag{64}$$

Previous studies have predicted that when the relative data density drops to a very low rate, it is plausible that the "time-isolated" measurements are highly dominated by noise or outliers (Seago, 1998). These outliers are often removed by using a suitable range or isolation window. To restrain the formation of time-isolated outliers into bad single-point normal points, ILRS analysis data centres often implement algorithms also known as a leverage point pre-filter that initially flags heavily leveraged points as noise (Seago, 1998). A datum is considered leveraged if it is the only observation within a specified time period (isolation window). The isolation window is arbitrarily chosen to be equal to either the recommended integration step size for a specific dynamic model integrator, or twice the normal point bin size. These values are passed

via a satellite data file containing other satellite specific parameters. The isolation windows for various satellites as estimated by Seago (1998) are presented in Table 3.

Table 3. Isolation intervals for leverage filtering

Satellite	Normal point bin (sec)	Isolation window (sec)
GFZ-1	5	60
ERS 1/2	15	60
Starlette	30	90
Ajisai	30	90
Stella	30	90
LAGEOS 1/2	120	240
Etalon 1/2	300	600
GLONASS	300	600

In order to remove systematic trends in the observation residuals, orbital parameters are often solved by fitting a trend function, $f(d_r)$, to the residuals d_r. The fit residuals which analyses any remaining outliers can be iteratively computed as given in Equation (65),

$$f_r = d_r - f(d_r). \tag{65}$$

In the second step of formation of normal points the resulting observed trajectory is segmented into fixed intervals or bins starting from 0^h UTC. The proposed interval sizes for various satellites are listed in Table 4.

Table 4. Examples of bin sizes for specific satellites

Satellite	Bin size (seconds)
GPS, GLONASS	300
LAGEOS 1/2	120
Starlette, Stella	30
ERS 1/2	15
GRACE	5

In each bin i, the mean value $\overline{f}_{r_i}$ of all deviations is computed and added to the trend function at the centre of the interval. The normal points representing all single observations of a given interval may be computed according to Equation (66),

$$NP_i = O_i - f_{r_i} + \overline{f}_{r_i}, \tag{66}$$

where O_i is an observation located in bin i and f_{r_i} represents fit residuals in the same bin. The ILRS normal point file format exists as uncompressed ASCII files containing a header record followed by a data record. A header record contains satellite and station designators, general station configuration information and normal point calculation parameters. The data record contains laser fire times in units of 0.1 μs, system delay in picoseconds, bin RMS, meteorological data (e.g., pressure, temperature and relative humidity) and number of ranges used in the normal point formation. Normal points may be computed either at the on-side tracking stations or at ILRS data analysis centres. The ILRS operational data centres forward normal point data to the CDDIS in hourly and daily files by satellite with a typical delay of less than one day following the observations. The CDDIS updates the received files containing all normal point data on a daily basis. Daily files contain all normal point data for each satellite received at the ILRS operational data centres in the previous 24 hour period. Thus, these daily files often contain data spanning several operating days. The monthly files contain all normal point data for each satellite during the month. Daily and monthly normal point data are available from the CDDIS in subdirectories by satellite and year and can be freely accessed at http://cddis.nasa.gov/.

The normal point data analyzed in this study were selected from ILRS tracking stations (Pearlman *et al*. 2002). Tracking stations were selected in order to ensure good global distribution. As mentioned earlier, global distribution of SLR stations is dense in US, Europe, and Australia. The Southern Hemisphere suffers from a lack of SLR tracking stations. This is one major disadvantage of SLR compared to other geodetic techniques such as VLBI, GPS and DORIS. In Africa there is only one active SLR tracking station situated in South Africa at HartRAO, joining other geodetic instruments (e.g., VLBI, GPS, and DORIS). The selection of the SLR stations is based on the number of daily normal points contributed by each station. Note that the daily normal points are not generally contributed by all the selected SLR stations rather the actual normal points per day are contributed by fewer stations. Stations with the highest number of points were selected.

3.3. Satellites

The data analysed was collected from LAGEOS 1 and 2 satellite missions. LAGEOS 1 was launched in 1976 by the American Space Agency, NASA in a near circular orbit. This satellite was later joined by a sister satellite, LAGEOS 2, launched during 1992 in a joint collaboration between United States and Italy. Both satellites have a high mass-to-area ratio of 1450 kg/m and orbit the Earth at an altitude of about 6000 km above Earth's surface. LAGEOS satellites carry a total of 426 corner cube reflectors inset in the outer aluminium shell surrounding a solid cylindrical brass core. These retro-reflectors are used to reflect laser beams which are reflected back to the ground stations. Each reflector is mounted with its front face perpendicular to the radius vector at the mounting point (Otsubo *et al*., 2004).

LAGEOS retro-reflectors are distributed in rings and equally spaced along lines of latitude (Fitzmaurice, 1977). The reflectors are arranged on the surface of the sphere in rows that form small circles parallel to the satellite's "equator" (circle perpendicular to the axis of rotation of the satellite) (Otsubo *et al*. 2004). These reflectors are symmetrically arranged in rows, each hemisphere (designated "N" and "S" hemispheres) having about 10 rows. The rows contain different numbers of reflectors, according to their "latitude" namely 32, 32, 31, 31, 27, 23, 18, 12, 6, 1, giving a total of 213 in each hemisphere (Otsubo *et al*., 2004.). A total of 422 of the LAGEOS reflectors are made of fused silica glass. The remaining four are made of germanium and they are used to obtain measurements in the infrared region of the spectrum. More properties of the two satellites are summarized in Table 5.

Table 5. Mission parameters of LAGEOS 1 and 2 satellites.

Properties	LAGEOS 1	LAGEOS 2
COSPAR ID	7603901	9207002
Launch date	May 4 1976	October 22 1992
Reflectors	426 corner cubes	426 corner cubes
Orbit	Circular	Circular
Orbit inclination	109.84^{0}	52.64^{0}
Eccentricity	0.0045	0.0135
Perigee height	5860 km	5620 km
Period	225 minutes	223 minutes
Weight	406.965 kg	405.38 kg

Figure 11 portrays the retro-reflectors of LAGEOS satellites. The LAGEOS series were designed to provide an orbiting benchmark for geodynamical studies of the Earth (http://ilrs.gsfc.nasa.gov). These include studies of Earth's gravity field, determination of EOPs and investigation of various geophysical phenomena such as tectonic plates, polar motion and tides (Smith *et al.* 1990; Sengoku, 1998; Bouille *et al.*, 2000). Due to their high mass-to-area ratio and attitude the LAGEOS orbits are less sensitive to Earth's gravity field and to non-gravitational forces. Thus they provide precise measurements of the satellite's position with respect to Earth. In addition the high altitude of the two satellites causes them to be sensitive up to degree 20 of the underlying gravity field model.

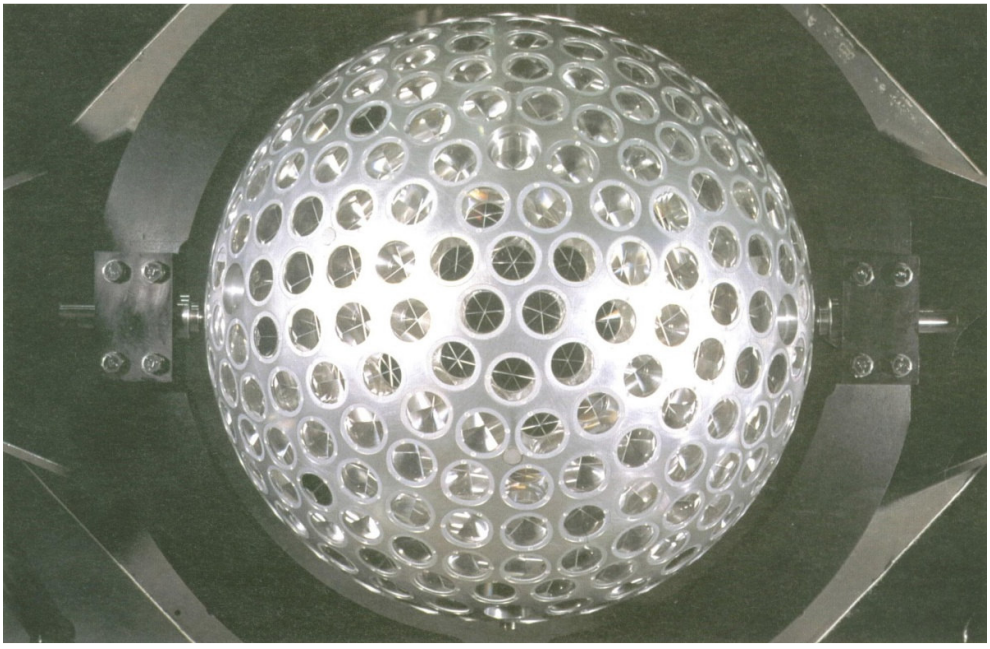

Figure 11. Retro-reflectors on LAGEOS satellite. http://ilrs.gsfc.nasa.gov.

Figure 12 illustrates the distribution of the normal point data analysed in one of the studies presented in this thesis. This time series comprises three years of SLR data, i.e. spanning December 2005 to December 2008. Figure 12 serves to illustrate a general distribution of normal points. The correct specifications on the data used are mentioned in relevant chapters. Typically there are between 200 and 400 normal points per day (for a total of ~15 stations) over a 24 hour satellite arc. Sometimes there are less, especially over international holiday periods (e.g. Christmas) and statistically there are less data available over weekend periods. This is due

to the fact that not all SLR stations operate in full 24x7 mode. A percentage (typically 10%-20%) of data can be filtered out statistically as outliers, depending on analysis strategy.

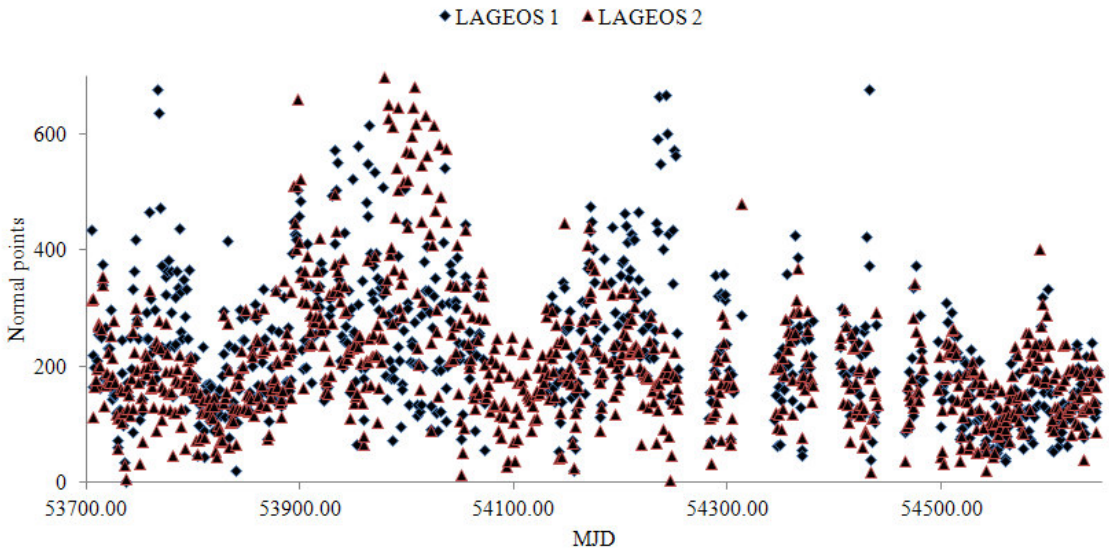

Figure 12. Distribution of normal points analysed.

3.4. SLR analysis software

The SLR data throughout this project was analysed using the SDAS package developed at HartRAO (Combrinck and Suberlak, 2007) mainly for POD and estimation of geodetic parameters. This software comprises the following main elements:

- Generation of initial setup files for the computation of SLR stations positions and their velocity solutions,
- Satellite orbit and parameter adjustment module for orbit improvement,
- Parameter estimation module which introduces constraints in the form of adjusting the outlier rejection term with a predefined weight.

The output solution includes the following:

- O-C RMS residuals, the mean and the standard deviation (SD) of the O-C residuals,
- Components of the stations' positions and their velocities,
- Empirical coefficients for atmospheric drag, solar radiation pressure, Earth's elasticity, Earth's albedo, once-per-cycle per revolution empirical parameters (9 coefficients) and coefficients of un-modelled components,

- Time and range bias values,
- Gravitational spherical harmonic coefficients (solve-for parameters) such as J_2 to J_5, S_{21} and C_{21}.

3.4.1. Software parameterization

The SDAS package utilises the station and satellite coordinates provided by the IERS and ILRS in the ITRF. These satellites coordinate a-priori values can be selected from a menu to be at a specific epoch, such as ITRF2000 and SLRF2005. The satellite coordinates incorporated in ITRF2000 were integrated by using primary core stations observed by VLBI, LLR, SLR, GPS and DORIS and were also densified by regional GPS networks in Alaska, Antarctica, Asia, Europe, North and South America and the Pacific. On the other hand, coordinates in ITRF2005 were constructed by using long-term input data in the form of time series of station positions, velocities and EOPs. These input solutions are provided as a weekly sampling by the IAG International Services of satellite techniques: the International GNSS Service (IGS) (Dow *et al.*, 2005), the ILRS (Pearlman *et al.*, 2002) and the International DORIS Service (IDS), (Tavernier *et al.* 2006), and in a daily basis by the International VLBI Service (IVS) (Schlueter *et al.*, 2002).

The SLRF2005 reference frame is a dedicated reference frame derived from a combination of ITRF2000, rescaled ITRF2005 and a global SLR solution based on data spanning 1993 to 2007 with new SLR stations included (for further details on combination strategy used to derive SLRF2005, see for example, http://ilrs.gsfc.nasa.gov/working_groups/awg/SLRF2005.html and Luceri and Bianco, 2008). The satellite a-priori coordinates are provided by the ILRS in the consolidated prediction format (CPF). During data processing, both satellite and SLR station position vectors are transformed to a non-rotating (inertial) frame, the International Celestial Reference Frame (ICRF). The ICRF is a geocentric inertial coordinate system, defined by the precise J2000.0 equatorial coordinates of extragalactic radio sources determined from VLBI measurements (Johnston and de Vegt, 1999). The J2000 standard reference epoch is given by 01-Jan-2000 12:00:00 ephemeris time. This is the beginning of the Julian year 2000, and corresponds to a Julian date of 2451545.0. The fundamental inertial frame definition uses the Earth as the reference body, its mean equator as the reference plane, the vernal equinox of its

mean orbit as the reference direction, and J2000 as the reference epoch. Hence, this frame is called the Earth Mean Equator and Equinox of Epoch J2000 (also known as EME2000) (Lyons and Vaughn, 1999).

The Jet Propulsion Laboratory (JPL) DE-405 planetary ephemeris (Standish, 1998), which is based on the ICRF inertial coordinate system has been utilised to determine exact vectors and distances to solar system objects and to account for the gravitational perturbations on the satellite orbit by the Sun, Moon and planets. These coordinates have been converted from barycentric inertial to geocentric inertial. In ICRF inertial coordinate system algorithms are designed to maintain three directions of orthogonal axes:

- The Z axis (Z_{J2000}) is the unit normal to the Earth's mean equator of epoch J2000
- The X axis (X_{J2000}) is chosen to be the vernal equinox, the node with the Earth's mean orbit plane where the orbit ascends through the equator plane for the J2000.
- The Y axis (Y_{J2000}) is chosen to complete the right-handed orthogonal coordinate system

The vector axes are shown in Figure 13 and are used as the basis for expressing the positions and velocities of satellites in space.

The SLR tracking station coordinates which are normally expressed in the Earth-fixed, geocentric, rotating systems are transformed to the ICRF reference frame by taking into account precession and nutation of the Earth, its polar motion and the UT1 transformation. The relation between the ICRF and the ITRF may be described by Equation (67),

$$\vec{X}_{ICRF} = PNTXY.\vec{X}_{ITRF}. \qquad (67)$$

In this equation P is the precession matrix, N is the nutation matrix, T is a matrix expressing the rotation by true sidereal time S and XY are the transformation matrixes from the terrestrial frame to the frame connected to the instantaneous ephemeris pole, $\vec{X}_{ICRF}$ and $\vec{X}_{ITRF}$ are the vectors relating to ICRF and ITRF axes respectively. The data obtained from the IERS and Bulletin B (actually file eopc04_62.now, consistent with ITRF2005) were utilised, with all values interpolated via polynomial fits to the epoch of SLR measurement. Bulletin B of the IERS provides current values of the EOPs in the IERS Reference System. While Bulletin A gives an advanced solution of EOPs as well as predictions updated on a weekly basis, the standard solution is given on weekly basis in Bulletin B. Details of file eopc04_62.now can be

obtained at http://hpiers.obspm.fr/iers/eop/eopc04_05/ in the document C04_05.guide. The EOP values provide an exact link between the ICRF and the ITRF.

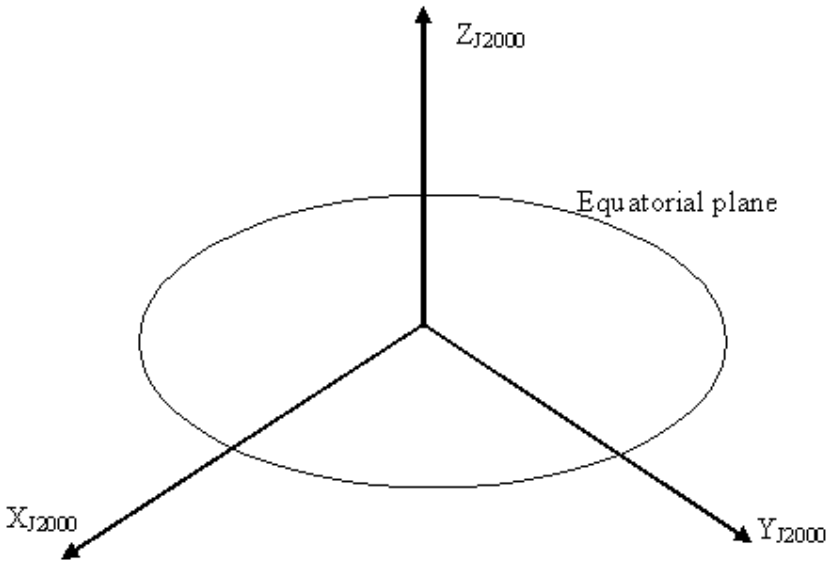

Figure 13. The J2000 inertial reference frame.

During data processing the software conforms to the IERS96 conventions as far as precession and nutation of the Earth's polar motion is concerned. For example, the model of the Earth's precession and nutation specifies the 1976 International Astronomical Union (IAU) precession (Lieske *et al*., 1977; Lieske, 1979) and the 1980 IAU nutation formula (Seidelmann, 1982). The software utilises the UT1-UTC values as provided by IERS Bulletin B database (http://hpiers.obspm.fr/eoppc/bul/bulb_new) or eopc04_62.now.

The SLR tracking stations' positions are affected by fluctuations in the position of the axis of the Earth's crust. Such fluctuations are due to horizontal and vertical displacements resulting from the solid Earth tidal perturbations as well as from large scale motions of Earth's lithosphere (tectonic plate velocity). Displacements of the tectonic plate motions can be accounted for by calculating the plate velocity using ITRF station velocities and adjusting the stations' positions in the ITRF to the epoch of the SLR measurements (see for example Combrinck and Suberlak, 2007). Tidal forces (solid and ocean) arise from changes to the Earth's geo-potential induced by variations in the mass distribution of Earth. Contributions to the solid Earth tide force arise from the gravitational effects of the Sun and Moon, which deform the

shape of the Earth. Other effects result from ocean loading on the crust and wobbles of the mantle and core region. Station displacements due to solid Earth tides were accounted for according to the model reported in Petrov (2005). Ocean loading is modelled by the ocean tides, whence our analysis utilised a model derived by Scherneck (1991). Atmospheric and pole tides were accounted for in accordance with IERS conventions 2003 (McCarthy and Petit, 2003). In the SLR analysis reported in this thesis, the transformation of the COM corrections of satellites was not considered although it is a selectable option in the software. In general a total of 48 parameters were adjusted during SLR data processing. The main standard parameters are the position and velocity of the satellite, solar pressure coefficient (set at 1.13), satellite drag coefficient (set at 4.9) and Earth albedo coefficient (set at 0.34). All the implemented models were aimed at achieving optimal solutions thereby minimising the O-C residuals (this is the main parameter in POD). In summary, the parameters considered during data processing are listed in Table 6.

Table 6. Constants, reference frames and empirical models used in the SLR data processing.

N_{max}	20×20
Inertial reference frame	J2000
Pole-tide correction (station position)	IERS 2003
Relativity (space-time curvature)	IERS 2003
Earth–tide correction (station position)	Petrov 2005
Earth-tide acceleration of satellite	(Rizos and Stolz, 1985)
Ocean loading correction (station position)	Scherneck, 1991
Atmospheric loading	Special Buro for Loading, IERS
Tectonic plate model	ITRF2000 velocity field
Earth orientation	a-priori Earth orientation parameters and UTC-UT1 values as per IERS extrapolated to observation epoch
O-C outlier rejection	Selectable
Satellite centre-of-mass offset (LAGEOS)	251 mm, ILRS standard value (Otsubo and Appleby, 2003)

3.5. Data analysis

A schematic representation of data analysis followed throughout this project is given in Figure 14. The SDAS package utilises a dynamical data analysis procedure (this is the dynamic orbit determination discussed in Chapter 2) where the satellite's equations of motion i.e. gravitational

and non-gravitational forces are taken into account. Using this method is advantageous since it does not only determine the satellite orbits, but also improves or estimates the force models such as the Earth's gravity field model. Also given that the force model can accurately describe the movement of an orbiting satellite, the least-squares solution method can be used to reduce the orbit error caused by measurement noise or errors. However, in this case the orbit accuracy is highly dependent on force models used for dynamic orbit determination. The analysis procedure involves numerical integration of the LAGEOS equations of motion from nominal initial conditions within a given force field and reference frames as listed in Table 6. A linear system of normal equations is set up and its solution is computed. The software computes derivatives of the observations with respect to the "solve-for parameters" of interest by integrating the equation of motion and solving for the unknown parameters using a least-squares adjustment. The procedure is iterated (e.g. 20 times) until convergence is reached, presumably on the last selected iteration number. During the data processing, the orbital arc integration length[8] was fixed at 24 hours. Although short arcs are mostly affected by various discontinuities, in this study it was chosen considering the density of the analysed data as well as the possibility of reducing some of the discontinuities through smoothing procedures. In addition, a short arc length was selected in order to prevent the increase of residual errors in non-gravitational accelerations.

[8] An orbital arc integration length may be defined as the interval of time from the initial point to some chosen final point of specific repeated period of satellite tracked data.

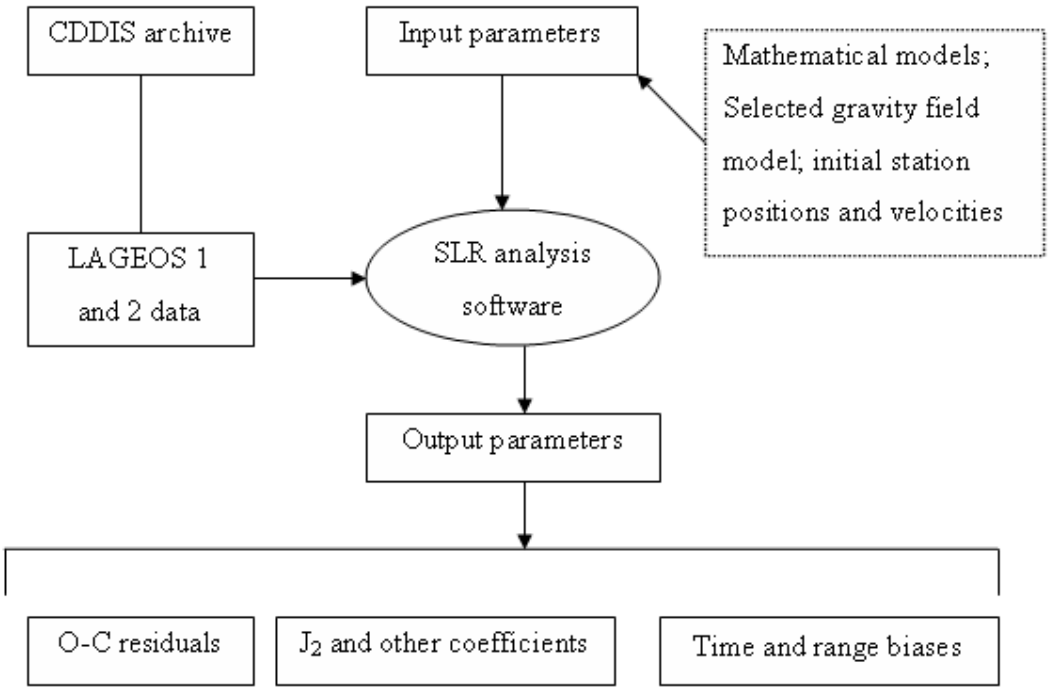

Figure 14. Schematic representation of data processing

3.6. Concluding remarks

SLR tracking data particularly from LAGEOS satellites have over the years allowed precise determination of satellite orbits as well as the investigation of orbital perturbations and their possible origins. About 30 SLR tracking stations coordinated by the ILRS are mostly distributed in European, Australian and Asian countries, this concentration of stations in the Northern Hemisphere has an impact on results as the network geometry is weakened and often data are not captured if one or more of the few Southern Hemisphere stations are not operational. Currently the accuracy of SLR data range between 1 cm and 3 cm for good tracking stations. However the accuracy decreases to 5 cm or more in some cases. In this study LAGEOS 1 and 2 data collected from selected tracking stations were analysed using the SDAS package developed at HartRAO. The analysis of SLR data requires adequate modelling of the orbit via an orbit integrator that includes modelling of gravitational and non-gravitational forces perturbing the orbit of the satellite. In order to adjust the range as determined by the SLR system, corrections due to physical effects such as those caused by the solid Earth tide and tidal deformations on the

static gravity field need to be made. The SDAS package at HartRAO takes into account all the mathematical models in order to achieve a suitable solution. In the following chapters results obtained from LAGEOS 1 and 2 data analyses are discussed.

4. Investigating the accuracy of gravity field models using satellite laser ranging data

"...the various models are not as good as they are said to be. If they were, the differences between them should not be as great as they are..."

Lambeck and Coleman (1983).

The following chapter is based on a paper by Botai and Combrinck (2011).

4.1. Introduction

In this chapter, improvements in gravity field modelling over a period of 18 years are studied based on SLR data analysis using the SDAS package. In particular, this analysis is concerned with investigating the accuracy of GGMs focusing on spherical harmonic coefficients up to degree and order 20. In addition, since SDAS is still under development the present analysis is also to investigate whether SDAS output (e.g., O-C residuals and J_2) compares with outputs from other existing SLR analysis software packages such as GEODYN. The O-C residuals computed during SLR data analysis utilizing various gravity field models are used as a proxy for the accuracy of the satellite orbits and thus a measure of improvement in gravity field modelling. In this study three different analyses were conducted:

a) Seven months of SLR data collected from LAGEOS 1 and 2 were analysed by considering 12 gravity field models. Here, the main goal was to review the general improvement in gravity field modelling.
b) Three years of LAGEOS 1 and 2 data were analysed in order to investigate the trend in the improvement in the range bias associated with gravity field models derived from 1996 to 2008.
c) Lastly, the analysis of SLR tracking data sets for LAGEOS 1 and 2 (here 26 months of data) also focused on investigating improvements in the SDAS package based on two recent gravity field models.

Based on our analysis, there has been a factor of ~2 improvement in the SLR range bias computed from LAGEOS 1 and 2 SLR data analysis based on gravity field models developed from 1990 to 2008. However from the analysis of the O-C range residuals, the majority of the gravity field models released from 1999 exhibit negligible improvement. Models developed

between 1999 and 2008 depict subtle differences of O-C residuals across the analysed models suggesting stability in the accuracy of gravity field modelling according to the SDAS package. Furthermore, using the most recent version of SDAS, gravity field models have shown significant improvements (the current value of O-C residuals is ~1.5 cm to 2.0 cm) compared to earlier versions of the analysis software.

4.2. Background

Continuous tracking of geodetic satellite orbits using the SLR data have provided an unprecedented opportunity in the history of gravity field modelling. The GGMs derived from such observations allow researchers to probe the long- to medium-wavelength components (half-wavelengths longer than 200 km, or spherical harmonic degrees 2 to 100) of the Earth's gravitational field. Numerous gravity field models have been derived from the mid-1960s. Furthermore, gravity field modelling is still in progress with new models being derived and old models being modified continuously. The accuracy of most of the latest models in terms of precise orbit determination is currently at cm level.

Improvements in gravity field modelling in terms of accuracy and spatial resolution is necessary in order to understand the physics of the interior of the Earth, the dynamics of the ocean and the interaction of continents, ice and ocean in sea-level studies, as well as for a better determination of satellite orbits and height systems in science and engineering (Rummel *et al.*, 2002). Such improvements are warranted owing to the availability of SLR tracking data, especially from the low Earth orbiting satellites. Satellite missions such as CHAMP, GRACE and GOCE launched in 2000, 2002 and 2009 respectively are believed to have improved the spatial resolution, sensitivity and accuracy of the newly developed GGMs. These satellites are designed to resolve the long-wavelength part of the gravity field and hence provide unprecedented accuracy (Featherstone, 2003). In contrast to the sporadic tracking by the SLR station network of the ILRS, the three satellite missions (CHAMP, GRACE and GOCE) carry GPS receivers on board that allow continuous orbit tracking. Furthermore, these satellites are equipped with accelerometers which provide direct measurements of the non-conservative forces (e.g. air-drag). In the case of GOCE, six accelerometers are installed in a gradiometer arrangement which additionally allows for direct measurement of the Earth's gravity gradients which gives an improvement in the medium wavelength part of the gravity. The three satellite

missions also provide a homogeneous and near complete global coverage of gravity field information.

Research focusing on gravity field modelling has led to the unprecedented improvement in the resolution of various gravity field models i.e., to higher degree and order spherical harmonics. Such improvements can be measured by studying the inherent characteristics (e.g., the statistics) of the GGMs based on several factors. For example, the behaviour of GGMs can be analyzed by performing orbit adjustment tests on artificial satellites, GPS/leveling tests, comparing spectral behaviour of the models or ocean geoid (Foerste *et al*., 2008). While earlier geopotential models derived up to degree and order 70 could resolve spatial features (geoid computation) at a half-wavelength of about 290 km, models (particularly the most recent) computed up to degree and order 360 can resolve spatial features down to 55 km (Moore *et al*. 2006). Now-a-days gravity field modelling has reached a new era where new gravity field models are being derived reaching even higher degree/order (1000 or more) providing even further unprecedented accuracies, see for example Pavlis *et al*. (2008).

Early evaluations of gravity field models by Zhang and Featherstone (1995) reported that the OSU91A geopotential model provided the best fit to the gravity field over the Australian region compared to prior released models. In contributions by Pearse and KearsIey (1996) and Kirby *et al*. (1998) the accuracy of the OSU91A gravity model was inferior to the EGM96 gravity model where the latter was reported to give better solutions for the computation of geoid heights. Evaluations of GGMs released between 1996 and 2002 by Amos and Featherstone (2003) based on comparisons of gravity anomalies, free-air gravity anomalies, geoid heights and GPS/levelling tests found that EIGEN-1S was the best satellite-only GGM when applied in the Australian and New Zealand region while the best combined GGM over the same region was reported to be PGM2000A (Pavlis *et al*., 2000). The quality of the GGM01 model was assessed by Ellmann (2004) based on a comparison with the combined gravity field model EGM96. It was reported that the GGM01 model gives better solutions of gravity anomalies and geoidal heights over Fennoscandia (e.g., Finland, Germany, Norway, and Sweden) and the Baltic Sea region.

As reported in Foerste *et al*. (2009), a comparison study of ten geopotential models (EGM96, GGM02C, GGM03S, ITG-GRACE03, JEM01-RL03B, EIGEN-GL04C, EIGEN-5C/5S and EGM2008) using geoid heights and GPS/leveling data points revealed that the

EGM2008 model provided the best solution compared with the other models at degree 360. A much improved solution was also reported for EGM2008 when its coefficients were increased to degree 2190. A similar study by Yilmaz *et al.* (2010) evaluating GGMs EGM96, EIGEN-5C and EGM2008 based on the comparison of geoid heights with the GPS/levelling over Afyonkarahisar in Western Turkey also confirmed the improvements of EGM2008 model in the computation of geoid heights.

Improvement in the Earth gravity field modelling is anticipated as new and qualitative SLR tracking data and new algorithms of processing the data become available in the future. This expectation therefore motivates for assessment and validation of the accuracy and precision of existing gravity field models. Orbit tests are considered as tools for testing the long wavelength components of the gravity field model. In particular, the quality of orbits (and indirectly the quality of gravity field models) can be obtained by computing orbits to a variety of low and high artificial satellites with different orbit parameters. This can be done via a dynamic approach as well as by analysing the statistics of the satellites orbital residuals (also known as the difference between the observed orbital elements and the computed ones, e.g., O-C range residuals) for available tracking data to such satellites. In this study, we evaluate the accuracy of gravity field models in terms of POD by analyzing different data sets from LAGEOS 1 and 2 SLR data. In addition, improvements in the SDAS package are also investigated by analyzing 26 months of LAGEOS 1 and 2 SLR data considering two recent satellite-only and combined gravity field models.

4.2. Analysis of gravity field models

4.2.1. Improvements in gravity field modelling

In this section of the study, seven months of SLR data collected from LAGEOS 1 and 2 and spanning December 2005 to June 2006 were analysed for the purpose of assessing general improvements in gravity field modelling. In particular, twelve (12) gravity field models comprising of satellite-only and the combined (satellite and terrestrial data) categories which were developed and released to the geodetic community between 1990 and 2008 were considered during the SLR tracking data analysis. A brief description of each of these models is presented in Chapter 2 and a summary is also given in Table 7.

Table 7. GGMs evaluated in this study. Data: S = Satellite tracking data, G = Terrestrial gravity data, A = Altimetry data.

Model	Year	Degree/order	Data	Reference
AIUB-GRACE01S	2008	120	S	Jaeggi *et al.* (2008)
EIGEN-5C	2008	360	S,G,A	Foerste *et al.* (2008)
EIGEN-5S	2008	150	S	Foerste *et al.* (2008)
GGM03C	2007	360	S,G,A	Tapley *et al.* (2007)
EIGEN-GL04S1	2006	150	S	Foerste *et al.* (2006)
EIGEN-CG03C	2005	360	S,G,A	Foerste *et al.* (2005)
EIGEN1	2002	119	S	Reigber *et al.* (2003)
GRIM5C1	1999	120	S,G,A	Gruber *et al.* (2000)
EGM96	1996	360	EGM96S,G,A	Lemoine *et al.* (1998)
JGM3	1994	70	S,G,A	Tapley *et al.* (1996)
OSU91A	1991	360	GEMT2,A,G	Rapp *et al.* (1991)
GRIM4C1	1990	50	S,G,A	Schwintzer *et al.* (1991)

The data processing technique is discussed in Chapter 3. The stations selected for data analysis and their global performance during the period between 2006 and 2008 are listed Table 8. As featured in Table 8, ILRS tracking stations (column 1) have different total passes per year (i.e., different data volumes which is generally determined by ILRS scheduling program) and the annual averaged data quality (which is influenced by the local atmospheric conditions at the SLR site). Stations which were not able to provide any data or provided insufficient data were not evaluated.

In general, Table 8 illustrates that there has been an improvement in SLR tracking data over the years. It is important however to note that the individual station data are distributed heterogeneously with respect to the length of the time span and to the available number of normal points. For example while the best tracking stations observed about 2000 passes for LAGEOS (e.g., at Yarragadee) more than half of the 19 SLR stations selected delivered less than 15% of that data amount (e.g., Katzively and Lviv tracking stations). Nowadays the accuracy of data collected from ILRS tracking stations ranges from the 1 cm-level (for stations which perfom well) up to 3 cm-level for those stations that generally underperform. It is however important to also underline that the local atmospheric conditions such as the fraction of cloud cover, as well as turbulence degrade the quality of the data recorded at the SLR sites.

Table 8. Performance parameters of global SLR tracking stations recovered from the ILRS website i.e., http://ilrs.gsfc.nasa.gov/stations/site_info/. The stations are listed based on data volume contributed from 2006 to 2008, a map showing the distribution of these stations is given in Figure 5.

Station Name	Station No.	LAGEOS data volume			LAGEOS data quality [mm]		
		2006	2007	2008	2006	2007	2008
Yarragadee	7090	2038	1799	2078	9.1	9.5	9.6
Zimmerwald	7810	1147	1192	74	12.2	17.6	11.0
Graz	7839	858	825	653	7.7	8.0	5.2
Wettzell	8834	978	1041	1011	15.6	18.5	18.5
Monument Peak	7110	894	484	363	14.5	15.9	16.0
Herstmonceux	7840	929	932	426	16.3	12.9	13.5
Changchun	7237	423	772	605	14.3	17.5	12.4
Matera_MLRO	7941	872	753	799	6.5	5.9	4.9
Hartebeesthoek	7501	720	304	254	8.9	10.4	10.5
Potsdam_3	7841	307	304	313	20.1	19.2	17.4
Greenbelt	7105	269	321	511	9.1	9.5	9.9
San_Fernando	7824	260	523	440	14.7	15.1	14.1
Concepcion_847	7405	590	1078	816	14.5	12.0	19.2
McDonald	7080	369	412	335	11.8	12.5	12.5
Beijing	7249	178	339	311	19.4	16.6	16.3
Riga	1884	98	111	57	13.0	12.0	12.4
Katzively	1893	80	287	310	8.3	40.2	42.5
Tokyo-(CRL)	7308	63	248	472	17.4	15.5	15.0
Arequipa	7403	37	218	130	7.0	6.9	5.6

In this study we have computed orbit residuals for LAGEOS 1 and 2 using the SDAS package and considering the 12 selected gravity field models (see Table 8). The orbit residuals are derived from the SLR data analysis which utilizes dynamical modelling (e.g., gravity fields) during precise orbit determination (Yunck, 1997; Lemoine *et al.*, 1998). In particular, orbit residuals (which also represent the differences between the satellite position as calculated from SLR observations and the satellite position (orbit) computed from dynamical models) are commonly referred to as the O-C range residuals which are dependent on the type of gravity field model under consideration (different gravity field models are associated with different O-C range residuals). The computed O-C residuals are used in this study as a measure of accuracy in the gravity field modelling.

Table 9 contains the mean SD values of the O-C residuals based on the 12 considered gravity field models. The results presented in Table 9 indicate that the oldest gravity field

models, GRIM4C1 and OSU91A (released in 1990 and 1991 respectively) are linked to a mean residual (~10 cm and ~8 cm for LAGEOS 1 and 2 respectively) that is approximately twice the O-C range residuals computed from SLR analysis using some of the more recent models. Higher SD values associated with gravity field models (GRIM4C1 and OSU91A) may be due to the systematic errors or range bias in the ephemeris and/or as a result of inappropriate calibration of the models (Milani *et al*., 1995). The gravity field models released from 1999 onwards seem to remain at approximately the same level, although there are many specific differences (e.g. type of data used, degree and order of coefficients) amongst these later models.

Table 9. Statistical comparative accuracies of the evaluated gravity field model in terms of O-C residuals.

Model	Year	Mean SD [cm] LAGEOS 1	Mean SD [cm] LAGEOS 2
AIUB-GRACE01S	2008	3.79	3.63
EIGEN-5C	2008	3.89	3.73
EIGEN-5S	2008	3.85	3.32
GGM03C	2007	3.88	4.86
EIGEN-GL04S1	2006	3.89	3.72
EIGEN-CG03C	2005	3.81	3.69
EIGEN1	2002	6.09	7.52
GRIM5C1	1999	3.82	3.70
EGM96	1996	4.14	4.41
JGM3	1994	4.49	5.57
OSU91A	1991	10.17	8.10
GRIM4C1	1990	10.36	9.94

The average difference among the gravity field models released between 1999 and 2008 is at mm level with maximum difference being less than 2%. This may imply that gravity field models released from 1999 to 2008 have less or no influence on the current cm accuracy level of the precise orbit determination. However, since the addition of CHAMP and GRACE data, an improvement in gravity field modelling is expected, though systematic errors might be dominant in the analysis set up. In the case where modelling errors dominate, the inaccuracies caused by the modelling of other perturbing forces are greater than the contribution from gravity field models and thus obscure the improvement in the gravity modelling. Nevertheless, with the inclusion of long term series of data there still could be room for further improvements in the models.

Figure 15 depicts the mean SD values of the O-C residuals computed from LAGEOS 1 and 2 SLR tracking data based on varying the 12 selected gravity field models. In general, gravity field modelling progressively improved between 1990 and 2008. Noticeable improvements occurred with the development of gravity field models that were released between 1990 and 1996. For example, while the GRIM4C1 and OSU91A models exhibit SD mean values of ≥8 cm the most recent models show an SD of ~3 cm. Based on the SLR analysis of LAGEOS 1 and 2 SLR data, the mean SD values corresponding to the 12 gravity field models indicate that gravity field modelling significantly improved over the 18 years period.

Large mean SD values of O-C range residuals observed in earlier GRACE gravity field models, EIGEN1, may be explained by inherent systematic errors in the SLR observations, uncertainties in the conceptual gravity field model, model error, as well as outliers related to weak station geometry and lack of data on some days. Overall, an improvement by a factor of 2 in the O-C range residuals based on the analysis of the LAGEOS 1 and 2 data sets considering the various gravity field models is observed since 1990. In particular, the satellite-only gravity field models, AIUB-GRACE01S and EIGEN-5S, yield the lowest O-C results therefore they seem to be the most accurate in terms of our evaluation.

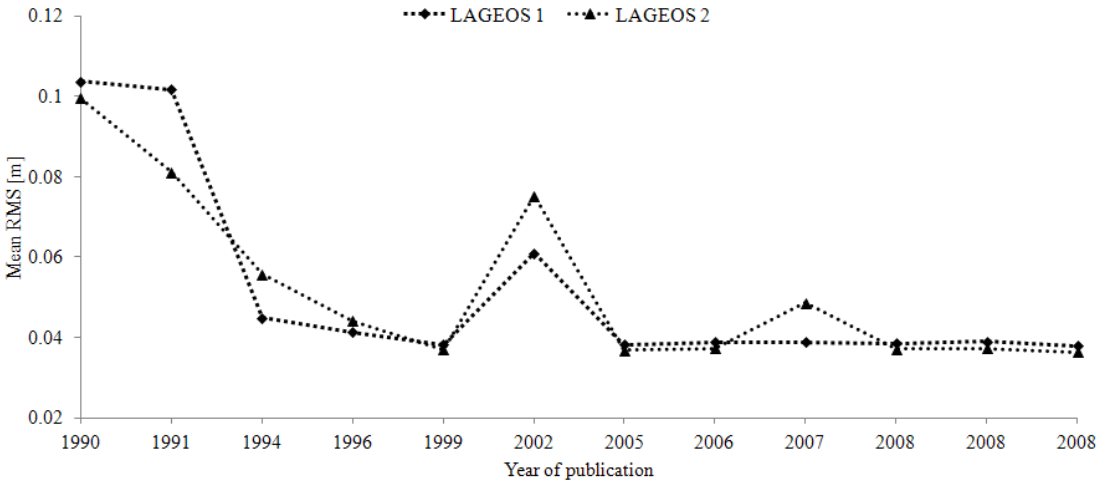

Figure 15. Time series of the mean SD values for the 12 evaluated GGMs.

Handling outliers in the O-C residuals based on selected gravity field models

In this part of work, the inherent outliers in the O-C residuals across the 12 selected gravity models have been assessed and corrected based on the 3σ-rule. This rule uses the fact that 99.73% of all values of a normally distributed parameter fall within three standard deviations of the average value. Suppose that we have a sample of O-C residuals given by $X = \{x_1, x_2, x_3, ..., x_n\}$, outliers in the data can be identified by iteratively applying the outlier tests given by Equation (68),

$$t_i = \frac{|\bar{x} - x_i|}{s}. \tag{68}$$

Here $\bar{x}$ is the mean, s is the standard deviation for the entire data set, x_i is the suspected single outlier, i.e., the value furthest away from the mean. Normally, a 3σ-rule considers any observations with $|t_i| > 3$ as possible outliers and discards such observations or adjusts them to one of the values $\bar{x} \pm 3s$, whichever is nearer. Another way of detecting outliers in the data is by fitting a linear regression on the data. Suppose the relationship between two variables x and y: (x_i, y_i), with i = 1, …, n is given by a straight line regression model,

$$y_i = \alpha + \beta x_i + u_i, \qquad i = 1, ..., n. \tag{69}$$

Here x_i and y_i are the predictor and response variable values respectively, and u_i are random errors. Possible outliers can be detected by estimating the parameters α and β with the least-squares estimates given by Equation (70),

$$\begin{aligned} \vec{\beta} &= \frac{\sum_{i=1}^{n}(x_i - \bar{x})(y_i - \bar{y})}{\sum_{i=1}^{n}(x_i - \bar{x})^2} \\ \alpha &= \bar{y} - \bar{x}\vec{\beta}. \end{aligned} \tag{70}$$

The 3σ-rule given by Equation (68) was used to investigate possible outliers in the O-C residuals computed from LAGEOS 1 and 2 SLR data based on the 12 gravity field models listed in Table 7.

Table 10 lists the new mean SD values of the O-C residuals computed by using LAGEOS 1 data after applying the 3σ-rule. A significant improvement in the mean SD of O-C residuals is noticed in all 12 gravity field models. In particular, the positive influence of the gravity field models on the O-C range residuals is more noticeable in all the models in the LAGEOS 1 data analysis. For example, the mean SD values computed from LAGEOS 1 based on GRIM4C1 and OSU91A ranges between ~6 cm and ~8 cm respectively. Application of the 3σ-rule on the O-C residuals derived from LAGEOS 1 indicates that ~6% and ~5% of the residuals were rejected as outliers. The combined gravity field model, EIGEN1 exhibits a high mean SD with data rejection of only 2% as compared to the other more recent models (models derived from CHAMP and GRACE data).

The mean SD values for the rest of the models lie at ~3 cm with range residual rejection ranging from 8% for JGM3 to ~27% for EIGEN-5S, EIGEN-5C and AIUB-GRACE01S. The AIUB-GRACE01S, EIGEN-5C, EIGEN-5S, EIGEN-CG03C and GRIM5C1 seem to be the best considering their reduced SD values, though they also reject a high quantity of data. In particular, the GRACE satellite-only model, AIUB-GRACE01S, is found to be the best with the least mean SD of 3.07 cm. It is however important to point out that, the percentage of data rejection is a function of the number of data points, as opposed to the variance of the O-C range residuals (here, older gravity field models have less data points compared with the most recent gravity field models).

Table 10. Mean SD values of the O-C residuals computed from LAGEOS 1 based on the 12 gravity field models after the application of the 3σ-rule.

Model	Mean SD [cm] LAGEOS 1	Residuals rejection %
AIUB-GRACE01S	3.07	26.8
EIGEN-5C	3.15	26.7
EIGEN-5S	3.18	27.4
GGM03C	3.29	15.4
EIGEN-GL04S1	3.25	20.7
EIGEN-CG03C	3.12	25.3
EIGEN1	5.16	2.1
GRIM5C1	3.13	25.1
EGM96	3.86	1.0
JGM3	3.81	8.3
OSU91A	8.38	4.9
GRIM4C1	6.87	5.9

Table 11 presents results for the 3σ-rule applied on O-C residuals computed from LAGEOS 2 based on the 12 selected gravity field models. In Table 11 the GRIM4C, OSU91A and EIGEN1 contain the highest mean SD values of ~8 cm and ~6cm with ~3%, ~4% and ~5% residual rejection. In particular, the EIGEN1 model exhibits a higher mean SD than any other recent models computed from CHAMP and GRACE data. The combined models, JGM3 and GGM03C are very close with a mean SD of ~4.7 cm and ~4.2 cm and residual rejection of ~3% and ~2% respectively. The rest of the gravity field models show an average SD of ~3 cm with residual rejection ranging from ~0.5% to ~1%. In particular, the EIGEN-5S, EIGEN-5C, EIGEN-GL04S1 and EIGEN-CG03C models exhibit equal average SD values of 3.30 cm with residual rejection of 0.48%. Since EIGEN-5S solution was incorporated in the computation of EIGEN-5C it may imply that the EIGEN-5C model and perhaps EIGEN-CG03C are dominated by the satellite-only information up to a certain degree/order. Based on this study the best model for computing LAGEOS 2 orbits is found to be AIUB-GRACE01S (similar to LAGEOS 1) considering the improvements in O-C residuals.

Table 11. Mean SD values of the O-C residuals computed from LAGEOS 2 based on the 12 gravity field models after the application of the 3σ-rule.

Model	Mean SD [cm] LAGEOS 2	Residuals rejection %
AIUB-GRACE01S	3.23	0.49
EIGEN-5C	3.30	0.49
EIGEN-5S	3.30	0.48
GGM03C	4.16	2.00
EIGEN-GL04S1	3.30	0.48
EIGEN-CG03C	3.30	0.48
EIGEN1	6.21	5.10
GRIM5C1	3.29	0.49
EGM96	3.74	1.50
JGM3	4.74	3.00
OSU91A	6.46	4.70
GRIM4C1	8.12	3.20

4.2.2. Trends in O-C residuals based on developments in gravity field modelling

In this study three (3) years of LAGEOS 1 and 2 tracking data spanning December 2005 to December 2008 were used to investigate the trend in the improvement of O-C residuals based on

a set of four gravity field models (i.e., EGM96, GRIM5C1, GGM03C and AIUB-GRACE01S) released between 1996 and 2008. The motivation for considering the selected models arises from the stable pattern (there was no noticeable improvement) in the O-C range residuals observed (see Figure 15) during the analysis of SLR data while using the models. In Table 12 the average SD values were calculated from the original O-C residuals (before filtering the outliers) of LAGEOS 1 and 2 considering the four gravity field models while, Table 13 presents slightly improved mean SD values of the O-C residuals after applying the 3σ-rule. Direct comparison of the average SD values computed from the four different models depicts that the GRIM5C1 and AIUB-GRACE01S have comparable accuracy (e.g., 3.35 and 3.36 based on LAGEOS 1 SLR and 3.35 and 3.34 cm based on LAGEOS 2 SLR data).

Table 12. Mean SD values calculated from the O-C residuals based on LAGEOS 1 and 2 data using EGM96, GRIM5C1, GGM03C and AIUB-GRACE01S models.

Model	Year	Mean SD [cm] LAGEOS 1	Mean SD [cm] LAGEOS 2
EGM96	1998	4.32	4.22
GRIM5C1	1999	3.94	3.84
GGM03C	2006	4.18	4.32
AIUB-GRACE01S	2008	3.92	3.82

Table 13. Mean SD values of the four models after 3σ-rule filtration.

LAGEOS 1		
Model	Mean SD [cm]	Residuals rejection %
EGM96	3.66	12.0
GRIM5C1	3.35	16.2
GGM03C	3.52	12.6
AIUB-GRACE01S	3.36	15.9
LAGEOS 2		
EGM96	3.60	10.0
GRIM5C1	3.35	9.5
GGM03C	3.84	11.4
AIUB-GRACE01S	3.34	9.3

As tabulated in Table 13 the O-C range residuals derived from LAGEOS 1 SLR data exhibit high residual rejection (~14% overall) during filtering, compared with ~10% rejected from O-C range residuals derived from the analysis of LAGEOS 2 SLR data sets. The EGM96 and GGM03C exhibits slightly higher O-C range residuals (3.7cm and 3.8cm respectively) based on

the analysis of LAGEOS 1 and 2 SLR data respectively. The high average SD based on the SLR analysis while considering the EGM96 and GGM03C gravity field models could be attributed to possible inherent biases in the O-C range residuals due to weak station geometry, systematic errors, poor tracking on certain days, especially during raining seasons and poor distribution of tracking data (due to network asymmetries).

4.3. Investigating possible improvements in the SDAS package

The SDAS package is still under development hence the estimates of O-C range residuals are expected to be optimized as more features are introduced into the software. The SDAS package has undergone considerable upgrades since the SLR data processing started back in 2008. This includes implementation of different IERS models to correct for the effects of tidal deformations due to solid Earth and pole tides. Hence the main focus in this section is to investigate the possible improvements in the estimation of O-C range residuals as realized by the general upgrade of SDAS. For this purpose we have analysed twenty-six months of LAGEOS 1 and 2 data spanning May 2008 to April 2010 while considering two recent gravity field models, EGM2008 (partly because this model has the highest degree/order 2159, though SDAS is only configured to process up to degree/order 20) and AIUB-GRACE01S (partly because this gravity field model exhibited the lowest O-C range residuals in the previous SLR data analysis).

The results for this analysis are presented in Table 14 (from the original O-C residuals) and Table 15 (after 3σ-rule filtration). The mean SD obtained in this study using a new version of the SDAS package shows an improvement by more than a half compared with the older version of the software. This suggests that the added features in the software have increased its capability to compute satellite orbits with unprecedented accuracy. In addition, the results reported in this study are comparable to those published in the literature. Generally, the SD values of other LAGEOS orbit computations, based on the most recent gravity field models, are found to be $\leq$1.5 cm, see for example Cheng *et al*. (2009). In this study we find the mean SD values for EGM2008 and AIUB-GRACE01S to be 1.8 cm based on LAGEOS 1 and 1.6 cm based on LAGEOS 2 data. This gives a difference of about 3 mm and 2 mm between our results and those reported by Cheng *et al*. (2009).

Table 14. Mean SD values calculated from the O-C residuals based on LAGEOS 1 and 2 data using EGM2008 and AIUB-GRACE01S models.

Model	Mean SD [cm] LAGEOS 1	Mean SD [cm] LAGEOS 2
EGM2008	2.01	1.77
AIUB-GRACE01S	2.00	1.80

Table 15. Mean SD values of the O-C residuals for LAGEOS 1 and 2 data based on EGM2008 and AIUB-GRACE01S models after 3σ-rule filtration.

LAGEOS 1		
Model	Mean SD [cm]	Residuals rejection %
EGM2008	1.81	3.90
AIUB-GRACE01S	1.84	3.10
LAGEOS 2		
EGM2008	1.64	3.30
AIUB-GRACE01S	1.62	3.20

4.4. Concluding remarks

Analysis of the accuracy of satellite orbits calculated from SLR measurements partly entails assessment of the influence of various gravity field models on the O-C range residuals. As a result, a more accurate gravity field model would manifest in the form of an improvement of the O-C range residuals calculated from the analysis of SLR data while considering the gravity model in question. In this study, the accuracy of twelve gravity field models released between 1990 and 2008 were analysed in terms of precise orbit determination by comparing their O-C range residuals. The results from a seven month data period indicated that there has been an improvement in the development of gravity field models over the period of evaluation. The evaluated models show an improvement by a factor of at least 2 since 1990 in terms of O-C range residuals. Furthermore, our analysis indicated that gravity field models released from 1999 onward are likely to be accurate at approximately the same level, at least to the sensitivity of our O-C tests, although there are many specific differences amongst these later models. A further analysis (for a period of three years) of a set of four gravity field models released between 1999 and 2008 demonstrates subtle differences in their O-C range residuals which could be associated with data quality. Overall, in the SLR data analysis (this includes the seven months and ~3 years of LAGEOS 1 and 2 SLR data) undertaken in this study, it was found that the satellite-only derived gravity field model AIUB-GRACE01S could be the most accurate due

to the low average SD of the corresponding O-C range residuals. The SDAS package has undergone numerous upgrades with promising results; current level of accuracy of the O-C range residuals is comparable to those published in the literature.

5. Analysis of the effect of tide parameterization on the accuracy of gravity field models

"Whether or not you can observe depends on the theory which you use. It is the theory which decides what can be observed" Albert Einstein.

5.1. Introduction

Gravity field models derived from SLR tracking data are utilized in various fields of research. For instance, they can be used to study the structure of the Earth, for computation of the geoid, reference systems, satellite orbits etc. The quality of the computed satellite orbits depends on the preferred gravity field model and its inherent accuracies. On the other hand, the accuracy of gravity field models is dependent on proper modelling of parameters that describe the disturbing forces acting on a satellite as it orbits the Earth. Factors such as availability, type and quality of data also play a significant role.

The main objective of this chapter is to investigate the contributions of Earth and pole tides on the O-C residuals across selected gravity field models by use of different configurations in the SDAS package. Contributions from the Earth and pole tides on the spherical harmonic coefficients (and also on O-C residuals) are computed using models incorporated into IERS 2010 conventions reported in Petit and Luzum (2010). In the SDAS package the Earth tide model is in the form of three selectable compatible models, these are selectable from the menu as IERS1, IERS2 and IERS3. In SDAS IERS1 corrects Earth tidal effects to degree 2 spherical harmonic coefficients, IERS2 is an extension of IERS1 with further corrections to the third and fourth spherical harmonic coefficients and IERS3 is a complete model which incorporates IERS1, IERS2 and frequency independent components of solid Earth tides.

In this study four SLR parameterization schemes were considered (i.e., the analysis options were configured as IERS1 off, IERS2 off, IERS3 off and pole tides off). The O-C results based on the four different tide parameterization schemes are first characterized by determining the inherent statistical structure. Here a direct comparison of the computed mean SD of the O-C residuals across the different models is used to determine an appropriate model that best describes the O-C data structure. In the second analysis a *t*-test statistical method was used (Student's *t*-test as applied in the *Statistica* statistical analysis package (Motulsky, 2003)) to assess the robustness of the mean SD of the O-C across different tide parameterization tests

based on the selected gravity field models. Overall, the results presented in this chapter have significant implications with regard to the interpretation of the O-C orbit errors computed from different gravity field models using each of the four tide parameterization test models.

5.2. Background

The gravitational attraction of the celestial bodies (e.g., Moon and Sun) exerts a direct force on Earth orbiting satellites. These forces also act on the rotating Earth thereby inducing deformations of the solid Earth. Such deformations tend to produce time variations in surface deflections and gravity with amplitudes up to 50 cm and 200 μGal respectively (Metivier and Conrad, 2008). The motion of the Earth (i.e. in orbit around the Sun and spinning around its instantaneous axis of rotation) and the coupled solar and lunar forces of attraction give rise to tidal deformations. Tidal deformations occur in the solid Earth, the ocean and in the atmosphere. Time varying deformations within the Earth system are consequences of solid Earth tides. On the other hand, pole tides are due to changes in the direction of the Earth's spin axis relative to a certain reference point in the Earth (McCarthy and Petit, 2003, Petit and Luzum 2010).

Generally, Earth and pole tides manifest as time-varying components of the gravity field. As a consequence, the Earth's gravitational field exhibits periodic variations which tend to affect the motion of satellites. Time variations in the global gravity field are often extracted from geodetic satellite data. They are commonly used to study a variety of geodynamic and atmospheric processes. In most geodetic applications, both the solid Earth and pole tides ought to be properly modelled so that their influence can be accounted for in geodetic observables. At present, the solid Earth tide components embedded in spherical harmonic coefficients (geopotential models) are accounted for by using classical models which have been incorporated into various IERS conventions and technical notes, the latest being IERS2010 reported by Petit and Luzum (2010).

5.2.1. Solid Earth tides

5.2.1.1. Effects of solid Earth tides on station coordinates

In SLR analysis the effects of Earth tide deformation are often noticed in the estimated time-varying component of station coordinates (here the greatest influence is in the vertical component of the station coordinates) see for example Figure 16.

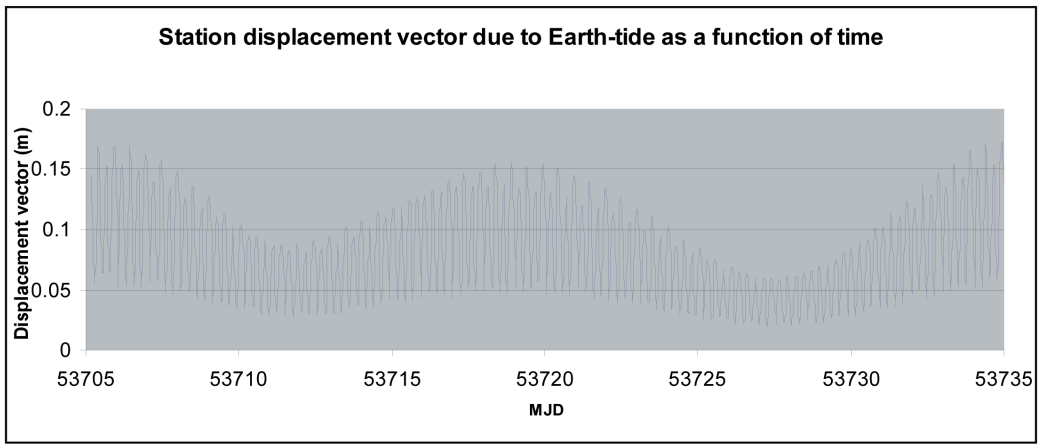

Figure 16. Position displacement of Yarragadee SLR tracking station due to Earth tides (Combrinck and Suberlak, 2007).

The effects of tidal deformations on the station coordinates due to Earth tides are often derived from Equation (71) as reported in Petit and Luzum (2010),

$$\Delta\vec{r} = \sum_{j=2}^{3} \frac{\left[GM_j r^4\right]}{\left[GM_\oplus R_j^{\,3}\right]} \left\{ \left[3l_2\left(\vec{R}_j \cdot \vec{r}\right)\right]\vec{R}_j + \left[3\left(\frac{h_2}{2} - l_2\right)\left(\vec{R}_j \cdot \vec{r}\right)^2 - \frac{h_2}{2}\right]\vec{r} \right\}, \qquad (71)$$

where GM_j and $GM_\oplus$ are the gravitational parameters for the Moon/Sun and the Earth respectively. Similarly, $\vec{R}_j, R_j$ and $\vec{r}, r$ are the unit vectors from the geocentre to the Moon or Sun and to the station respectively, together with the magnitudes of the vectors. In addition, h_2 and l_2 are the nominal second degree Love and Shida numbers respectively.

Tidal deformations are thought to manifest in the station height component since in most geodetic applications nearly all of the parameters in Equation (71) become time-independent at longer time-scales. As a result the time-dependent station height variation due to Earth tide deformations is accounted for by use of Equation (72) (Petit and Luzum, 2010),

$$\delta h_{STA} = \delta h_{K_1} H_{K_1} \left(-\sqrt{\frac{5}{24\pi}} 3 \sin\phi \cos\phi \sin\left(\theta_{K_1} + \lambda\right) \right). \tag{72}$$

In Equation (72) $\delta h_{K_1} = h_{K_1} - h_2$ (the estimated value is -0.0887), H_{K_1} is the amplitude of the K_1 term in the harmonic expansion of the tide generating potential and its value is 0.36878 m, ϕ and λ are the geocentric latitude and east longitude of the station and θ_{K_1} is the K_1 tide argument and is given by $\theta_g + \pi$. Equation (72) can be written in a simplified way as,

$$\delta h_{STA} = -0.0253 \sin\phi \cos\phi \left(\theta_g + \lambda\right). \tag{73}$$

Here the effect is a maximum at $\phi = 45^\circ$ where the amplitude is 0.013 m.

5.2.1.2. Effects of solid Earth tides on geopotential coefficients

The effects of solid Earth tides in the free space potential are often modelled as temporal variations in the standard geopotential coefficients C_{nm} and S_{nm}. Such contributions are often expressed in terms of Love number independence on tidal frequency (this includes long period terms) and station latitude. The effects of ellipticity and rotation of the Earth due to latitudinal dependence and the Coriolis force give rise to tidal deformations. As reported in Wahr (1981), tidal deformation effects require the use of three k- parameters (these are the Love and Shida numbers), k_{nm} and $k_{nm}^{(\pm)}$ (with the exception of $n = 2$) to characterize the changes produced in the free space potential by tides of spherical harmonic of degree and order (nm). In the case where mantle anelasticity is taken into account, anelasticity may introduce small imaginary parts to the k_{nm} and $k_{nm}^{(\pm)}$ terms that reflect a phase lag in the deformation response of the Earth to the tidal forces. In addition, anelasticity may also affect the Earth's deformational response to effects arising from direct action of the tide generating potential (e.g. ocean tides and wobbles of the mantle and the core regions).

The tidal contributions due to Earth tides are accounted for by a two-step formulation reported in Wahr (1981) and Petit and Luzum (2010). In the first step, frequency independent nominal Love numbers are used to evaluate the (nm, for $n = 2$ and $n = 3$ for all m) part of the tidal potential coefficients and compute the corresponding changes $\Delta\bar{C}_{nm}$ and $\Delta\bar{S}_{nm}$ (these are

temporal corrections to geopotential coefficients $\bar{C}_{nm}$ and $\bar{S}_{nm}$) in the time domain using the lunar and solar ephemeris. The induced contributions (i.e. ΔC_{nm} and ΔS_{nm}) due to the nm part of the tidal generating potential in the normalized geopotential coefficients having the same (nm) in the time domain are expressed in terms of the k_{nm} Love number using Equation (74) as reported in Petit and Luzum (2010),

$$\Delta\bar{C}_{nm} - i\Delta\bar{S}_{nm} = \frac{k_{nm}}{2n+1}\sum_{j=2}^{3}\frac{GM_j}{GM_\oplus}\left(\frac{R_e}{r_j}\right)^{n+1} P_{nm}\left(\sin\phi_j\right)e^{-im\lambda_j}. \qquad (74)$$

Here k_{nm} is the nominal Love number for degree n and order m, R_e is the equatorial radius of the Earth, $GM_\oplus$ and GM_j are gravitational parameters for the Earth and the Moon $(j=2)$ or Sun $(j=3)$ respectively, r_j is the distance from geocentre to Moon or Sun and ϕ_j and λ_j are the body-fixed geocentric latitude of the Moon or Sun and east longitude (from Greenwich) of the Sun or the Moon respectively. The contribution to the geopotential coefficients in the degree 4, C_{4m} and S_{nm} due to degree 4 tides are also computed in a similar method in terms of $k_{2m}^{(+)}$ as given in Equation (75),

$$\Delta\bar{C}_{4m} - i\Delta\bar{S}_{4m} = \frac{k_{2m}^{(+)}}{5}\sum_{j=2}^{3}\frac{GM_j}{GM_\oplus}\left(\frac{R_e}{r_j}\right)^{3} P_{2m}\left(\sin\phi_j\right)e^{-im\lambda_j}, \quad (m=0,1,2). \qquad (75)$$

The parameter values utilized in the computation of step 1 are given in Table 16. The nominal value for $m=0$ needs to be selected as a real since the contribution to $\bar{C}_{20}$ from the imaginary part of $k_{20}^{(0)}$.

Table 16. Nominal values of solid Earth tide external potential Love numbers.

Elastic Earth				
n	m	k_{nm}	$k_{nm}^{(+)}$	$R_e k_{nm}$
2	0	0.29525	-0.00087	0.30190
2	1	0.29470	-0.00079	0.29830
2	2	0.29801	0.00057	0.30102
3	0	0.093		
3	1	0.093		
3	2	0.093		
3	3	0.094		

The second step corrects arguments of a harmonic expansion of the tide generating potential for which the error due to the Love number k_2 of step 1 is above a certain cut-off value. In this step the frequency dependent values considered are obtained from Mathews *et al.* (1995) and corrections to $\Delta\bar{C}_{nm}$ and $\Delta\bar{S}_{nm}$ values are from step 1. These corrections are the sum of contributions from a number of tidal constituents belonging to the respective bands. The contribution to $\Delta\bar{C}_{20}$ from the long period tidal constituents of various frequencies, f is given by Equation (76) as reported in Petit and Luzum (2010),

$$R_e \sum_{f(2,0)} \left(A_0 \delta k_f H_f \right) e^{i\theta f} = \sum_{f(2,0)} \left[\left(A_0 H_f \delta k_f^R \right) \cos\theta_f - \left(A_0 H_f \delta k_f^I \right) \sin\theta_f \right]. \quad (76)$$

Furthermore, the contributions to $\left(\Delta\bar{C}_{21} - i\Delta\bar{S}_{21}\right)$ due to the diurnal tidal constituents and to $\left(\Delta\bar{C}_{22} - i\Delta\bar{S}_{22}\right)$ from the semidiurnal band are given by,

$$\Delta\bar{C}_{2m} - i\Delta\bar{S}_{2m} = \eta m \sum_{f(2,m)} \left(A_m \delta k_f H_f \right) e^{i\theta_f}, \qquad (m = 1,2), \qquad (77)$$

where

$$A_0 = \frac{1}{R_e\sqrt{4\pi}} = 4.4228\times10^{-8}\ \mathrm{m}^{-1},$$

$$A_m = \frac{(-1)^m}{R_e\sqrt{8\pi}} = (-1)^m \left(3.1274\times10^{-8}\right)\ \mathrm{m}^{-1}, \qquad (m \neq 0), \qquad (78)$$

$$\eta_1 = -i, \qquad \eta_2 = 1.$$

Here δk_f gives the difference between k_f defined as k_{2m}^0 at frequency f and the nominal value k_{2m}, in the sense $k_f - k_{2m}$ plus a contribution from ocean loading; δk_f^R is the real part of δk_f; δk_f^I is the imaginary part of δk_f; H_f is the amplitude of the term at frequency f from the harmonic expansion of the tide generating potential defined according to the convention of Cartwright and Taylor (1971). In Equation (76),

$$\theta_f = \vec{n}\beta = \sum_{i=1}^{6} n_i \beta_i, \text{ or } \quad \theta_f = m\left(\theta_g + \pi\right) - \vec{N}\vec{F} = m\left(\theta_g + \pi\right) - \sum_{j=1}^{5} N_j F_j.$$

In addition, $\vec{\beta}$ is the six-vector of Doodson's fundamental arguments β_i, (τ, s, h, p, N', p_s), $\vec{n}$ is the six-vector of multipliers n_i of the fundamental arguments, $\vec{F}$ is the five-vector of

fundamental arguments F_j (the Delaunay variables l, l', F, D, Ω) of nutation theory, $\vec{N}$ is the five-vector of multipliers N_j of the Delaunay variables for the nutation of frequency $-f + d\theta_g / dt$ and θ_g is the Greenwich Mean Sidereal Time.

5.2.2. Pole tides

The pole tides cause spatial variations in the gravitational potential due to Earth rotation. These tides are caused by changes in the direction of the Earth's spin axis relative to a point fixed in the Earth. The spin produces a centrifugal force, which depends on the angular distance between the spin axis and a reference point. As the spin axis moves, this distance and the centrifugal force changes. The pole tide deformation effects on the station coordinates (up to ~cm) arises from the first order perturbation associated with the centrifugal potential caused by the Earth's rotation. Rotational deformations due to polar motion can be modelled by assuming that the perturbation in the centrifugal potential is related to the Earth's rotation. Thus considering (x, y, z) as the terrestrial system of reference, a first order perturbation of the centrifugal potential (ΔV) can be expressed in Equation (79), as reported in Petit and Luzum (2010),

$$V = -\frac{1}{2}\left[r^2 \left|\vec{\Omega}\right|^2 - \left(\vec{r}.\vec{\Omega}\right)^2 \right], \tag{79}$$

where $\vec{\Omega} = \Omega\left(m_1 \hat{x} + m_2 \hat{y} + \left(1 + m_3\right)\hat{z}\right)$, Ω is the mean angular velocity of rotation of the Earth, m_1 and m_2 are small dimensionless parameters describing the time dependent offset of the instantaneous rotation pole from the mean, m_3 is the fractional variation in the rotational rate, r is the geocentric distance to the station. Neglecting the m_3 term, due to its small influence, the first order perturbation in the potential (ΔV) can be written in terms of m_1 and m_2 as in Equation (80) (Petit and Luzum, 2010),

$$\Delta V\left(r, \theta, \lambda\right) = -\left(\frac{\Omega^2 r^2}{2}\right)\sin 2\theta\left(m_1 \cos\lambda + m_2 \sin\lambda\right). \tag{80}$$

The tidal Love numbers and ΔV can be used to compute the radial (S_r, positive upwards) and horizontal displacements S_θ and S_λ (positive southwards and eastwards respectively) due to ΔV as given in Equation (81),

$$S_r = h_2 \frac{\Delta V}{g}, \quad S_\theta = \frac{l_2}{g} \partial_\theta \Delta V, \quad S_\lambda = \frac{l_2}{g} \frac{1}{\sin\theta} \partial_\lambda \Delta V. \tag{81}$$

The coordinates (in the ITRF) of the position of the Earth's mean rotation pole due to secular variations are given in terms of the polar motion variables (x_p, y_p) and are obtained by running averages $\bar{x}_p$ and $-\bar{y}_p$, thus

$$m_1 = x_p - \bar{x}_p, \qquad m_2 = -(y_p - \bar{y}_p). \tag{82}$$

In order to achieve the most accurate results for the polar motion variables estimates of the mean pole are commonly utilised. Now-a-days the conventional mean pole of the IERS conventions (2003) is replaced with the IERS conventional mean pole incorporated in the IERS conventions (2010). The latest version of the IERS conventional mean pole is composed of a cubic model validated over the period from 1976.0 to 2010.0 and a linear model for extrapolation after 2010.0. Generally, the IERS (2010) mean pole model can be described as per Equation (83)

$$\bar{x}_p(t) = \sum_{i=0}^{3} (t - t_0)^i \times \bar{x}_p^i \qquad \bar{y}_p(t) = \sum_{i=0}^{3} (t - t_0)^i \times \bar{y}_p^i, \tag{83}$$

where t_0 is 2000 and the coefficients of $\bar{x}_p^i$ and $\bar{y}_p^i$ are given in Table 17.

Table 17. Coefficients of the IERS (2010) mean pole model.

Degree i	Until 2010.0		After 2010.0	
	$\bar{x}_p^i$ / mas yr^{-i}	$\bar{y}_p^i$ / mas yr^{-i}	$\bar{x}_p^i$ / mas yr^{-i}	$\bar{y}_p^i$ / mas yr^{-i}
0	55.974	346.346	23.513	358.891
1	1.8243	1.7896	7.6141	-0.6287
2	0.18413	-0.10729	0.0	0.0
3	0.007024	-0.000908	0.0	0.0

The radial and horizontal displacements S_r, S_θ and S_λ, can be computed by use of Love number values appropriate to the frequency of the pole tides $(h = 0.6027,\ l = 0.0836)$ and $r = a = 6.378 \times 10^6$ m as follows:

$$\begin{aligned} S_r &= -32 \sin 2\theta (m_1 \cos\lambda + m_2 \sin\lambda) \text{ mm}, \\ S_\theta &= -9 \cos 2\theta (m_1 \cos\lambda + m_2 \sin\lambda) \text{ mm}, \\ S_\lambda &= 9 \cos 2\theta (m_1 \sin\lambda - m_2 \cos\lambda) \text{ mm}, \end{aligned} \tag{84}$$

with m_1 and m_2 given in arcseconds. The effects of polar motion in the Cartesian coordinate systems as reported in IERS2010 conventions (Petit and Luzum, 2010) are represented in Equation (85),

$$\left[dX, dY, dZ\right]^T = R^T \left[S_\theta, S_\lambda, S_r\right]^T, \tag{85}$$

where

$$R = \begin{pmatrix} \cos\theta\cos\lambda & \cos\theta\sin\lambda & -\sin\theta \\ -\sin\lambda & \cos\lambda & 0 \\ \sin\theta\cos\lambda & \sin\theta\sin\lambda & \cos\theta \end{pmatrix}. \tag{86}$$

In order to show the effects of pole tides to the accuracy of gravity field models Equation (80) can be expressed as Equation (87)

$$\Delta V\left(r,\theta,\lambda\right) = -\frac{\Omega^2 r^2}{2}\sin 2\theta R_e\left[\left(m_1 - im_2\right)e^{i\lambda}\right]. \tag{87}$$

The deformation caused by the pole tide produces time-dependent perturbations in the external potential given by Equation (88)

$$\Delta V = -\frac{\Omega^2 r^2}{2}\sin 2\theta R_e\left[k_2\left(m_1 - im_2\right)e^{i\lambda}\right]. \tag{88}$$

These perturbations are related to changes in the geopotential coefficients C_{21} and S_{21}, which describe the position of the Earth's figure axis. Using the value $0.3077 + 0.0036i$ for the Love number k_2 the time-dependent perturbations in the C_{21} and S_{21} geopotential coefficients can be estimated as follows

$$\begin{aligned} \Delta\bar{C}_{21} &= -1.333\times10^{-9}\left(m_1 - 0.0115m_2\right), \\ \Delta\bar{S}_{21} &= -1.333\times10^{-9}\left(m_1 - 0.0115m_2\right), \end{aligned} \tag{89}$$

where m_1 and m_2 given in arcseconds.

5.3. Parameterization

The latest SDAS version (Combrinck personal communication, July 2012) utilises IERS2010 conventions to correct for Earth and pole tide effects. In the software the Earth tide model is divided into three compatible and selectable models namely, IERS1, IERS2 and IERS3 (these are described in Table 18). The objective of the work presented in this chapter is to perform orbital tests with particular emphasis on evaluating the influence of using IERS1, IERS2 and

IERS3 compatible Earth tide models (affecting the static GGM spherical harmonic coefficients) and pole tide model (IERS2010 standard) in the determination of satellite orbits by analysing LAGEOS data using different gravity field models. The IERS1 model in SDAS is considered the least complex Earth tide model and corrects degree 2 spherical harmonics of a given geopotential model. On the other hand, IERS2 in the analysis software is an extension of IERS1 with additional corrections to third and fourth degree spherical harmonics. Lastly, a complete model of Earth tides, the IERS3 is considered as the most complex model since it includes both IERS1 and IERS2 plus it takes into account the frequency independent components of the solid Earth tides. A summary of these compatible models and their respective corrections to spherical harmonic coefficients is given in Table 18.

Table 18. Summary of the compatible models derived from IERS2010 with their respective corrections to spherical harmonic coefficients of a geopotential model.

Compatible models from IERS2010	Corrections to a typical geopotential model
IERS1	$C_{20}, C_{21}, C_{22}, S_{21}, S_{22}$
IERS2	IERS1 + $C_{30}, C_{31}, C_{32}, C_{33}, S_{31}, S_{32}, S_{33}$ + $C_{40}, C_{41}, C_{42}, S_{41}, S_{42}$
IERS3	IERS1 + IERS2 + frequency independent components
Pole tides	C_{21}, S_{21}

The methodology followed can be formulated as follows: suppose that a GGM is represented by $y = \eta(x)$, where x represents a vector of input empirical models to be varied and y is the expected output; for the purpose of this study y is considered as the O-C residuals. Let η be a GGM such that the way the model responds to changes in each of the three elected empirical models is not transparent. The purpose of selecting different empirical model combinations during the analysis of SLR data is to investigate how changes in the geopotential coefficients (GGM dependent) in the context of O-C residuals, y, are related to or affected by Earth (as modelled by IERS1, IERS2 and IERS3) and pole tides (modelled using IERS2010 standard) contributions.

Table 19 summarises the criteria used to test the effects of the IERS1, IERS2, IERS3 and pole tides on the O-C residuals across five different gravity field models when determining LAGEOS orbits as analysed with SDAS. In particular, the "on/disabled" configuration tests were conducted for each considered model by disabling one of the compatible models while the

other two are enabled during processing. Basically four tests were conducted for each selected gravity field model based on LAGEOS 1 and 2 data. In the first test the IERS1 Earth tide model and pole tides (IERS2010 standard) were activated while disabling IERS2 and IERS3 in the software. The second test involved the activation of IERS2 and pole tides while IERS3 was disabled in the software to investigate their combined effects on the derived O-C residuals across the selected models. In third test the IERS3 and pole tides were implemented and lastly, in the fourth test the IERS3 was activated and pole tides were disabled during LAGEOS 1 and 2 data processing.

Table 19. Orbital parameter tests strategy used. Parameters were tested at 0.8σ rejection.

Orbital tests	Parameter configuration	
Test 1	IERS1 and pole tides 'on'	IERS2 and IERS3 'disabled'
Test 2	IERS2 and pole tides 'on'	IERS3 'disabled'
Test 3	IERS3 and pole tides 'on'	IERS1 and IERS2 'enabled'
Test 4	IERS3 'on'	Pole tides 'disabled'

5.4. Models Evaluated

In this study five gravity field models were used in SDAS analysis of LAGEOS 1 and 2 SLR data. These models are the GRIM5C1, EIGEN-CG30C, AIUB-CHAMP01S, EGM2008 and AIUB-GRACE01S and they were evaluated using LAGEOS 1 and 2 data sets spanning January to June 2009. Specific characteristics and references of the selected models are summarized in Table 20. The ILRS tracking stations selected for data processing are the so-called EOP SLR stations. These stations are believed to be providing high quality SLR data for the computation of EOPs. The EOP selected stations include Yarragadee, McDonald, Zimmerwald, Wettzell, Monument Peak, Hartebeesthoek, Herstmonceux, Greenbelt, Riyadh, Graz, Mount-Stromlo, Beijing and Arequipa.

Table 20. Geopotential models evaluated.

Model	Year	Degree/order	Data	Reference
GRIM5C1	1999	120	S, G, A	Gruber *et al.* (2000)
EIGEN-CG03C	2005	360	S(CHAMP,GRACE),G,A	Foerste *et al.* (2005)
AIUB-CHAMP01S	2007	90	S(CHAMP)	Prange *et al.* (2007)
EGM2008	2008	2190	S(GRACE),G,A	Pavlis *et al.* (2008)
AIUB-GRACE01S	2008	120	S(GRACE)	Jaeggi *et al.* (2008)

The SLR data in this study were processed using constants and reference frames listed in Table 21.

Table 21. Constants and reference frames utilised during LAGEOS 1 and 2 data processing.

Reference frame epoch	SLRF2005
Inertial reference frame	J2000
Pole-tide correction (station position)	IERS2010
Correction for general relativistic effects	IERS2010
Earth–tide correction (station position)	Petrov 2005
Ocean loading correction (station position)	Agnew/Scherneck
Atmospheric loading	Disabled
Earth orientation	a-priori Earth orientation parameters and UTC-UT1 values as per IERS extrapolated to observation epoch
O-C outlier rejection	Selectable: set to 0.8 sigma
Average pole	IERS2010

5.5. Statistical analysis of O-C residuals

Table 22 and Table 23 present the results for the statistical orbital fits of LAGEOS 1 and 2 based on IERS1, IERS2, IERS3 and pole tide tests using the GRIM5C1, EIGEN-CG03C, AIUB-CHAMP01S, EGM2008 and AIUB-GRACE01S gravity field models. The listed statistical results considered in the tables are the mean SD of the O-C residuals for each orbital test. These SD values are used as a measure of orbit quality as well as gravity model accuracy. There are small differences in the calculated average SDs across the five elected gravity field models. This suggests that the choice of parameterizations has a particular influence on satellite orbit determination as well as gravity field model accuracy. The results presented in Table 22 and Table 23 indicate that from the SLR analysis utilizing the selected gravity field models, the average SDs of the O-C residuals are about 2 cm and 1 cm for LAGEOS 1 and 2 respectively.

The following five GGM model comparisons utilised LAGEOS 1 data.

GRIM5C1:

In Table 22 the GRIM5C1 gravity field model gives a slightly improved solution when the Earth tides are modelled using the complex Earth tide model, IERS3, with the pole tides disabled

during data processing followed by a combined implementation of the IERS3 model and pole tides. A combination of the IERS2 model and pole tides decreases the quality of the GRIM5C1 gravity field model. The poorest O-C SD solution is obtained when the least complex Earth tide model IERS1 and pole tides are jointly implemented in the software. This indicates that the accuracy of the final solution when using the GRIM5C1 model and LAGEOS 1 data can be achieved through inclusion of spherical harmonic components due to Earth tides (added) to those of the GRIM5C1 model. The pole tides seem to contribute less towards the precision of the final solution of GRIM5C1.

EIGEN-CG03C:

The combined gravity field model, EIGEN-CG03C gives the best solution for the combined selection of IERS3 and pole tides followed by a combination of IERS2 and pole tides. The O-C SD solution worsens when IERS3 is activated and pole tides disabled in SDAS. Its worst solution is when IERS1 and pole tides are jointly selected during data processing. Based on this result the Earth and pole tides equally contribute towards the quality of the EIGEN-CG03C gravity field model. Hence it is necessary to include both the spherical harmonic coefficient components due to the Earth and pole tides when using EIGEN-CG03C and LAGEOS 1 data.

AIUB-CHAMP01S:

The CHAMP satellite-only model, AIUB-CHAMP01S results in a better solution when IERS3 and pole tides are jointly active in the software followed by when the IERS3 model is active and pole tides disabled. The solution worsens when IERS2 and pole tides are jointly selected and the poorest solution is obtained when the least complex Earth tide model, IERS1 and pole tides are jointly selected. In conjunction with the EIGEN-CG03C gravity field, the usage of AIUB-CHAMP01S with LAGEOS 1 data requires the inclusion of both the spherical harmonic coefficient components due to Earth and pole tides.

EGM2008:

For the EGM2008 gravity field model the best solution is obtained when IERS2 and pole tides are active, followed by the combination of IERS3 and pole tides. The average SD of the O-C residuals reduces when the IERS1 model and pole tides are active during data processing. Its

poorest solution is obtained when the IERS3 model is active and the pole tides disabled in SDAS. The results indicate that both the spherical harmonic coefficient components due to Earth and pole tides play a significant (interacting) role in the final solution of the EGM2008 gravity field model when LAGEOS 1 data is utilised.

AIUB-GRACE01S:

Lastly using LAGEOS 1, the GRACE satellite-only model AIUB-GRACE01S, exhibits the best solution when the IERS3 model is activated and pole tides are disabled in the software followed by a combined implementation of IERS3 and pole tides. The O-C SD solution worsens when IERS2 and pole tides are implemented during data processing. The worst solution is obtained when the least complex Earth tide model, IERS1 and pole tides are implemented in SDAS. This suggests that optimal use of the quality of AIUB-GRACE01S occurs when using LAGEOS 1 data through a proper and a complete modelling of contributions from Earth tides only. The differences between IERS1, IERS2 and IERS3 O-C values are statistical only, as the differences are non-significant (at the level of fractions of mm).

Table 22. Results of the mean SD of the O-C extracted from LAGEOS 1 data.

Model	Mean SD [cm] when IERS1 and pole tides are 'on'	Mean SD [cm] when IERS2 and pole tides are 'on'	Mean SD [cm] when IERS3 and pole tides are 'on'	Mean SD [cm] when IERS3 is 'on' & pole tides are disabled
GRIM5C1	2.184	2.151	2.131	2.129
EIGEN-CG03C	2.308	2.266	2.246	2.279
AIUB-CHAMP01S	2.187	2.135	2.116	2.126
EGM2008	2.202	2.160	2.169	2.165
AIUB-GRACE01S	2.174	2.145	2.141	2.133

Figure 17 depicts SD values averaged across the selected (five) gravity field models for individual tide parameterization test. As depicted in Figure 17 the IERS1 and pole tides test exhibits the highest mean SD solution while the mean SD of the O-C improves for the three remaining parameterization tests with only parts-per millimetre differences. In particular, the IERS3 and pole tide parameterization test have the lowest solution. This is expected since most

of the gravity field models yield a best mean SD solution when IERS3 and pole tides are activated during the LAGEOS 1 data processing.

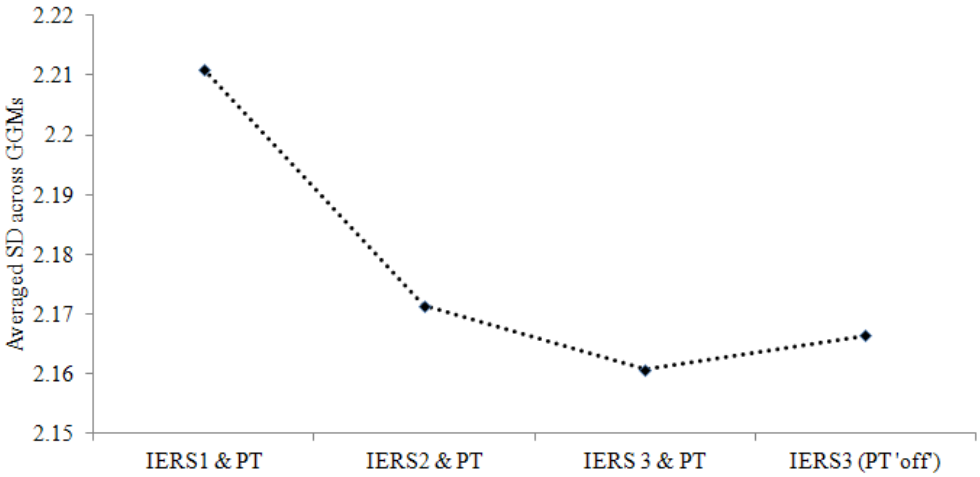

Figure 17. Averaged SD across the GRIM5C1, EIGEN-CG03C, AIUB-CHAMP01S, EGM2008 and AIUB-GRACE01S gravity field models based on LAGEOS 1 data.

The following five GGM model comparisons utilised LAGEOS 2 data.

GRIM5C1:

The GRIM5C1 gravity field model has the lowest O-C SD solution when LAGEOS 2 data are processed with IERS3 and pole tides activated followed by active combination of IERS2 and pole tides in SDAS. The solution worsens when the IERS3 model is active and the pole tides are disabled during data processing. The poorest O-C SD solution is obtained when the least complex Earth tide model, IERS1 and pole tides are jointly activated in the software. Similar to the results obtained for LAGEOS 1, the optimal use of the quality of GRIM5C1 when using LAGEOS 2 occurs when all spherical harmonic functions due to the Earth and pole tides are included to those of the gravity field model. The different O-C SD values obtained for LAGEOS 1 where pole tide was either on or off, combined with IERS3 are statistically insignificant. Therefore one would want to utilise IERS3 and pole tides for both LAGEOS 1 and LAGEOS 2 when using GRIM5C1.

EIGEN-CG03C:

The combined gravity field model, EIGEN-CG03C exhibits the best O-C SD solution when the IERS3 model is active with pole tides disabled followed by the active combination of IERS2 and pole tides in the software. The solution worsens with the joint combination of IERS1 and pole tides and the poorest solution is obtained when IERS3 and pole tides are jointly selected during LAGEOS 2 data processing. This result is different from the previous EIGEN-CG03C using LAGEOS 1 data. It is apparent that adding the spherical harmonic coefficients to those of the GGM due to pole tide in combination with the IERS3 Earth tide coefficients reduces the quality of the solution.

AIUB-CHAMP01S:

The CHAMP satellite-only model has the best solution when IERS3 and pole tides are active in SDAS followed by the implementation of IERS3 with pole tides disabled. A combination of IERS2 and pole tides reduces the quality of the O-C SD solution. The solution worsens further when the least complex Earth tide model, IERS1 and pole tides are jointly combined in the software. This is similar result obtained with AIUB-CHAMP01S using LAGEOS 1 data implying that there are no satellite dependence effects. Considering the similarities in the results from the two satellites it can be concluded that the full spherical harmonic coefficient components due to the Earth and pole tides need to be taken into account when using AIUB-CHAMP01S and LAGEOS 2.

EGM2008:

The EGM2008 gravity field model exhibits the lowest O-C SD solution when IERS3 and pole tides are selected, followed by the active combination of IERS2 and pole tides during LAGEOS 2 data analysis. Activation of the complex Earth tide model, IERS3 with the pole tides disabled worsens the O-C SD solution. The poorest solution is obtained when the IERS1 model and pole tides are jointly selected in the software. Considering the results obtained with LAGEOS 1 data, this indicates the necessity of including the full spherical harmonic coefficient components due to pole tides when using EGM2008 and LAGEOS 1 and 2 data. In both cases (LAGEOS 1 and LAGEOS 2) results are improved when including pole tides.

AIUB-GRACE01S:

The GRACE satellite-only model, AIUB-GRACE01S gives the best solution when contributions from the Earth tides are modelled with IERS 3 while the pole tides are disabled, followed by the active combination of IERS2 and pole tides in the software. A joint implementation of the complex Earth tide mode with pole tides reduces the O-C SD solution. The solution worsens further with active combination of the least complex Earth tide model, IERS1 and pole tides. Considering the quality of AIUB-GRACE01S it is necessary to include spherical harmonic coefficient components due Earth tides when using LAGEOS 2 data. It is also apparent that the inclusion of spherical harmonic coefficient components due pole tides tends to reduce the quality of the AIUB-GRACE01S gravity field model although this is at such a low level to be statistically insignificant.

Table 23. Results of the mean SD extracted from LAGEOS 2 data for different tide parameterization options.

Model	Mean SD [cm] when IERS1 and pole tides are 'on'	Mean SD [cm] when IERS2 and pole tides are 'on'	Mean SD [cm] when IERS3 and pole tides are 'on'	Mean SD [cm] when IERS3 is 'on' and pole tides are disabled
GRIM5C1	1.490	1.467	1.463	1.486
EIGEN-CG03C	1.711	1.634	1.828	1.633
AIUB-CHAMP01S	1.515	1.500	1.490	1.498
EGM2008	1.524	1.497	1.483	1.510
AIUB-GRACE01S	1.527	1.481	1.495	1.469

The trend of the averaged SD of the O-C residuals for the four parameterization tests across all the considered gravity field models based on LAGEOS 2 data is illustrated in Figure 18. Highest averaged mean SD solutions are obtained for IERS1 and pole tides, and IERS3 and pole tides parameterization tests. The results obtained for the IERS3 and pole tides test contradicts those obtained when LAGEOS 1 SLR data is utilized (here IERS3 and pole tides gave the best mean SD solution). This difference arises from the large mean SD of the O-C residuals obtained when using the EIGEN-CG03C gravity field model while processing SLR LAGEOS 2 data. Generally the IERS3 and pole tides parameterization with the EIGEN-CG03C gravity field model based on the analysis of LAGEOS 2 SLR data yields O-C residuals which are almost twice as large as

compared with those obtained from the other parameterization test for the similar model and data. This uniqueness could be attributed to systematic errors in the adjustment procedure during data processing. It is apparent that the pole tides have a significant influence on the final O-C residual, considering the IERS3 Earth tide model and the EIGEN-CG03C gravity field model. If the average O-C value of the EIGEN-CG03C model is excluded, the plot in Figure 18 would be similar to that of Figure 17, with the least detailed model exhibiting the largest O-C values and the most detailed model (IERS3 plus pole tide) providing the best solutions as depicted in Figure 19. This example indicates that some GGM models may produce unexpected results.

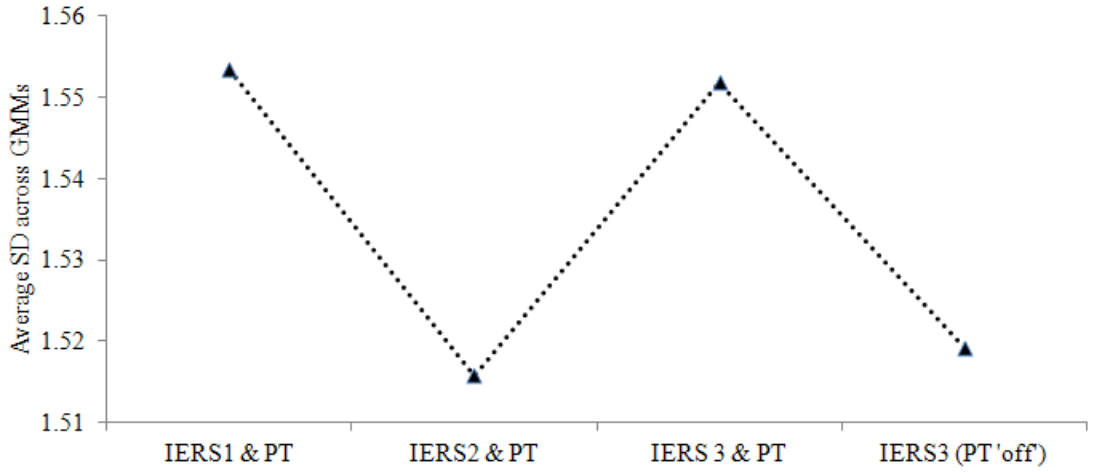

Figure 18. Averaged SD across GRIM5C1, EIGEN-CG03C, AIUB-CHAMP01S, EGM2008 and AIUB-GRACE01S gravity field models based on LAGEOS 2 data.

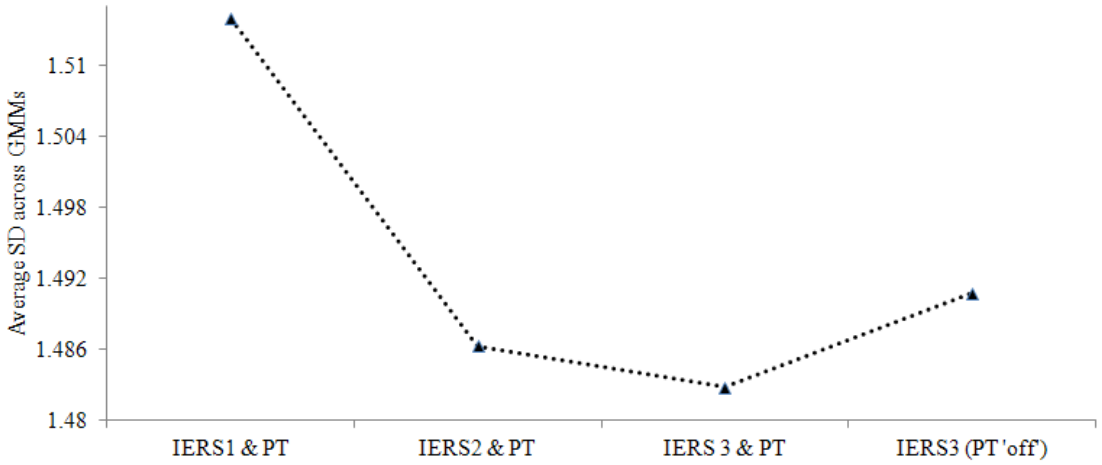

Figure 19. Averaged SD across GGMs with EIGEN-CG03C model excluded.

5.6. Statistical significance of the variations in the standard deviation of O-C residuals between models

The mean SD of the O-C residuals presented in Table 22 and Table 23 as derived from LAGEOS 1 and 2 data using GRIM5C1, EIGEN-CG03C, AIUB-CHAMP01S, EGM2008 and AIUB-GRACE01S gravity field models exhibit subtle differences across the different tide parameterization. This makes it difficult to ascertain whether the difference in the mean SD values has any statistical significance for the different gravity field models. In this section a *t*-test was performed to assess whether the mean SD differences between the tide parameterization options are statistically different from each other. In particular the mean SD of two groups of tide parameterization tests is compared to investigate whether the means are statistically significant.

The *t*-test (Welch's t-test) used in the present study was computed as a ratio of the difference between the two averages and the measure of O-C residual variances corresponding to the different parameterization options. If the parameter options are i and j then the student's t-test can be calculated as per Equation

$$t_{ij/ji} = \frac{\bar{X}_i - \bar{X}_j}{\sqrt{\frac{S_i^2}{N_i} - \frac{S_j^2}{N_j}}}, \qquad \forall\ i \neq j \tag{90}$$

where $\bar{X}_i$ and $\bar{X}_j$ are the means of the i and j O-C residuals, S_i^2 and S_j^2 are the pooled O-C residual variances, N_i and N_j are the data sizes for test i and test j and $t_{ij/ji}$ is the test statistic evaluated as a Student t quantile with $N_i + N_j - 2$ degrees of freedom. In this study a risk or significant level given by $\alpha = 0.05$ is used to test for significance between two considered groups. For example if a typical *t*-test gives a *p*-value less than or equal to 0.05 $(p \leq 0.05)$ then the mean SD difference between the two is deemed statistically significant else it is statistically insignificant. The results for the *t*-tests performed using the O-C residuals derived from the four tide parameterization tests using the GRIM5C1 gravity field model during the analysis of SLR data derived from LAGEOS 1 observations are summarised in Table 24 (differences are in metres). Here the variables considered correspond to the orbital tests summarised in Table 19, that is, Var 1: IERS1 and pole tides; Var 2: IERS2 and pole tides; Var 3: IERS3 and pole tides

and Var 4 corresponds to the IERS3 test with the pole tides disabled. In Table 24 the *t*-test computed between Var 1 and Var 2, Var 1 and Var 3, Var 1 and Var 4, Var 3 and Var 4 have *p*-values that are greater than the 0.05 (or 5%) significance level implying that the differences in the mean SD (listed in column 2) are not statistically significant. In contrast the computed *t*-values for Var 2 versus Var 3 and Var 2 versus Var 4 correspond to *p*-values which are less than 0.05 implying that the difference in the mean SD between the considered group tests for GRIM5C1 are statistically significant.

Table 24. The *t*-test results for GRIM5C1 based on LAGEOS 1 data.

Variable	Diff (mean SD)	Diff. (SD)	t-value	p-value
Var 1 vs. Var 2	0.000330	0.005756	0.75404	0.451857
Var 1 vs. Var 3	0.000537	0.005795	1.21940	0.224362
Var 1 vs. Var 4	0.000550	0.005774	1.25360	0.211690
Var 2 vs. Var 3	0.000207	0.001279	2.13114	0.034498
Var 2 vs. Var 4	0.000220	0.001466	1.97644	0.049704
Var 3 vs. Var 4	0.000013	0.001652	0.10385	0.917410

Table 25 (difference values are in metres) summarises the *t*-test results for EIGEN-CG03C using LAGEOS 1 data. Considering the *p*-values calculated in each of the tests it is apparent that the mean SD differences between the considered group tests are statistically insignificant. The negative *t*-test value implies that the first mean was smaller than the second mean for the considered groups. Similar results are obtained for the three remaining gravity field models (AIUB-CHAMP01S, EGM2008 and AIUB-GRACE01S) though the p-values are relatively low, see Table 26, Table 27 and Table 28.

Table 25. The *t*-test results for EIGEN-CG03C based on LAGEOS 1 data.

Variable	Diff (mean SD)	Diff. (SD)	*t*-value	*p*-value
Var 1 vs. Var 2	0.000421	0.010541	0.51030	0.610537
Var 1 vs. Var 3	0.000617	0.010592	0.74423	0.457818
Var 1 vs. Var 4	0.000294	0.010954	0.34250	0.732420
Var 2 vs. Var 3	0.000196	0.002346	1.06703	0.287547
Var 2 vs. Var 4	-0.000127	0.002695	-0.60382	0.546807
Var 3 vs. Var 4	-0.000324	0.002621	-1.57596	0.116985

Table 26. The *t*-test results for AIUB-CHAMP01S based on LAGEOS 1 data.

Variable	Diff (mean SD)	Diff. (SD)	*t*-value	*p*-value
Var 1 vs. Var 2	0.000514	0.005443	1.24209	0.215896
Var 1 vs. Var 3	0.000705	0.005664	1.63682	0.103497
Var 1 vs. Var 4	0.000611	0.005695	1.41097	0.160061
Var 2 vs. Var 3	0.000191	0.001520	1.65192	0.100375
Var 2 vs. Var 4	0.000097	0.001472	0.86594	0.387728
Var 3 vs. Var 4	-0.000094	0.001930	-0.64046	0.522728

Table 27. The *t*-test results for EGM2008 based on LAGEOS 1 data.

Variable	Diff (mean SD)	Diff. (SD)	*t*-value	*p*-value
Var 1 vs. Var 2	0.000420	0.006054	0.911976	0.363058
Var 1 vs. Var 3	0.000322	0.006073	0.697232	0.486599
Var 1 vs. Var 4	0.000368	0.006332	0.763458	0.446236
Var 2 vs. Var 3	-0.000098	0.001810	-0.710726	0.478217
Var 2 vs. Var 4	-0.000052	0.001433	-0.479173	0.632424
Var 3 vs. Var 4	0.000046	0.001909	0.314152	0.753786

Table 28. The *t*-test results for AIUB-GRACE01S based on LAGEOS 1.

Variable	Diff (mean SD)	Diff. (SD)	*t*-value	*p*-value
Var 1 vs. Var 2	0.000289	0.002903	1.30929	0.192183
Var 1 vs. Var 3	0.000326	0.002355	1.81808	0.070791
Var 1 vs. Var 4	0.000409	0.003055	1.75956	0.080260
Var 2 vs. Var 3	0.000036	0.002757	0.17405	0.862027
Var 2 vs. Var 4	0.000120	0.001508	1.04348	0.298192
Var 3 vs. Var 4	0.000083	0.002864	0.38196	0.702960

The *t*-test results for the GRIM5C1 gravity field model using LAGEOS 2 data are given in Table 29. The computed *t*-values for all the six pairs give *p*-values are greater than the 0.05 risk level. It is therefore concluded that the computed mean SD differences between these six group tests are not statistically significant.

Table 29. The *t*-test results for GRIM5C1 based on LAGEOS 2 data.

Variable	Diff (mean SD)	Diff. (SD)	*t*-value	*p*-value
Var 1 vs. Var 2	0.000230	0.008858	0.32710	0.744027
Var 1 vs. Var 3	0.000269	0.009625	0.35287	0.724659
Var 1 vs. Var 4	0.000039	0.009065	0.05406	0.956954
Var 2 vs. Var 3	0.000040	0.002298	0.21727	0.828282
Var 2 vs. Var 4	-0.000191	0.001383	-1.74026	0.083761
Var 3 vs. Var 4	-0.000230	0.002202	-1.32019	0.188680

Table 30 summarises the *t*-test results for the EIGEN-CG03C model based on LAGEOS 2 data. Based on the results presented in Table 30 there are no statistically significant differences in the mean SD between Var 1 versus Var 2, Var 1 versus Var 3, Var 1 versus Var 4 and Var 2 versus Var 4 tests (since $p \geq 0.05$). In contrast the computed *t*-values between Var 2 versus Var 3 and Var 3 versus Var 4 correspond to *p*-values less than the risk level, 0.05 implying that the mean SD differences between the two groups are statistically significant for the EIGEN-CG03C model.

Table 30. The *t*-test results for EIGEN-CG03C based on LAGEOS 2 data.

Variable	Diff (mean SD)	Diff. (SD)	*t*-value	*p*-value
Var 1 vs. Var 2	0.000762	0.012549	0.76336	0.446393
Var 1 vs. Var 3	-0.001170	0.013784	-1.06735	0.287453
Var 1 vs. Var 4	0.000778	0.012646	0.77322	0.440555
Var 2 vs. Var 3	-0.001933	0.008310	-2.92330	0.003976
Var 2 vs. Var 4	0.000016	0.001819	0.10920	0.913180
Var 3 vs. Var 4	0.001948	0.008341	2.93607	0.003824

The results for the *t*-test as derived from the four orbital tests using AIUG-CHAMP01S and LAGEOS 2 are presented in Table 31. These results however, indicate that the differences in the mean SD for each condition are not statistically significant (since $p \geq 0.05$).

Table 31. The *t*-test results for AIUB-CHAMP01S based on LAGEOS 2 data.

Variable	Diff (mean SD)	Diff. (SD)	*t*-value	*p*-value
Var 1 vs. Var 2	0.000143	0.009214	0.195760	0.845049
Var 1 vs. Var 3	0.000243	0.009204	0.333253	0.739385
Var 1 vs. Var 4	0.000169	0.009250	0.230246	0.818199
Var 2 vs. Var 3	0.000100	0.001663	0.759639	0.448603
Var 2 vs. Var 4	0.000026	0.001485	0.219537	0.826515
Var 3 vs. Var 4	-0.000074	0.001488	-0.630220	0.529461

Table 32 summarises the *t*-test results for the EGM2008 gravity field model based on LAGEOS 2 data. The results indicate that the differences in the mean SD between the first five groups are not statistically significant (i.e. $p \geq 0.05$). Similar results are obtained for the AIUB-GRACE01 gravity field model using LAGEOS 2 data, see Table 33. In both cases the difference in the mean SD between Var 3 versus Var 4 groups are statistically significant since $p \leq 0.05$.

Table 32. The *t*-test results for EGM2008 based on LAGEOS 2 data.

Variable	Diff (mean SD)	Diff. (SD)	*t*-value	*p*-value
Var 1 vs. Var 2	0.000278	0.009269	0.37783	0.706065
Var 1 vs. Var 3	0.000411	0.009389	0.55250	0.581384
Var 1 vs. Var 4	0.000141	0.009568	0.18556	0.853026
Var 2 vs. Var 3	0.000134	0.001317	1.27969	0.202532
Var 2 vs. Var 4	-0.000137	0.001615	-1.06938	0.286529
Var 3 vs. Var 4	-0.000271	0.001463	-2.33254	0.020934

Table 33. The *t*-test results for AIUB-GRACE01S based on LAGEOS 2 data.

Variable	Diff (mean SD)	Diff. (SD)	*t*-value	*p*-value
Var 1 vs. Var 2	0.000460	0.009136	0.63494	0.526388
Var 1 vs. Var 3	0.000326	0.009217	0.44596	0.656240
Var 1 vs. Var 4	0.000579	0.009249	0.78940	0.431059
Var 2 vs. Var 3	-0.000134	0.001715	-0.98588	0.325697
Var 2 vs. Var 4	0.000119	0.001650	0.90935	0.364550
Var 3 vs. Var 4	0.000253	0.001298	2.45936	0.014997

Figure 20 compares the gravity field models found to exhibit O-C mean SD differences that are statistically significant. In particular, for LAGEOS 1 data only the combined gravity field model GRIM5C1 has *t*-values corresponding to *p*-values less than the 0.05 risk level. The *p*-value for Var 2 versus Var 4 is however too close to the significant level hence the difference in the mean SD of the O-C is likely to have arisen by chance. In this case it becomes difficult to firmly conclude anything about the statistical significance of the mean difference (additional data processing is needed to ascertain the findings). The small *p*-values obtained for EIGEN-CG03C when analysing LAGEOS 2 data imply that the findings are unlikely to have arisen by chance. In fact the difference in the mean SD of the O-C between Var 2 versus Var 3 and Var 2 versus Var 4 tide parameterization tests are highly statistically significant since $p \leq 0.01$. Similarly, the *p*-values computed from the *t*-test using the O-C residuals derived from LAGEOS 2 data based on the EGM2008 and AIUB-GRACE01S models indicate that there are almost true differences in the mean SD between Var 3 versus Var 4 tide parameterization tests.

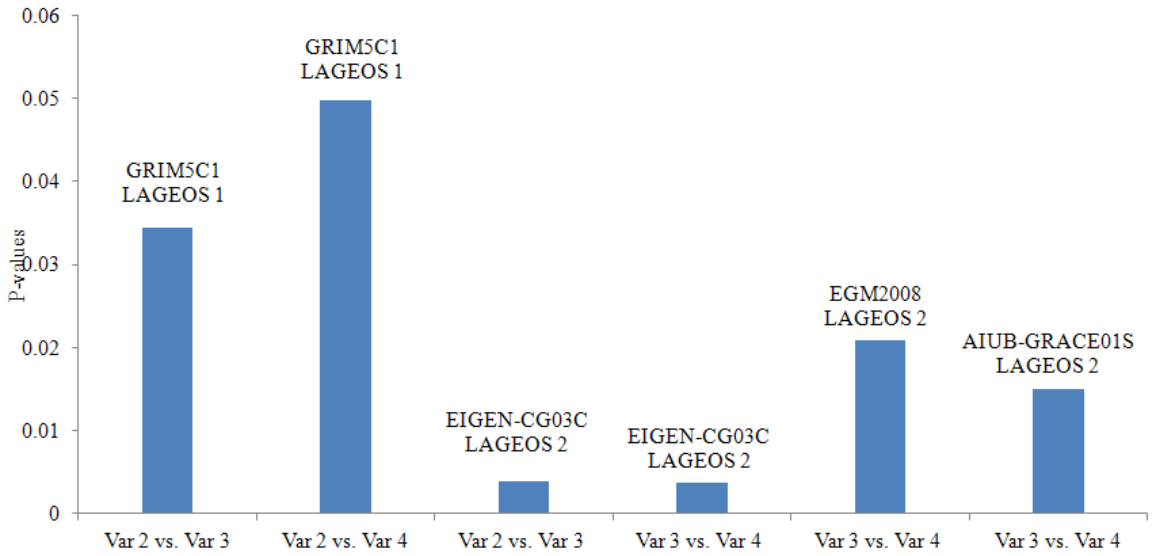

Figure 20. Comparisons of gravity field models showing mean statistical significant differences between Earth tide and pole tide models.

5.7. Concluding remarks

In this chapter the influence of tide parameterization on the accuracy of five gravity field modes is analysed. In particular, the tide parameterization effects on the accuracy of gravity field models in SLR data analysis is determined by studying the influence of solid Earth tides (modelled by IERS1, IERS2, IERS3 and IERS2010 pole tide standard model) on O-C residuals (with applications in POD) based on the selected gravity field models. In the SLR data analysis using the SDAS package the IERS1, IERS2, IERS3 and pole tide models have been used alternately (parameterized) in order to investigate how the O-C residuals are affected by the choice of the tide model set and across different gravity field models. The results indicate that the accuracy of the final orbital solution when using EIGEN-CG03C, AIUB-CHAP01S and EGM2008 and LAGEOS 1 data require the inclusion of spherical harmonic components due to Earth and pole tides to those of the gravity field models. Similar conclusions can be made for the GRIM5C1, AIUB-CHAMP01S and EGM2008 models when using LAGEOS 2 data. Since the computed mean SD across the four parameterizations based on the five gravity field models was statistically close a *t*-test was performed to assess whether the differences in the mean SD of the O-C were significantly different. The *t*-tests between most of the considered parameterization options are found to have *p*-values which were greater than the significant

level 0.05 (or 5%). Based on these results it can be concluded that the differences in the mean SD between the considered parameterization options for the selected gravity field models are not statistically significant. In particular, the differences in the mean SD of the O-C based on EIGEN-CG03C, EGM2008 and AIUB-GRACE01S and LAGEOS 2 data are unlikely to have arisen by chance as they exhibit statistically significant mean SD differences. In particular the small *p*-values obtained for EIGEN-CG03C imply that the differences in the mean SD are highly statistically significant. The deviation of EIGEN-CG03C from the expected is difficult to explain. This model produces expected results for IERS1, IERS2 and IERS3 (pole tide disabled), but produces an anomaly when processing for LAGEOS2 with IERS3 enabled and pole tide disabled. This distorts the graph of average values as contained in Figure 18. These distortions are possibly due to outliers in the O-C time series as presented in appendix A5, Figure 24 to Figure 33.

6. Geophysical applications of Earth's oblateness parameter J_2

Physics is mathematical not because we know so much about the physical world, but because we know so little; it is only its mathematical properties that we can discover, Bertrand Russell, 2009.

6.1. Introduction

The Earth's oblateness (J_2) is an important geophysical parameter derived from SLR data analysis. In the present chapter, J_2 computed by SDAS has been validated and found to be in close agreement with the J_2 value published in the literature. Additionally, the geophysical linkage of J_2 with the LOD and Atmospheric Angular Momentum (AAM) has been studied and confirmed by use of a data adaptive analysis methodology called the Empirical Mode Decomposition (EMD) reported by Wang *et al*., (2010). In particular, the oscillatory components known as the Intrinsic Mode Functions (IMFs) of J_2, LOD and AAM were derived and phase synchronization used to infer the geophysical linkage between J_2, LOD and AAM. The phase synchronization results demonstrate that there is some degree of synchronization between the signal components of J_2 and LOD and J_2 and AAM. A higher degree of phase synchronization is particularly observed for high frequency IMFs of J_2, LOD and AAM. Additionally, IMFs components that depict a weak or nil phase synchronization are believed to be mostly due to inherent noise components.

6.2. Background

The Earth is a complex dynamic system driven by various geophysical processes as reported by for example Dickey *et al*. (2002). These processes act to redistribute the mass of Earth and as a result influence the basic movement of the solid Earth relative to the geocentre, as well as causing spatial and time-dependent variations of the gravitational field of the Earth. An important spherical harmonic coefficient of the gravity field is the zonal harmonic of degree 2 and order 0, i.e. $-C_{20}$ which is equivalent to J_2. This coefficient is known to be related to the flattening of the Earth as well as to the angular spin velocity Ω (this is connected to the equatorial and polar moments of inertia given by (A) and (C) respectively) (Chao, 2006).

Considering the equatorial and polar moments of inertia, the J_2 coefficient can be expressed as in Equation (91) as reported in Chao (2006),

$$J_2 = \frac{(C - A)}{Ma^2}. \tag{91}$$

Equation (91) contains the difference of the polar greatest moment of inertia C and the equatorial minimum moment of inertia A normalized by Ma^2, where M and a are the Earth's mass and mean equatorial axis respectively. A further expression of J_2 relating to dynamic oblateness may be written as in Equation (92),

$$J_2 = \left[C / Ma^2\right]\left[(C - A)/C\right] \equiv \eta H, \tag{92}$$

In Equation (92), $\eta \equiv C / Ma^2$ is a fundamental function of the Earth's internal structure and $H \equiv (C - A)/C$ is the dynamic oblateness (the dynamic oblateness can be determined from the observation of the astronomical precession of the Earth). Knowing the estimated values of J_2 one can use the following relation to calculate the normalized values of C_{20} as shown in Equation (93),

$$\bar{J}_2 = -\bar{C}_{20} = -\sqrt{5}\overline{C_{20}}. \tag{93}$$

The estimated J_2 coefficient as determined from geodetic measurements may be given by Equation (94) (Cheng *et al.*, 1997)),

$$\begin{aligned} J_2 = -J_2^{(0)} &= \left[C - \frac{1}{2}(A + B)\right]\left(\frac{1}{Ma_0^{\,2}}\right). \\ &= (1082639.9 \pm 0.1) \times 10^{-9} \end{aligned} \tag{94}$$

The Earth oblateness parameter J_2 has attracted a lot of interest from the scientific community since the detection of its temporal variations over two decades ago. In particular, some studies have reported on significant temporal variability exhibited by this coefficient. For example, Yoder *et al.* (1983) reported a secular decrease of the trend in J_2 which was suspected to be associated with PGR effects. An increasing trend in J_2 which later reversed to its normal decreasing trend in the beginning of 1998 was reported by Cox and Chao (2002). The authors estimated the decrease in J_2 between 1979 and 2002 to be approximately -2.8×10^{-11} yr^{-1}.

The variability of J_2 has also been linked to variations observed in other geophysical parameters. One such parameter is the LOD which characterizes the variability of the Earth's rotation rate. Variations in LOD are due to contributions from surface mass loading changes as well as changes of the horizontal surface stress (torques). Surface mass loading variations are due to changes in atmospheric surface pressure, continental water storage (including snow and ice on land), and ocean bottom pressure (Chen *et al*., 2000). In contrast, the horizontal surface stress variations reflect the exchange of angular momentum between the solid Earth and the surrounding geophysical fluids e.g., wind and ocean current variations (Chen *et al*., 2000). The changes due to the combined atmospheric wind and surface pressure effects (i.e., the AAM) which arise from the mass re-distribution and the movement within the Earth system is known to be the dominant contributor (~90%) to the observed LOD variability (Chen 2005b).

Variations in the LOD are often modelled by two terms i.e., the mass and motion components as reported in Bourda (2008). The physical manifestation of the mass term (this is due to dynamic processes within the Earth) is modelled by the gravitational effects associated with the Earth's mass re-distribution. Most of the dynamic Earth processes that are associated with the temporal variations of the Earth's gravitational field are also linked to the variability of the Earth's rotation, through the temporal changes in LOD (Gross, 2003). Theoretically, the LOD variations are thought to be slightly proportional to changes in degree-2 spherical harmonic coefficients of the gravity field (Eubanks, 1993; Gross *et al*. 2004). The response to the LOD variability can approximately be given by Equation (95) as reported in Chen (2005b),

$$-\frac{\Delta LOD}{LOD_{mean}} = m_3(t) = \chi_3, \tag{95}$$

where ΔLOD are the changes in the LOD with respect to the mean LOD, LOD_{mean} is given by 86400 seconds, and χ_3 is the LOD excitation which includes the surface mass load change term $\left(\chi_3^{mass}\right)$ and the atmospheric winds or currents term $\left(\chi_3^{motion}\right)$.

In a case where a gridpoint (i.e., latitude φ, longitude λ and time t) is given the LOD excitations due to surface mass load fluctuations χ_3^{mass} and winds or currents motion χ_3^{motion} can be computed by using Equations, (96) and (97), all reported in Chen (2005b)

$$\chi_3^{mass} = \frac{0.753\bar{R}^4}{C_m g}\iint P\cos^3\varphi d\lambda d\varphi, \tag{96}$$

$$\chi_3^{motion} = \frac{0.998\bar{R}^3}{C_m g \Omega} \iiint U \cos^2\varphi d\rho d\lambda d\varphi, \tag{97}$$

where $\bar{R} = 6.371\times10^6$ m and $\Omega = 7.292115\times10^{-5}$ rad-s^{-1} are the mean radius and mean angular velocity of the Earth, respectively. Furthermore $g \approx 9.81$ ms^{-2} is the mean gravitational acceleration, $C_m \approx 7.1236\times10^{37}$ kg m^2 is the third principal moment of inertia of the Earth's mantle, and P and U are the atmospheric surface pressure (mass term) and the zonal velocity (e.g., wind or ocean currents) respectively (Chen, 2005b). The surface mass change is often represented by the spherical harmonic coefficient of a geopotential depicted in Equation (98).

$$\begin{Bmatrix}\Delta C_{nm}\\ \Delta S_{nm}\end{Bmatrix} = \frac{R_e^{\,2}}{(2n+1)M} \iint \Delta\sigma(\theta,\lambda)\,\bar{P}_{nm}(\sin\theta)\cdot\begin{Bmatrix}\cos m\lambda\\ \sin m\lambda\end{Bmatrix}\cos\theta d\theta d\lambda. \tag{98}$$

In Equation (98), C_{nm} and S_{nm} are the degree n and order m normalized harmonic coefficients of mass decomposition, $\Delta\sigma(\theta,\lambda)$ is the surface mass load with $\Delta\sigma = \Delta P / g$ and M is the mass of Earth and $\bar{P}_{nm}$ is the 4π normalized associated Legendre function given by Equation (99),

$$\left[\frac{(2-\delta_{m0})(2n+1)(n-m)!}{(n+m)!}\right]^{1/2} \times P_{nm}. \tag{99}$$

The associated Legendre function of degree 2 and order 0 can be expressed as in Equation (100)

$$P_{2,0} = \frac{(3\sin^2\theta - 1)}{2}. \tag{100}$$

Applying the normalization factor given by Equation (99) to Equation (100) the normalized associated Legendre function of degree 2 and order 0 can be written as

$$\bar{P}_{2,0} = \sqrt{5}\cdot\frac{(3\sin^2\theta - 1)}{2}. \tag{101}$$

Based on Equation (95), the relationship between the LOD excitation with respect to the surface mass term χ_3^{mass} and the zonal harmonic spherical harmonics, $-C_{20}$ can be obtained by combining Equations (96) and (101) (Chen, 2005b and Bourda, 2008),

$$\chi_3^{mass} = \frac{0.753\bar{R}^2 M}{(1+k_2^{'})C_m}\cdot\frac{2}{3}\left(\Delta C_{00} - \sqrt{5}\Delta C_{20}\right). \tag{102}$$

Here M is the mass of the Earth, $k_2^{'} = -0.301$ is the degree-2 load Love number and C_{00} represents the total mass change of a given component normalized by mass of the Earth, i.e., $C_{00} = \Delta M / M$.

The motion part of the AAM component can be related to changes in LOD by Equation (103) (Bourda, 2008)

$$\frac{\Delta LOD_{winds}(t)}{LOD_{mean}} = \frac{h_{3\text{winds}}(t)}{C_m \Omega}, \qquad (103)$$

where h_3 is the axial relative angular momentum of the Earth corresponding to the winds or motion term. The linkage between J_2 and LOD is an important scientific investigation because of the geophysical applications in areas such as hydrology, atmosphere and ocean coupling. One way to establish the association between J_2 and LOD is to investigate the possible coherence of various modes of oscillation in the J_2 coefficient with those estimated from LOD fluctuations. Additionally, since the variations in LOD are also closely linked to those in the AAM it then follows that some modes of oscillation of J_2 could be synchronized with those of the AAM as reported in Sole *et al*. (2007). In the present analysis of phase synchronization, we investigate the linkage between J_2 and LOD as well as J_2 and AAM, based on the independent oscillatory components obtained from each of these geophysical parameters.

6.3. Inter-comparisons between SDAS estimated J_2 and a priori J_2 of EGM96, GRIM5C1, GGM03C and AIUB-GRACE01S models.

In the present study, the robustness of the analysis of SLR data by use of the SDAS package parameterization has been tested generally by comparing the values of unnormalised *a-priori* and estimated J_2 values based on the EGM96, GRIM5C1, GGM03C and AIUB-GRACE01S gravity field models. The purpose of the analysis was to validate J_2 computed from SLR data analysis using SDAS against the published values from the five selected gravity field models. Here the published J_2 values for each gravity field model and results obtained by using SDAS are summarized in Table 34 and Table 35. During processing the *a-priori* J_2 values are set as starting points in the estimation, and the formal errors of the GGM being used is set as the

estimation parameter constraint. The least-squares solution of J_2 is therefore constrained fairly tightly. Figure 21 depicts a comparison between *a-priori* J_2 values and those derived from SDAS data analysis based on the EGM96, GRIM5C1, GGM03C AND AIUB-GRACE01S gravity field models. In particular the plotted values are the differences between the normalized *a-priori* J_2 values and the SDAS derived J_2 based on LAGEOS 1 and 2 across the considered gravity field models. The results presented in Figure 21 indicate that the *a-priori* J_2 and the SDAS derived J_2 exhibits similar patterns and are in good agreement for all the GGMs as processed using LAGEOS 1 and 2 data.

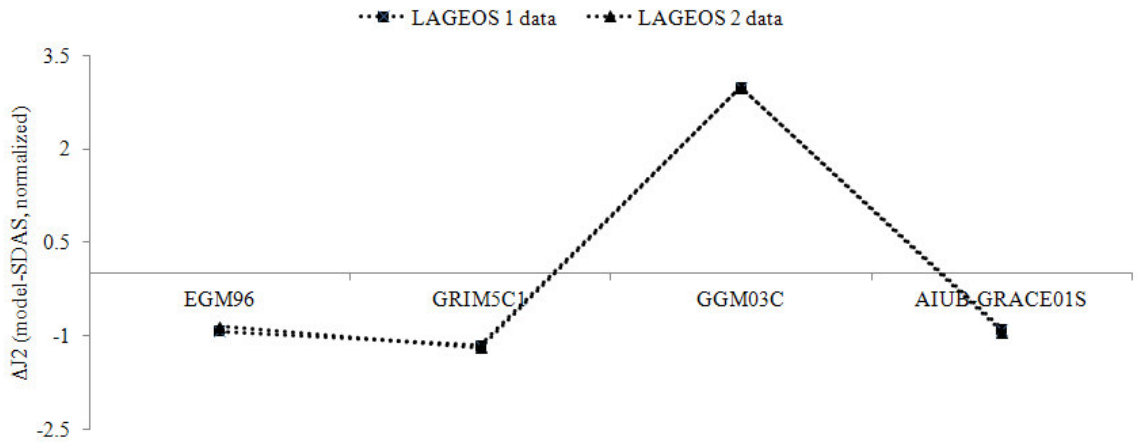

Figure 21. Comparison between *a-priori* J_2 values and those derived from SDAS data analysis. The plotted values are the differences between a priori J_2 values and SDAS derived in the normalized form.

As illustrated in Table 34 and Table 35, based on LAGEOS 1 and 2 data sets, the percentage differences (absolute) between the *a-priori* and SDAS estimated J_2 are in the order of 10^{-8} for all the considered GGMs. These results therefore suggest that the J_2 derived from SDAS could be used to compute normalized J_2 values that would be very similar to the published ones. No attempts were made to adjust *a-priori* values for $\dot{J}_2$ as the uncertainties in $\dot{J}_2$ are at the formal error level for the particular models used. Therefore one must consider that the epoch of the GGMs are not neccessarily those of the mid-epoch period of the processed SLR data (December

2005 to December 2008). Nevertheless, the SDAS package provides reasonable estimates with the J_2 *a-priori* values differing at the 10^{-10} to 10^{-11} level.

Table 34. Comparisons of *a- priori* J_2 from the five GGMs and J_2 derived from SDAS based on LAGEOS 1 data.

Model	A priori $J_2 \times 10^{-3}$	Formal error$\times 10^{-11}$	SDAS $J_2 \times 10^{-3}$	SDAS formal error $\times 10^{-11}$	$\Delta J_2 \times 10^{-10}$ (Model -SDAS)
EGM96	-1.0826267	3.561063	-1.0826268	7.8449	1.19859
GRIM5C1	-1.0826261	0.409800	-1.0826262	0.9162	1.69544
GGM03C	-1.0826355	4.684600	-1.0826368	0.1024	0.12672
AIUB-GRACE01S	-1.0826267	0.504104	-1.0826270	1.1270	2.66310

Table 35. Comparisons of *a-priori* J_2 from the five GGMs and J_2 derived from SDAS based on LAGEOS 2 data.

Model	A priori $J_2 \times 10^{-3}$	Formal error$\times 10^{-11}$	SDAS $J_2 \times 10^{-3}$	SDAS formal error $\times 10^{-11}$	$\Delta J_2 \times 10^{-10}$ (Model - SDAS)
EGM96	-1.0826267	3.561063	-1.08262673	7.8902	6.54752
GRIM5C1	-1.0826261	0.409800	-1.0826263	0.7634	1.19854
GGM03C	-1.0826355	4.684600	-1.0826369	0.1023	0.13675
AIUB-GRACE01S	-1.0826267	0.504104	-1.0826268	1.1268	1.19356

6.4. Geophysical modes of oscillation inherent in LOD, AAM and J_2

In this section the linkage between J_2 and LOD as well as J_2 and AAM geophysical parameters is investigated by use of a recent, widely used data adaptive analysis methodology, the EMD described in Huang *et al.* (1998). The data used to extract oscillation components of J_2 are the same as that presented in Chapter 4 for the EGM96, GRIM5C1, GGM03C and AIUB-GRACE01S models. The LOD data used in this study is the official IERS EOP 08 C04 product series archived and freely available from ftp://hpiers.obspm.fr/iers/eop. The LOD data are computed from VLBI, GPS and SLR space geodetic techniques. Similarly, the AAM data used in the present study were the National Centers for Environmental Prediction (NCEP) effective atmospheric angular momentum functions calculated from NCEP/NCAR (National Center for Atmospheric Research) reanalyses archived on pressure levels. The AAM data are

freely available at the geophysical fluid: the Special Bureau for the Atmosphere (SBA), ftp://ftp.aer.com/pub/anon_collaborations/sba. For the purpose of this work both the LOD and AAM data period were matched with the analysed period of SLR observations. Properties of the J_2, LOD and AAM were analysed using a modified Ensemble Empirical Mode Decomposition (EEMD) method reported in e.g., Botai *et al.* (2009) and Zhaohua and Huang (2009).

The EEMD methodology is a data adaptive method of decomposing a series into local oscillatory components called the IMFs originally reported in Zhaohua and Huang (2009). According to Zhaohua and Huang (2009), an IMF is a mono-component signal that satisfies two conditions:

1. In the whole data set, the number of extrema and the number of zero crossings must either equal or differ at most by one;
2. At any point, the mean value of the envelope defined by the local maxima and the envelope defined by the local minima is zero.

The EEMD method is a variant of the original EMD developed by Huang *et al.* (1998). This method is used for analysing non-stationary and non-linear signals driven by underlying linear and non-linear stochastic processes. In general, the EMD method extracts oscillatory components from a given series by an iterative procedure known as the *sifting process* (SP). Here for any given data, a signal is decomposed into a series of IMFs generated at each scale starting from smooth to coarse and a residual representing a trend function. According to Huang *et al.* (1998), the EMD algorithm can be summarized as follows:

1. For a given data denoted by $x(t)$, identify all the local extrema.
2. Interpolate all the maxima and minima with natural cubic splines lines to form the upper $u(t)$ and lower, $l(t)$, envelopes.
3. Compute the mean of the envelopes: $m(t) = \dfrac{\left[u(t) + l(t)\right]}{2}$.
4. Take the difference between the data and the mean as the proto-IMF: $h(t) = x(t) - m(t)$.
5. Check the proto-IMF against the definition of the IMF and the stoppage criterion to determine if it is an IMF.

6. If the proto- IMF doe not satisfy the IMF definition then repeat steps 1 to 5 on $h(t)$ until it satisfies the definition.
7. If the proto- IMF satisfies the definition, assign the proto- IMF as an IMF component, $c(t)$.
8. Iterate on the residue, $f(t) = x(t) - c(t)$, as on the data. This process will end when the residue reaches a non-existence of extrema.

The flow chart of the sifting process is depicted in Figure 22.

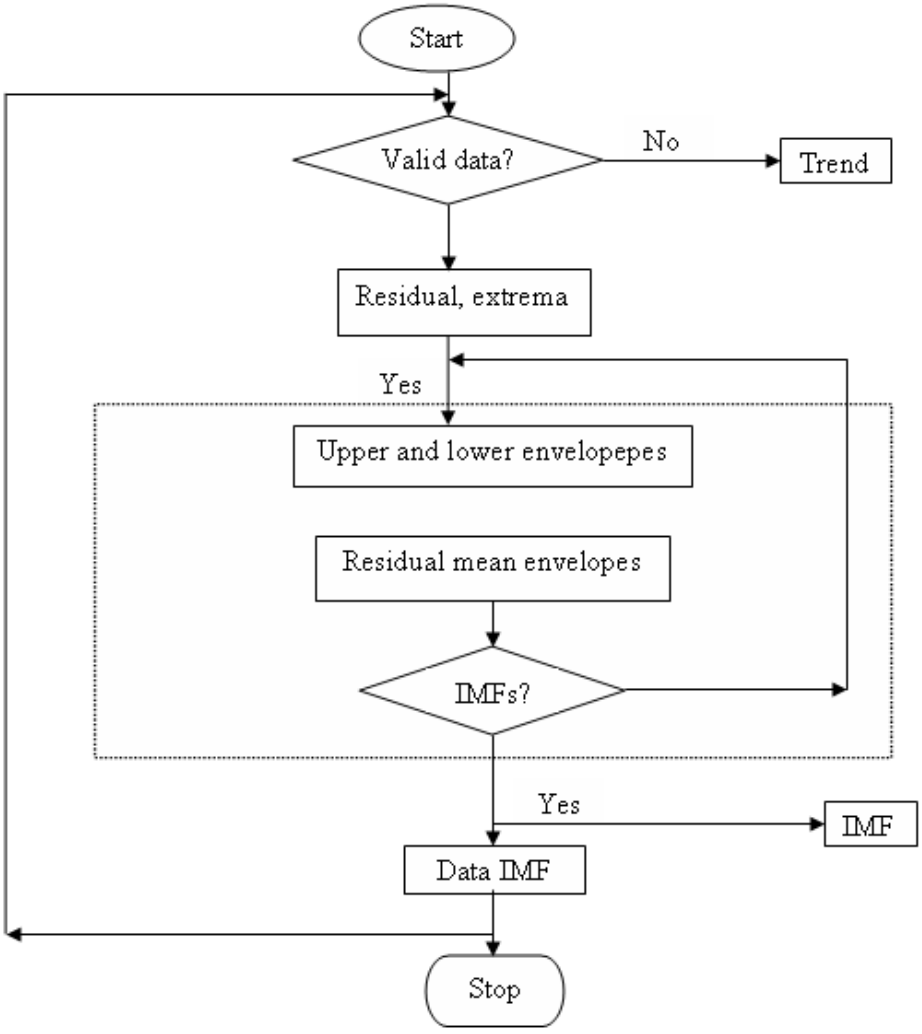

Figure 22. The flow chart of the decomposition process of EMD through the sifting procedure (adapted from Wang *et al*., 2010).

Mathematically, the sifting process can be described as follows in Equation (104)

$$\begin{aligned} &x(t)-m_{1,1}(t)=h_{1,1}(t);\\ &h_{1,1}(t)-m_{1,1}(t)=h_{1,2}(t);\\ &\quad\ldots\\ &\quad\ldots\\ &h_{1,k-1}(t)-m_{1,k}(t)=h_{1,k}(t).\\ &\Rightarrow\ h_{1,k}(t)=c_1(t) \end{aligned} \tag{104}$$

Here the indices indicate the iteration of the same step. It then follows that

$$\begin{aligned} &x(t)-m_{1,1}(t)=h_{1,1}(t);\\ &h_{1,2}(t)=h_{1,1}(t)-m_{1,2}(t)=s(t)-(m_{1,1}+m_{1,2});\\ &\ldots\\ &\ldots\\ &h_{1,k}(t)=h_{1,k-1}(t)-m_{1,k}(t)=x(t)-(m_{1,1}+m_{1,2}+\ldots+m_{1,k});\\ &\Rightarrow\ \ c_1(t)=x(t)-(m_{1,1}+m_{1,2}+\ldots+m_{1,k}). \end{aligned} \tag{105}$$

The step presented here serves to extract the first IMF component. Subsequently, one finds that

$$\begin{aligned} &x(t)-c_1(t)=r_1(t);\\ &r_1(t)-c_2(t)=r_2(t);\\ &\ldots\\ &\ldots\\ &r_{r-1}(t)-c_n(t)=r_n(t). \end{aligned} \tag{106}$$

Thus for any given data, the signal $x(t)$, can be decomposed by the EMD method as

$$x(t)=\sum_{j=1}^{n}c_j(t)+r_n(t), \tag{107}$$

where c_j represents the j^{th} IMF and r_n is the residual.

In the present analysis of the oscillatory mode decomposition of J_2, LOD and AAM the following algorithm steps (is illustrated in Figure 23) were followed:

a) Compute IMFs by use of a noise assisted data analysis method based on Zhaohua and Huang (2009).
b) Determine significant IMFs based on the energy criterion.
c) Compute the phase difference of the analytic signals of the selected IMFs.

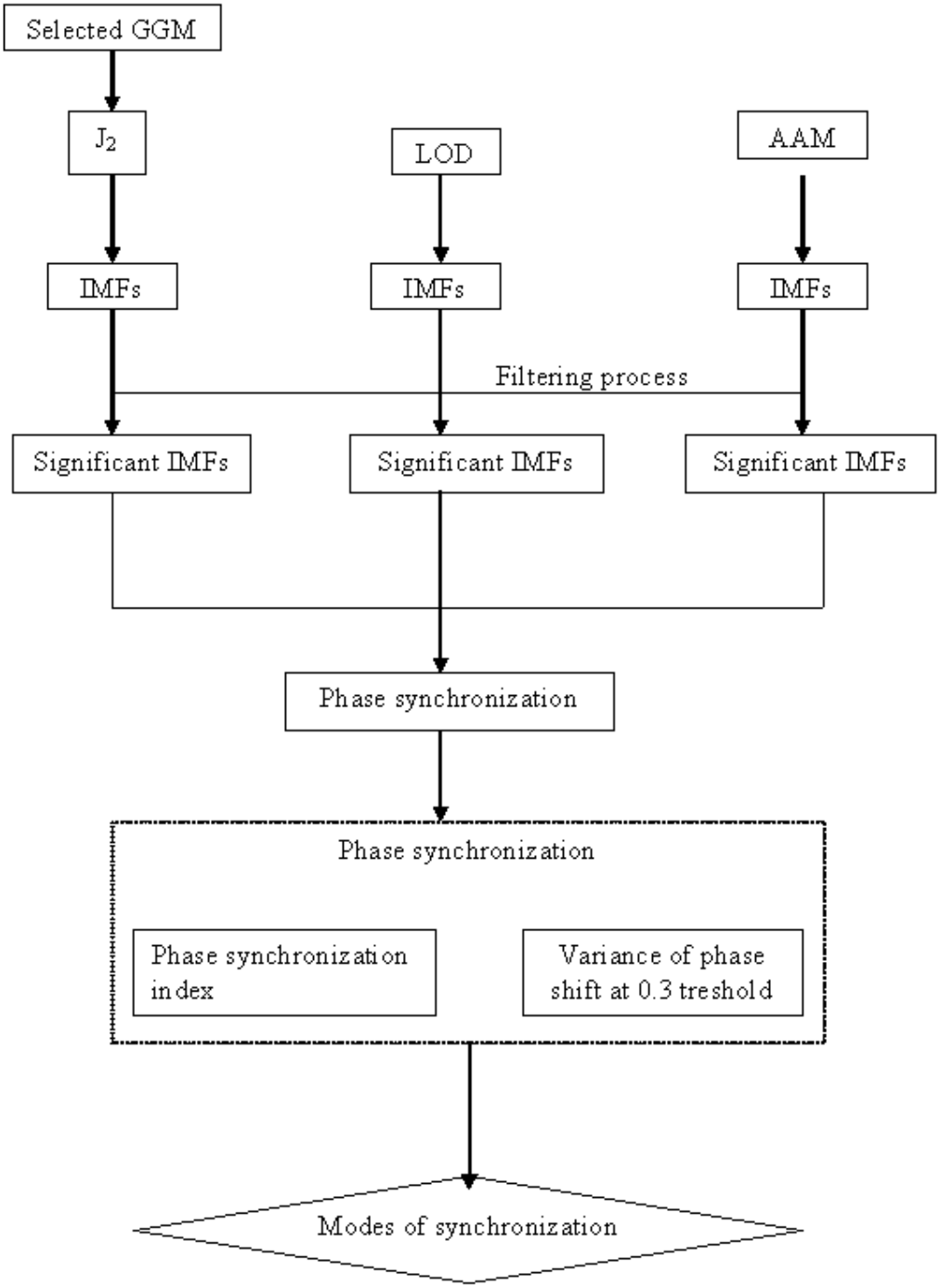

Figure 23. Synchonization method used in the current study.

In this work, only significant IMFs were selected to investigate the association of J_2 oscillatory components with those from LOD and AAM. The significant IMFs were selected based on the energy criteria: their energy ought to be within the inter-quartile range of the IMF with maximum energy from a total of 10 IMFs decomposed adaptively by use of 0.33σ noise level with 50 ensembles. Intrinsic Mode Functions with small instantaneous amplitudes/energy and high frequencies were considered as outliers.

6.4.1. Analysis of phase synchrony

In order to quantify the level of synchrony across the recorded IMFs from J_2, LOD, and AAM geophysical parameters the Phase Locking Value (PLV) approach reported in Sole at al. (2007) was used. In particular, for two signals $x(t)$ and $y(t)$ of equal time length with instantaneous phase $\Phi_x(t)$ and $\Phi_y(t)$ respectively, the PLV bivariate metric is given by Equation (108),

$$PLV = e^{i\Delta\Phi_{xy}(t)} = \left| \frac{1}{N} \sum_{j=1}^{N} e^{\left(i\left(\Phi_x(j\Delta t) - \Phi_y(j\Delta t)\right)\right)} \right|, \tag{108}$$

where Δt is the sampling period and N is the number of points in the sampling period of each signal.

The corresponding IMFs extracted from J_2 (based on four selected gravity field models), LOD and AAM were analyzed to detect the level of interaction between J_2 and LOD as well as J_2 and AAM mode signals. Here we only consider phase locking as an important factor and impose no restrictions on the amplitudes. In general, a phase locking ratio of 1:2 was considered appropriate for our analysis. Furthermore, we calculate the variance of the phase shift and determine the degree of phase synchronization based on a 0.3 threshold. The usage of this low threshold cut-off is to eliminate IMFs that primarily consist of noise. Generally, the frequencies ω_x and ω_y of any two given periodic oscillators are related by $n\omega_x = m\omega_y$ where n and m are integers. If a phase for each oscillator is defined by Equation (109),

$$\phi_j(t) = w_j t, \tag{109}$$

then the principle of phase synchronization corresponds to a phase locking between two oscillators defined by Equation (110),

$$\varphi_{n,m} = \left| n\phi_X(t) - m\phi_Y(t) \right| \leq C, \qquad (110)$$

where ϕ_X and ϕ_Y are the unwrapped phases of the signals of the two oscillators and this is equivalent to a constant, C. Equation (110) can now be used to derive the phase synchronization index defined in Equation (111) as reported in Hutt *et al*. (2003) and Allefeld and Kurths (2003),

$$\gamma_m(t) = \frac{1}{\tau}\sqrt{\left(\sum_{i=-\tau/2}^{\tau/2}\cos\left(\Delta\phi_m(t+i\Delta T)\right)\right)^2 + \left(\sum_{i=-\tau/2}^{\tau/2}\sin\left(\Delta\phi_m(t+i\Delta T)\right)\right)^2}. \qquad (111)$$

Here τ denotes the number of time points in the sliding window of width ΔT. The computed variance normally varies between 0 and 1, i.e., $0 \leq \gamma_m \leq 1$. Assuming that $\phi_m(t)$ represents the difference between two phases that change at certain times, then $\gamma_m(t)$ can be used to define the phase synchronization index. It follows that the maximum value of $\gamma_m(t) = 1$ would indicate a perfect synchronization between phases with phase difference ϕ_m. Similarly, a zero phase synchronization between phases with phase difference ϕ_m would be achieved when $\gamma_m(t) = 0$.

The phase synchronization results between signal components extracted from J_2 and those extracted from LOD and AAM can be found in Appendix A6, Figure 34 to Figure 49. Visual inspection of these figures suggests that there exists some degree of synchronization between J_2 signal components and those from LOD and AAM. In particular, ~70% of the signal components extracted from J_2 data show a high degree of synchronization with those derived from LOD and AAM signals. The higher phase synchronization seems to be located at the high frequencies in the case of J_2 and LOD and J_2 and AAM. The presence of synchronization between J_2 components and components from LOD and AAM suggests that the LOD and AAM signal components are embedded in the data hence confirming that the two parameters are related as stated in the literature. Pairs showing high synchronization between J_2 from LAGEOS 1 and 2 data and LOD and AAM are summarized in Table 36 and Table 37 respectively. The calculated phase synchronization index for these pairs ranges between 0.01 and 0.3 based on phase locking ratio of 1:2. Components showing weak behaviour of asynchrony or no synchronization at all between J_2 and LOD and AAM respectively could be a

result of random noise between the signal components of the interacting signals or irregular variability in the J_2 signal.

Table 36. Phase synchronization pairs showing a high degree of synchronization between J_2 and LOD.

J_2 derived from LAGEOS 1 based on model	Synchronized pairs between J_2 and LOD
EGM96	δ_{14}, δ_{15}, δ_{17}, δ_{35} and δ_{47}
GRIM5C	δ_{13}, δ_{14}, δ_{17}, δ_{34} and δ_{47}
GGM03C	δ_{13}, δ_{14}, δ_{17}, δ_{34} and δ_{47}
AIUB-GRACE01S	δ_{14}, δ_{15}, δ_{17}, δ_{35} and δ_{47}
J_2 derived from LAGEOS 2 based on model	Synchronized pairs between J_2 and LOD
EGM96	δ_{14}, δ_{17}, δ_{24} and δ_{67}
GRIM5C	δ_{14}, δ_{17}, δ_{24}, δ_{47} and δ_{77}
GGM03C	δ_{14}, δ_{17}, δ_{24}, δ_{47} and δ_{77}
AIUB-GRACE01S	δ_{14}, δ_{17}, δ_{24}, δ_{27} and δ_{67}

Table 37. Phase synchronization pairs showing a high degree of synchronization between J_2 and AAM.

J_2 derived from LAGEOS 1 based on model	Synchronized pairs between J_2 and AAM
EGM96	δ_{11}, δ_{13}, δ_{16} and δ_{26}
GRIM5C	δ_{11}, δ_{13} and δ_{16}
GGM03C	δ_{11}, δ_{13}, δ_{16} and δ_{26}
AIUB-GRACE01S	δ_{11}, δ_{13}, δ_{16} and δ_{26}
J_2 derived from LAGEOS 2 based on model	Synchronized pairs between J_2 and AAM
EGM96	δ_{11}, δ_{13}, δ_{16} and δ_{26}
GRIM5C	δ_{11}, δ_{13} and δ_{16}
GGM03C	δ_{11}, δ_{13} and δ_{16}
AIUB-GRACE01S	δ_{11}, δ_{13}, δ_{16}, δ_{26} and δ_{65}

6.5. Concluding remarks

The oscillatory components in the SDAS derived J_2 coefficient based on EGM96, GRIM5C1, GGM03C and AIUB-GRACE01S gravity field models were investigated using SLR data from LAGEOS 1 and 2 for a period of about 3 years (i.e. December 2005 to December 2008). A data adaptive analysis method, EMD was utilized to decompose the J_2, LOD and AAM signals into significant IMFs. The phase synchronization between J_2 and LOD and J_2 and AAM signal components show that there exists some degree of synchronization between the interacting

signals. A higher degree of phase synchronization is observed at high frequencies of J_2, LOD and AAM decomposed IMFs. Components showing a weak or nil phase synchronization are believed to be primarily contaminated by random noise within the signals.

7. Conclusion and recommendations for future research

"Nothing is too wonderful to be true, if it be consistent with the laws of nature" Michael Faraday.

7.1. Summary

Earth gravity field models (these are empirical models that are used to explain the nature of the gravity field of Earth) have significant applications in geodesy, geophysics, oceanography and navigation. In particular, precise gravity field models have been used in:

- The determination of accurate orbits of both low and high orbiting satellites, this is a pre-requisite for the launch, navigation, prediction and tracking of artificial orbiting satellites,
- Precise estimation of the global unified geoids particularly the oceanic geoids,
- Understanding geophysical phenomena of the Earth's interior as well as geodynamic processes associated with the lithosphere and mantle composition,
- Establishment of a global height reference system for datum connection and
- Understanding mass transportation and different distributions within the Earth system through detection and assessment of spatial-temporal variations of the gravitational field of the Earth.

Nowadays several gravity field models derived exclusively from SLR tracking measurements or/and from a combination of SLR measurements with surface gravity measurements (e.g. terrestrial gravity data and airborne gravity data) and satellite radar altimetry measurements have been freely released to the scientific community for research. These models however exhibit certain inaccuracies due to various factors ranging from the type of utilized satellite data, availability and quality of the data, global coverage, accuracies of force models incorporated in the geodetic data analysis, etc. Recent satellite missions such as CHAMP, GRACE and GOCE are believed to have the capability to resolve the long- and medium wavelength features of the Earth's gravity by providing new data for precise and high resolution gravity field modelling. Since the inception of the three satellite missions a number of gravity field models have been derived and some of the old ones have been modified. These progresses in gravity field modelling require that the models be constantly assessed and validated. Despite the many

scientific milestones in gravity field modelling, studies focusing on evaluating the accuracy of the gravity field models in the context of POD using SLR data have remained in-exhaustive. The research work reported in this thesis evaluates various gravity field models in terms of the O-C range residuals, investigates the influence of SLR analysis parameterization on the accuracy of the gravity field models and demonstrates the capability of the SDAS package to investigate the different gravity field models for POD. It is of importance to emphasize that the results presented in this thesis are related to spherical harmonic coefficients up to degree and order 20 as proxies for gravity field models.

7.2. Concluding remarks

The main aim of this research was to evaluate the accuracy of gravity field models used for POD by use of LAGEOS 1 and 2 data collected from ILRS tracking stations. The research began by providing an historical overview of gravity field models intended to highlight the development of gravity field models and their scientific applications. An investigation in general improvement in the gravity field modelling based on the O-C residuals derived from LAGEOS 1 and 2 data using various selected gravity field models was presented in Chapter 4. In Chapter 5 of the thesis we performed a sensitivity analysis on the O-C residuals computed from LAGEOS 1 and 2 tracking data considering 5 gravity field models. The main focus was to investigate the effects of different tide parameterizations on the O-C residuals across different gravity field models. In Chapter 6, some of the SDAS derived products are validated and analysed for geophysical applications. In particular, the J_2 spherical harmonic coefficient derived from the SDAS package was compared with the coefficients published in the literature. In addition, association of the J_2 coefficient with other geophysical parameters (LOD and AAM) was also investigated. Based on the analysis of results presented in this research work the following conclusions can be drawn:

- The development of gravity field modelling over the period of evaluation (15 years) has generally improved. In particular, based on the seven months analysis of SLR data, the accuracy of the evaluated gravity field models depict an improvement by a factor of at least 2 since 1990 in terms of O-C range residuals. The analysis of the O-C residuals reveals that the accuracy of gravity field models released from 1999 onward are

approximately at the same level of accuracy (within the limits of sensitivy of our tests as described in this work), although there are many specific differences amongst most recent gravity field models. A further analysis (for a period of three years) of a set of four gravity field models released between 1996 and 2008 demonstrate slight differences in their O-C range residuals. Overall, in the SLR data analysis (this includes the seven months and ~3 years of LAGEOS 1 and 2 SLR data) undertaken in this study, it was found that the satellite-only derived gravity field model AIUB-GRACE01S could be the most accurate due to the low SD of the corresponding O-C range residuals.

- The influence of tide parameterization (using IERS1, IERS2, IERS3 and IERS2010 pole tide standard model) on the accuracy of five gravity field models was analysed based on LAGEOS 1 and 2 data. The results indicate that the accuracy of the final orbital solution when using EIGEN-CG03C, AIUB-CHAP01S and EGM2008 and LAGEOS 1 data require the inclusion of spherical harmonic components due to Earth and pole tides to those of the gravity field models. Similar results were found for the GRIM5C1, AIUB-CHAMP01S and EGM2008 models when using LAGEOS 2 data. Statistical *t*-tests were performed to assess whether the differences in the mean SD of the O-C are significantly different. Most of the considered parameterization options are found to have *p*-values which are greater than the significant level 0.05 (or 5%) implying that the differences in the mean SD for the selected gravity field models are not statistically significant. Differences in the mean SD of the O-C based on EIGEN-CG03C, EGM2008 and AIUB-GRACE01S and LAGEOS 2 data are unlikely to have arisen by chance. In particular the small *p* values obtained for EIGEN-CG03C imply that the differences in the mean SD are highly statistically significant. In the case were the *p*-values are found to be relatively low but still greater than 0.05 (e.g. $p = 0.08$ for AIUB-GRACE01 and GRIM5C1 based on LAGEOS 1 and 2 data respectively) more data need to be processed to draw firm conclusions.
- The J_2 coefficients derived from the SDAS package are comparable to those published in the literature. Furthermore, the presence of a geophysical signal component in the time-variable J_2 coefficient was assessed by use of the phase synchronization between J_2 and LOD and J_2 and AAM. Our analysis revealed that there exists some degree of

synchronization between the J_2, LOD and AAM signal components. A higher degree of phase synchronization is observed in the high frequency modes of J_2, LOD and AAM of the IMFs obtained from the empirical decomposition of considered time series (J_2, LOD and AAM). Components showing a weak or nil phase synchronization are believed to be primarily contaminated by random noise within the signals.

7.3. Recommendations

7.3.1. Assessment of additional SLR LAGEOS data

A vast quantity of LAGEOS 1 and 2 tracking data ought to be processed to robustly infer the general improvement of gravity field modelling. Gravity field models derived from as early as the 1970's to the most recent (2011/2012) need to be considered in order to track fully the progress in gravity field modelling. Additional investigation involving larger SLR data sets can be valuable in assessing significant accuracy and resolution of the various considered gravity field models.

7.3.2. Probing the significance of SLR parameterization

In this thesis the tidal deformation effects due to IERS Earth and pole tides (models) on the O-C residuals across 5 different models were investigated. The three models (IERS1, IERS2, IERS3 and IERS3 with pole tides disabled) considered are used to correct for the effects of Earth and pole tides on the spherical harmonice coefficients of the GGMs in question. These effects are directly linked to the O-C residuals which represent the orbits of the satellites. However, there are many other factors that affect the orbit solution and hence gravity field models. These include the atmospheric delay/loading, ocean loading, tropospheric effects, displacements caused by solid Earth tides, general relativistic effects, etc. In order to achieve an improved orbit solution these parameters/effects require full understanding in terms of their contributions to precise satellite orbit determination. It is therefore recommended that sensitivity analysis be extended to include these parameters/effects.

7.3.3. Additional satellites

Nowadays the satellite based global gravity field determination is based on three techniques (e.g. continued GNSS tracking, K-band range and range-rate tracking and satellite gradiometry) which involve CHAMP, GRACE and GOCE satellite missions. High accuracy gravity field determination through these satellite missions is attributed to their orbit attitude, observational mode and on-board equipments. The new satellite missions overcome the SLR drawbacks such as uneven orbit tracking by ground stations non-uniform SLR observations. Consequently, evaluation of global gravity field model accuracies can be expanded by processing long term data sets from these satellite missions. Results from these new satellite missions can then be compared to those obtained in this thesis using LAGEOS 1 and 2 data. Other possible satellites to be considered may include those at a greater range of altitudes and inclinations, e.g. Stella and Starlette.

7.3.4. Technical issues

Much needs to be done to improve the quality and distribution of the available data. For example, the state of the ILRS network needs to improve. The network requires more sites, a better geometry, better tracking capabilities, and enhanced data acquisition capabilities. Thus gaps in the Southern Hemisphere and Africa in particular need to be filled with some SLR tracking stations for a more complete data set for validation purposes.

References

1. Allefeld, C., Kurths, J., (2003). Multivariate phase synchronization analysis of eeg data. *IEICE Transactions, Fundamentals*. E86-A(9):2218-2221.

2. Amos, M.J., Featherstone, W.E., (2003). Comparisons of global geopotential models with terrestrial gravity field data over New Zealand and Australia. *Geomatics Research Australasia*. 78:67-84.

3. Andersen, O.B., Hinderer, J., (2005a). Global inter-annual gravity changes from GRACE: Early results. *Geophysical Research Letters*. 32:L01402. http://dx.doi. org/10.1029/2004GL020948.

4. Andersen, O.B., Seneviratne, S.I., Hinderer, J., Viterbo, P., (2005b). GRACE-derived terrestrial water storage depletion associated with the 2003 European heat wave. *Geophysical Research Letters*. 32:L18405. http://dx.doi. org/10.29/2005GL023574.

5. Benjamin, D., Wahr, J., Ray, R.D., Egbert, G.D., Desai, S.D., (2006). Constraints on mantle anelasticity from geodetic observations, and implications for the anomaly. *Geophysical Journal International*. 165:3-16. http://dx.doi.org/10.1111/j.1365- 246X.2006.02915.x

6. Beutler, G., (2004). Revolution in Geodesy and Surveying. IN: Proceedings, FIG Working Week 2004, Athens, Greece, 1-19.

7. Botai, O.J., Combrinck, W.L., Sivakumar, V., (2009). Assessing the degree of synchronisation between geophysical records using the method of instantaneous phase differences, *In* 11th SAGA biennial technical meeting and exhibition. D. Vogt and S. Fourie (eds). ISBN. 978-0-620-44602-0: 588-593.

8. Bouille, F., Cazenave, A., Lemoine, J.-M., Cretaux, J.F., (2000). Geocentre motion from the DORIS space system and laser data to the LAGEOS satellites: Comparison with surface loading data. *Geophysical Journal International*. 143(1):71-82.

9. Bourda, G., (2008). Length-of-day and space-geodetic determination of the Earth's variable gravity field. *Journal of Geodesy*. 82:295-305.

10. Cazenave, A., Nerem, R.E., (2004). Present-day sea level change: Observations and causes. *Reviews of Geophysics*. 42, RG3001 doi:10.1029/2003RG000139.

11. Chao, B.F., (2006). Earth's oblateness and its temporal variations. *C. R. Geoscience*. 338:1123-1129.

12. Chen, J.L., Wilson, C.R., Tapley, B.D., (2005a). Interannual variability of low-degree gravitational change, 1980–2002. *Journal of Geodesy*. 78: 535-543.

13. Chen, J., (2005b). Global mass balance and the length-of-day variation. *Journal of Geophysical Research*. Vol. 110, B08404.

14. Chen, J.L., Wilson, C.R., Eanes, R.J., Tapley, B.D., (2000). Assessment of long-wavelength gravitational variations. *Journal of geophysical research*. Vol. 105 (B7):16271-16277.

15. Cheng, M., Ries, J.C., Chambers, D.P., (2009). Evaluation of the EGM2008 Gravity Model, Newton's Bulletin, 4, 18-25, http://bgi.omp.obs-mip.fr/index.php/eng/Publications/Newton-s-bulletin/Newton-s-bulletin-No-4.

16. Colombo, O.L., Luthcke, S.B., (2004). Kinematic Point Positioning of a LEO, with Simultaneous Reduced-Dynamic Orbit Estimation. Proceedings ION GNSS 2004, Long Beach, California.

17. Combrinck, L., (2010). Satellite Laser Ranging. In: Xu G, editor. Sciences of geodesy I-Advances and future directions. *Berlin: Springer Verlag*. 301– 336.

18. Combrinck, L., Suberlak, V., (2007). Earth-tide as parameter of crustal motion to correction for SLR station displacement. *South African Journal of Geodegy*. Vol 110:203-210.

19. Coulot, D., Berio, P., Biancale, R., Loyer, S., Soudarin, L., Gontier, A.-M., (2007). Toward a direct combination of space-geodetic techniques at the measurement level: methodology and main issues. *Journal of Geophysical research*. Vol 112, B05410, doi:10.1029/2006JB004336.

20. Cox, C.M., Au, A., Boy, J.-P, Chao, B.F., (2003). Time-variable gravity: Using Satellite-Laser-Ranging as a tool for observing long-term changes in the Earth system. In: Noomen R, Klosko S, Noll C, Pearlman M, editors. Proceedings of the 13th International Workshop on Laser Ranging. Greenbelt, MD: NASA Goddard Space Flight Center.

21. Cox, C.M., Chao, B.F., (2002). Detection of a large-scale mass redistribution in the terrestrial system since 1998. *Science*. 297:831–832. http://dx.doi. org/10.1126/science.1072188, PMid:12161652.

22. Dawod, G., (2008). Towards the redefinition of the Egyptian geoid: Performance analysis of recent geoid models and digital terrain models. *Journal of Spatial Science*. Vol 53 (1):31-42.

23. Degnan, J.J., (1985). Satellite Laser Ranging: current status and future prospects. *IEEE Transactions on Geoscience and remote sensing*. GE-23:398-413.

24. Dickey, J.O., Marcus, S.L., De Viron, O., Fukumori, I., (2002). Recent Earth oblateness variations: Unraveling climate and postglacial rebound effects. *Science*. 298:1975-1977.

25. Dobslaw, H., Schwintzer, P., Barthelmes, F., Flechtner, F., Reigber, C., Schmidt, R., Schoene, T., Wiehl, M., (2004). Geostrophic Ocean Surface Velocities from TOPEX Altimetry,

and CHAMP and GRACE Satellite Gravity Models. Scientific technical report 04/07, GeoForschungsZentrum Potsdam.

26. Dow, J.M, Neilan, R.E., Gendt, G., (2005). The International GPS Service (IGS): Celebrating the 10th Anniversary and Looking to the Next Decade. *Advances in Space Research*. Vol. 36(3):320-326.

27. Eckman, M., (1998). What is the geoid? In: Vermeer M, editor. Coordinate systems, GPS, and the geoid. Report 95:5 of the Finnish Geodetic Institute. Masala: Finnish Geodetic Institute, pp. 49-51.

28. Ellmann, A., (2004). The geoid for the Baltic countries determined by the least squares modification of Stokes' formula. Geodesy Report No. 1061. Stockholm: Royal Institute of Technology, Department of Infrastructure.

29. Eubanks, T.M., (1993). Variations in the orientation of the Earth, in Contributions of Space Geodesy to Geodynamics: Earth Dynamics. *Geodynamic Series*. Vol 24:1-54. Edited by Smith, D.E., and Turcotte, D.L. *American Geophysical Union*,Washington D.C.

30. Featherstone, W.E., (2003). Improvement to long-wavelength Australian gravity anomalies expected from the CHAMP, GRACE and GOCE dedicated satellite gravimetry missions. *Exploration Geophysics*. 34:69-76.

31. Featherstone, W.E., Olliver, J.G., (2001). A review of Geoid Models over the British Isles: progress and proposals. *Survey Review*. 36:78-100.

32. Freedman, A.P., Steppe, J.A., Dickey, J.O., Eubanks, T.M., Sung, L.-Y., (1994). The short-term prediction of universal time and length-of-day using atmospheric angular momentum. *Journal of Geophysical Research*. 99:6981-6996.

33. Foerste, C., Stubenvoll, R., Koenig, R., Raimond, R., Flechtner, J.-C., Barthelmes, F., Kusche, J., Dahle, C., Neumayer, H., Biancale, R., Lemoine, J.-M., Bruinsma, S., (2009). Evaluation of EGM2008 by comparison with other recent global gravity field models. Newton's Bulletin. 4:26-37.

34. Foerste, C., Flechtner, F., Schmidt, R., Stubenvoll, R., Rothacher, M., Kusche, J., Neumayer, K.-H., Biancale, R., Lemoine, J.-M., Barthelmes, F., Bruinsma, J., Koenig, R., Meyer, U., (2008). EIGEN-GL05C – A new global combined high-resolution GRACE based gravity field model of the GFZ-GRGS cooperation. General Assembly EGU, Vienna, Austria, Abstract No. EGU2008-A-06944.

35. Foerste, C., Flechtner, F., Schmidt, R., Koenig, R., Meyer, U., Stubenvoll, R., Rothacher, M., Barthelmes, F., Neumayer, H., Biancale, R., Bruinsma, S., Lemoine, J.-M, Loyer, S., (2006). A mean global gravity field model from the combination of satellite mission and altimetry/gravimetry data, EIGEN-GL04C. *Geophysical Research Abstracts*. 8, 03462.

36. Foerste, C., Flechtner, F., Schmidt, R., Meyer, U., Stubenvoll, R., Barthelmes, F., Rothacher, M., Biancale, R., Bruinsma, S., Lemoine, J.-M., (2005). A new high resolution global gravity field model from the combination of GRACE satellite mission and altimetry/gravimetry surface gravity data. *Geophysical Research Abstracts*. Vol. 7, 04561.

37. Fitzmaurice, M.W., Minott, P.O., Abshire, J.B., Rowe, H.E., (1977). Prelaunching testing of the Laser Geodynamic Satellite (LAGEOS). NASA Technical Paper 1062.

38. Gambis, D., (2004). Monitoring Earth orientation using space-geodetic techniques: state-of-the-art and prospective. *Journal of Geodesy*. 78:295-303.

39. Gross, R.S., Fukumori, I., Menemenlis, D., Gegout, P., (2004). Atmospheric and oceanic excitation of length-of-day variations during 1980-2000. *Journal of Geophysical Research*. 109, B01406, doi:10.1029/2003JB002432.

40. Gross, R.S., (2003). CHAMP, mass displacements, and the Earth's rotation, in first CHAMP mission results for Gravity, Magnetic and Atmospheric studies. *Springer-Verlag*, New York. 174-179. Edited by Reigber, C., Lu¨hr, H. and Schwintzer, P.

41. Gruber, Th., Bode, A., Reigber, Ch., Schwintzer, P., Balmino, G., Biancale, R., Lemoine, J.-M., (2000). GRIM5-C1: Combination solution of the global gravity field to degree and order 120. *Geophysical Research Letters*. 27(24):4005-4008.

42. Gruber, Th., Anzenhofer, M., Rentsch, M., (1997). Improvements in high resolution gravity field modeling at GFZ. In: Proceedings of IAG Symposium No. 117, Gravity, Geoid and Marine Geodesy, Ed. Segawa, Fujimoto, Okubo. *Springer Verlag*. 445-452.

43. Heck, B., (1990). An evaluation of some systematic error sources affecting terrestrial gravity anomalies. Bull Geodesique; 64:88–108. http://dx.doi. org/10.1007/BF02530617.

44. Heiskanen, W.A., Moritz, H., (1967). Physical Geodesy. W.H. Freeman & Co. (USA). 364 pages.

45. Huang, N.E., Shen, Z., Long, S.R., Wu, M.C., Shih, H.H., Zheng, Q., Yen, N.-C. Tung, C.C., Liu, H.H., (1998). The empirical mode decomposition and the Hilbert spectrum for nonlinear and nonstationary time series analysis. *Proceedings of the Royal Society*. London A. 454: 903-995.

46. Huang, C. and Liu, L. (1992) Analytical solutions to the four post-Newtonian effects in a near-Earth satellite orbit. *Celestial Mechanics and Dynamical Astronomy*, 53, 293–307.

47. Hutt, A., Daffertshofer, A., Steinmetz, U., (2003). Detection of mutual phase synchronization in multivariate signals and application to phase ensembles and chaotic data. *Physical Review E*. 68, 036,219.

48. Jaeggi, A., Beutler, G., Mervart, L., (2008). GRACE Gravity Field Determination using the Celestial Mechanics Approach - first results, presented at the IAG Symposium on Gravity, Geoid, and Earth Observation. Chania/Greece.

49. Jevrejeva, S., Grinsted, A., Moore, J.C., Holgate, S., (2006). Nonlinear trends and multi-year cycles in sea level trends. *Journal of Geophysical Research*. 111, C09012, doi:10.1029/2005JC003229.

50. Johnston, K.J., de Vegt, C., (1999). Reference frames in astronomy. *Annual Review of Astronomy and Astrophysics*. 37:97-125.

51. Kaula, W.M., (1966). Theory of satellite geodesy: Applications of satellites to geodesy. Waltham, Mass.: Blaisdell.

52. Kearsley, A.H.W., Forsberg, R., (1990). Tailored geopotential models – applications and shortcomings. Manuscripta geodaetica. 15:151-158.

53. Kiamehr, R., Sjoeberg, L.E., (2005). Comparison of the qualities of recent global and local gravimetric geoid models in Iran. *Studia Geophysica et Geodaetica*. 49:289-304.

54. Kirby, .JF., Featherstone, W.E., Kearsley, A.H.W., (1998) Tests of the DMA/GSFC geopotential models over Australia. International geoid service bulletin; 7:213.

55. Koyama, Y., Kurihara, N., Kondo, T., Sekido, M., Takahashi, Y., Kiuchi, H., Heki, K., (1998). Automated geodetic Very Long Baseline Interferometry observation and data analysis system. *Earth, Planets and Space*. 50:709-722.

56. Laxon, S., (2003). Physics of the Earth. wwwcpg.mssl.ucl.ac.uk/people/swl/lectures.

57. Lemoine, F.G., Kenyon, S.C., Factor, J.K., Trimmer, R.G., Pavlis, N.K., Chinn, D.S., Cox, C.M., Klosko, S.M., Luthcke, S.B., Torrence, M.H., Wang, Y.M., Williamson, R.G., (1998). The Development of the Joint NASA GSFC and the National Imagery and Mapping Agency (NIMA) Geopotential Model EGM96. NASA Technical Paper, NASA/TP-1998-206861:1-98. Goddard Space Flight Center, Greenbelt, USA.

58. Lieske, J. H., Lederle, T., Fricke, W., Morando, B., (1977). Expressions for the precession quantities based upon the IAU /1976/ system of astronomical constants. *Astronomy and Astrophysics*. vol. 58, no. 1-2, p. 1-16.

59. Lieske, J. H., (1979). Precession matrix based on IAU /1976/ system of astronomical constants. *Astronomy and Astrophysics.* vol. 73, no. 3, p. 282-284.

60. Loyns, D., Vaughn, R., (1999). Mars Pathfinder Project: Planetary constants and models. trs-new.jpl.nasa.gov/dspace/bitstream/2014/16962/1/99-0376.pdf.

61. Luceri, V., Bianco, G., (2008). The temporary ILRS reference frame: SLRF2005. ILRS Fall Meeting, 24-28 September 2007. Grasse.

62. Mathews, P.M., Buffett, B.A., Shapiro, I.I., (1995). Love numbers for diurnal tides: Relation to wobble admittances and resonance expansions. *Journal of Geophysical Research*, 100(B9); 9935-9948.

63. Marini, J.W., Murray, C.W., (1973). Correction of laser range tracking data for atmospheric refraction at elevations above 10 degrees. NASA-TM-X-70555, Goddard Space Flight Center, Greenbelt, MD.

64. Mendes, V.B., Pavlis, E.C., (2004). High accuracy Zenith delay prediction at optical wavelengths. *Geophysical Research Letters*. 31:L14602, doi:10.1029/2004GL020308.

65. Mendes, V.B., Prates, G., Pavlis, E.C., Pavlis, D.E., Langley, R.B., (2002). Improved mapping functions for atmospheric refraction correction in SLR. *Geophysical Research Letters*. Vol. 29(10):1414, doi:10.1029/2001GL014394.

66. McCarthy, D.D., Petit, G., (2003). IERS conventions. IERS Technical Note 32, http://www.iers.org/iers/publications/tn/tn32/.

67. Metivier, L., Conrad, C.P., (2008). Body tides of a convecting, laterally heterogeneous, and aspherical Earth. *Journal of Geophysical Research*. Vol. 113:B11405.

68. Milani, A., Carpino, M., Rossi, A., Catastini, G., Usai, S., (1995). Local geodesy by satellite laser ranging: an European solution. *Manuscripta Geodaetica*. 20:123-138.

69. Minott, P.O., Zagwodzki, T.W., Varghese, T., Selden, M., (1993). Prelaunch optical characterization of the laser geodynamic satellite (LAGEOS 2). NASA technical paper, TP-3400.

70. Montenbruck, O., Gill, E., (2001). Satellite Orbits: Models, Methods and Applications. *Springer-Verlag*.

71. Moore P, Zhang Q, Alothman A., (2006). Recent results on the modeling of the spatial and temporal structure of the Earth's gravity field. *Philosophical Transactions of the Royal Society*.;A364:1009–1026. http://dx.doi.org/10.1098/rsta.2006.1751.

72. Motulsky, H.J., (2003). Prism 4 Statistics Guide - Statistical analyses for laboratory and clinical researchers. GraphPad Software Inc., San Diego CA.

73. Nerem, R.S., Eanes, R.J., Thompson, P.F., Chen, J.L., (2000). Observations of annual variations of the Earth's gravitational field using satellite laser ranging and geophysical models. *Geophysical Research Letters*. 27:1783-1786.

74. Neumeyer, J., Barthelmes, F., Dierks, O., Flechtner, F., Harnisch, M., Hinderer, J., Imanishi, Y., Kroner, C., Meurers, B., Petrovic, S., Reigber, Ch., Schwintzer, P., Sun, H.-P., Virtanen, H., (2006). Combination of temporal gravity variations resulting from superconducting gravimeter (SG) recordings, GRACE satellite observations and global hydrology models. *Journal of Geodesy*;79(10–11):573–585. http://dx.doi.org/10.1007/s00190-005-0014-8.

75. Noll, C., (2010). The Crustal Dynamics Data Information System: A resource to support scientific analysis using space geodesy. *Advances in Space Research*. 45 (12):1421 1440, doi: 10.1016/j. asr. 2010.01. 018.

76. Oliveau, S.H., Freedman, A.P., (1997). Accuracy of Earth Orientation Parameter Estimates and Short-Term Predictions Generated by the Kalman Earth Orientation Filter. TDA Progress Report 42-129.

77. Otsubo, T., Sherwood, R.A., Gibbs, P., Wood, R., (2004). Spin motion and orientation of LAGEOS 2 from photometric observation. *IEEE Transaction Geoscience and Remote Sensing*. 42(1):202-208, doi:10.1109/TGRS.2003.817191.

78. Osorio, J.P., (1992). Satellite laser ranging. *Proceedings of SPIE* 1524, 345; doi:10.1117/12.57731.

79. Pail, R., Bruinsma, S., Migliaccio, F., Foerste, C., Goiginger, H., Schuh, W.-D, Hoeck, E., Reguzzoni, M., Brockmann, J.M, Abrikosov, O., Veicherts, M., Fecher, T., Mayrhofer, R., Krasbutter, I., Sanso, F., Tscherning, C.C., (2011). First GOCE gravity field models derived by three different approaches. *Jounal of Geodesy*. 85:819-843

80. Pavlis, N.K., Holmes, S.A., Kenyon, S.C., Factor, J.K., (2008). An Earth Gravitational Model to Degree 2160: EGM2008. EGU, Vienna, Austria.

81. Pavlis, D.E., Poulose, S.G., McCarthy, J.J., (2006). GEODYN operations manuals, contractor report. Stinger Ghaffarian Technol., Greenbelt, Md.

82. Pavlis, N.K., Chinn, D.S., Cox, C.M., Lemoine, F.G., (2000). Geopotential model improvement using POCM_4B dynamic ocean topography information: PGM2000A. Paper presented at the Joint TOPEX/Poseidon and Jason-1 Science Working Team Meeting, Miami, ftp://geodesy.gsfc.nasa.gov/dist/nkp/PGM2000A/pavlis_swt_fall2000.pdf [coefficients available from ftp://geodesy.gsfc.nasa.gov/dist/nkp/PGM2000A/].

83. Pavlis, D.E., Moore, D., Luo, S., McCarthy, J.J., Luthcke, S.B., (1999). GEODYN Operations Manual: 5 volumes. Raytheon ITSS, Greenbelt, MD.

84. Pearlman, M.R., Degnan, J.J. Bosworth, J.M., (2002). The International Laser Ranging Service. *Advances in Space Research*. Vol. 30(2):135-143.

85. Pearse, M.B., Kearsley, A.H.W., (1996). Analysis of EGM models in New Zealand. International geoid service bulletin: 203–213.

86. Petit, G., Luzum, B., (2010). IERS technical note no. 36. ISSN: 1019-4568, http://www.iers.org/TN36/.

87 Petrov, L., (2005). Software sotid for computation of site displacements due to the solid Earth tides, updated pdf documentation 2005.02.11, http://gemini.gsfc.nasa.gov/sotid.

88. Ponsar, S., Dehant, V., Holme, R., Jault, D., Pais, A., Van Hoolst, T., (2003). The core and fluctuations in the Earth's Rotation, in Earth's Core: Dynamics, Structure, Rotation. Edited by Dehant, V., Creager, K.C., Karato, S., and Zatman, S. *American Geophysical Union Geodynamics Series* vol. 31, Washington, D.C., pp. 251-261.

89. Prange L., Jaeggi A., Beutler G., Mervart, L. Dach, R., (2008). Gravity field determination at the AIUB – the celestial mechanics approach. In: International Association of Geodesy Symposia, *Springer-Verlag*, Berlin.

90. Prange, L., Jaeggi A., Beutler G., Dach, R., (2007). Gravity Field Determination at the AIUB the Celestial Mechanics Approach. Poster at the IUGG XXIV General Assembly, Perugia/Italy.

91. Rapp, R.H., (1998). Past and future developments in geopotential modelling: in Geodesy on the Move; Gravity, Geoids, Geodynamics, and Antarctica (Eds. Forsberg, R., M. Feissl and R. Dietrich). *Springer-Verlag* (Berlin). 58-78.

92. Rapp, R.H, Wang, Y.M., Pavlis, N.K., (1991). The Ohio State 1991 Geopotential and Sea Surface Topography Harmonic Coefficient Models. Rep 410, Department of Geodetic Science and Surveying, The Ohio State University, Columbus, Ohio.

93. Reigber, Ch., Schwintzer, P., Neumayer, K.-H., Barthelmes, F., König, R., Foerste, Ch., Balmino, G., Biancale, R., Lemoine, J.-M., Loyer, S., Bruinsma, S., Perosanz, F., Fayard, T., (2003). The CHAMP-only Earth Gravity Field Model EIGEN-2. *Advances in Space Research*. 31(8):1883-1888, (doi: 10.1016/S0273--1177(03)00162-5).

94. Reigber Ch., Balmino, G., Schwintzer, P., (2002). A high quality global gravity field model from CHAMP GPS tracking data and accelerometry (EIGEN-1S). *Geophysical Research Letters* 29(14): 10.1029/2002GL015064.

95. Rizos, C., Stolz, A., (1985). Force modelling for GPS satellites orbits. 1st International Symposium on. Precise Positioning with GPS, Rockville, Maryland, United States of America, 1, 87-98.

96. Rummel, R., Balmino, G., Johannessen, J., Visser, P., Woodworth, P., (2002). Dedicated gravity field missions - principles and aims. *Journal of Geodynamics*. 33:3-20.

97. Ryan, J.W., Clark, T.A., Ma, C., Gordon, D., Caprette, D.S., Himwich, W.E., (1993). Global scale tectonic motions measured with CDP VLBI data, in Contributions of Space Geodesy to

Geodynamics: Crustal Dynamics. Edited by D. E. Smith and D. L. Turcotte. 37-49. *American Geophysical Union*, Washington D.C.

98. Sasaki, M., Hashimoto, H., (1987). Launch and observation program of the experimental geodetic satellite of Japan. *IEEE Transations on geoscience and remote sensing*. vol. GE-25, pp. 526-533.

99. Seago, J.H., (1998). Enhancements toward robust normal point generation. *Proceedings of the 11th International Workshop on Laser Ranging*, Deggendorf, Germany. 80.

100. Scherneck, H.G., (1991). A Parameterised Solid Earth Tide Model and Ocean Tide Loading Effects for Global Geodetic Baseline Measurements, *Geophysical Journal International*, 106, 677-694.

101. Schlueter, W., Himwich, E., Nothnagel, A., Vandenberg, N., Whitney, A., (2002). IVS and its important role in the maintenance of the global reference systems. *Advances in Space Research*. Vol. 30(2):145-150.

102. Schwintzer, P., Reigber, Ch., Bode, A., Kang, Z., Zhu, S.Y., Massmann, F.-H., Raimondo, J.C., Biancale, R., Balmino, G., Lemoine, J.-M., Moynot, B., Marty, J.C., Barlier, F., Boudon, Y., (1997). Long-wavelength global gravity field models: GRIM4-S4, GRIM4-C4. *Journal of Geodesy*. 71:189-208.

103. Schwintzer, P., Reigber, Ch., Massmann, F.-H., Barth, W., Raimondo, J.C., Gerstl, M., Li, H., Biancale, R., Balmino, G., Moynot, B., Lemoine, J.M., Marty, J.C., Boudon, Y., Barlier F., (1991). A New Earth gravity field model in support of ERS-1 and SPOT-2. Final Report to the German Space Agency (DARA) and the French Space Agency (CNES), DGFI München, GRGS Toulouse.

104. Seeber, G., (2003). Satellite Geodesy: Foundations, Methods, and Applications, 2nd edition, New York.

105. Seidelmann, P. K., (1982). 1980 IAU theory of nutation - The final report of the IAU Working Group on Nutation. *Celestial Mechanics*, vol. 27, p. 79-106.

106. Sengoku, A., (1998). A plate motion study using Ajisai SLR data. *Earth Planets Space*. 50:611-627.

107. Sinclair, A.T., Appleby, G.M., (1986). SATAN – Programs for the determination and analysis of satellite orbits for SLR data. SLR Technical Note, No. 9, Royal Greenwich Observatory, Herstmonceux.

108. Smith, D.E., Kolenkiewicz, R., Dunn, P.J., Robbins, J.W., Torrence, M.H., Klosko, S.M., Williamson, R.G., Pavlis, E.C., Douglas, N.B., Fricke, S.K., (1990). Tectonic motion and deformation from satellite laser ranging to LAGEOS. *Journal of Geophysical Research*. 95:22013-22041.

109. Sole, J., Turiel, A., Liebor, J.E., (2007). Using empirical mode decomposition to correlate paleoclimatic time-series. *Natural Hazards and Earth System Science*. 7:299-307.

110. Standish, E.M., (1998). JPL planetary and lunar ephemerides, DE405/LE405. JPL IOM 312. F-98-048.

111. Svehla, D., Rothacher, M., (2004). Kinematic precise orbit determination for gravity field determination. In: Sansò F (ed) A window on the future of geodesy. *Springer*, Berlin Heidelberg New York. 181-188.

112. Tanir, E., Boehm, J., Schuh, H., Tornatore, V., Felsenstein, K., (2006). VLBI Intra-technique combination for Kalman Filter and Least-Squares solutions. Munich, Germany.

113. Tapley, B., Ries, J., Bettadpur, S., Chambers, D., Cheng, M., Condi, F., Poole, S., (2007). The GGM03 Mean Earth Gravity Model from GRACE. *Eos Transactions American Geophysical Union* 88(52), Fall Meet. Suppl., Abstract G42A-03.

114. Tapley, B., Ries, J., Bettadpur, S., Chambers, D., Cheng, M., Condi, F., Gunter, B., Kang, Z., Nagel, P., Pastor, R., Pekker, T., Poole, S., Wang, F., (2005). GGM02 – An Improved Earth Gravity Field Model from GRACE. *Journal of Geodesy*. DOI 10.1007/s00190-005-0480-z.

115. Tapley, B.D., Schutz, B.E. and Born, G.H., (2004a) Statistical Orbit Determination Burlington. Elsevier Academic Press, San Diego.

116. Tapley, B.D., Bettadpur, S., Watkins, M., Reigber, C., (2004b). The Gravity Recovery and Climate Experiment: Mission overview and early results. *Geophysical Research Letters*. 31, L09607, doi:10.1029/2004GL019920.

117. Tapley, B., Watkins, M., Ries, J., Davis, G.W., Eanes, R.J., Poole, S.R., Rim, H.J., Schutz, B.E., Shum, C.K., Nerem, R.S., Lerch, F.J., Marshall, J.A., Klosko, S.M., Pavlis, N.K., Williamson, R.G., (1996). The Joint Gravity Model 3. *Journal of Geophysical Research*. 101 (B12):28029-28049.

118. Tavernier, G., Fagard, H., Feissel-Vernier, M., Le Bail, K., Lemoine, F., Noll, C., Noomen, R., Ries, J.C., Soudarin, L., Valette, J.J., Willis, P., (2006). The International DORIS Service: Genesis and Early Achievements. *Journal of Geodesy*, 80(8-11):403-417.

119. Verhagen, S., (2005). The GNSS integer ambiguities: estimation and validation, NCG. Nederlandse Commissie voor Geodesie, Netherlands Geodetic Commission, Delft, The Netherlands, January 2005.

120. Wahr, J.M., Sasao, T., (1981). A diurnal resonance in the ocean tide and the Earth's load response due to the resonant free “core nutation”. *Geophysical Journal of the Royal Astronomical Society*, 64, pp. 747-765.

121. Wang, G., Chen, X.-Y., Qiao, F.-L., (2010). On intrinsic mode function. *Advances in adaptive data analysis, World scientific.* Vol. 2(3):277-293.

122. Wenzel, H.G., 1998. Ultra-high degree geopotential models GPM98A and GPM98B to degree 1800, Report 98:4, Finnish Geodetic Institute, Masala, 71-80.

123. Willis, P., Jayles, C., Barsever, Y., (2006). DORIS: From orbit determination for altimeter missions to geodesy. Comptes Rendus Geosciences. Vol 338, 14-15, pp. 968-979.

124. Winsemius, H.C., Savenije, H.H.G., Van den Hurk, N.C., Zapreeva, E.A., Klees, R., (2006) Assessment of gravity recovery and climate experiment (GRACE) temporal signature over the upper Zambezi. *Water Resources Research*, 42:2-8.

125. Yoder, C.F., Williams, J.G., Dickey, J.O., Schutz, B.E., Eanes, R.J., Tapley, B.D., (1983). Secular variation of Earth's gravitational harmonic J_2 coefficient from Lageos and non-tidal acceleration of Earth rotation. *Nature*.303, 757 - 762.

126. Yoder, C.F., Williams, J.G., Parke, M.E., (1981). Tidal variations of Earth rotation. *Journal of Geophysical Research*. 86: 888-891.

127. Yilmaz, I., Yilmaz, M., Gullu, M., Turgut, B., (2010). Evaluation of recent global geopotential models based on GPS/leveling data over Afyonkarahisar (Turkey). *Scientific Research and Essays*. 5(5):484-493.

128. Yunck, T.P., (1997). Orbit Determination, in Global Positioning System: Theory and Applications, B. Parkinson and P. Axelrad, eds. *American Institute of Aeronautics and Astronautics*. Vol. 2:567-585

129. Yunck, T.P., Bertiger, W.I., Wu, S.C., Bar-Sever, Y.E., Christensen, E.J., Haines, B.J., Lichten, S.M., Muellerschoen, R.J., Vigue, Y., Willis, P., (1994). First assessment of GPS-based reduced dynamic orbit determination on TOPEX/Poseidon. *Geophysical Research Letters*. Vol. 21(7):541-544.

130. Zhang, K.F., Featherstone, W.E., (1995). The statistical fit of high degree geopotential models to the gravity field of Australia. *Geomatics Research Australas*. 63:1-18.

131. Ziebart, M., (2001). High Precision Analytical Solar Radiation Pressure Modelling for GNSS Spacecraft. PhD thesis, University of East London. 272 pages.

132. Zhaohua, W., Huang, N.E., (2009). Ensemble empirical mode decomposition: a noise-assisted data analysis method. *Advances in data adaptive analysis*. Vol. 1(1):1-41.

133. Zolfaghari, K., Gharebaghi, A., (2008). What is the Gravimeter? Geophysical Research Abstracts, 10, EGU2008-A-08169.

Appendix A5

This appendix presents the O-C time series derived from tidal parameterization tests using LAGEOS 1 and 2 data and the five considered gravity field models.

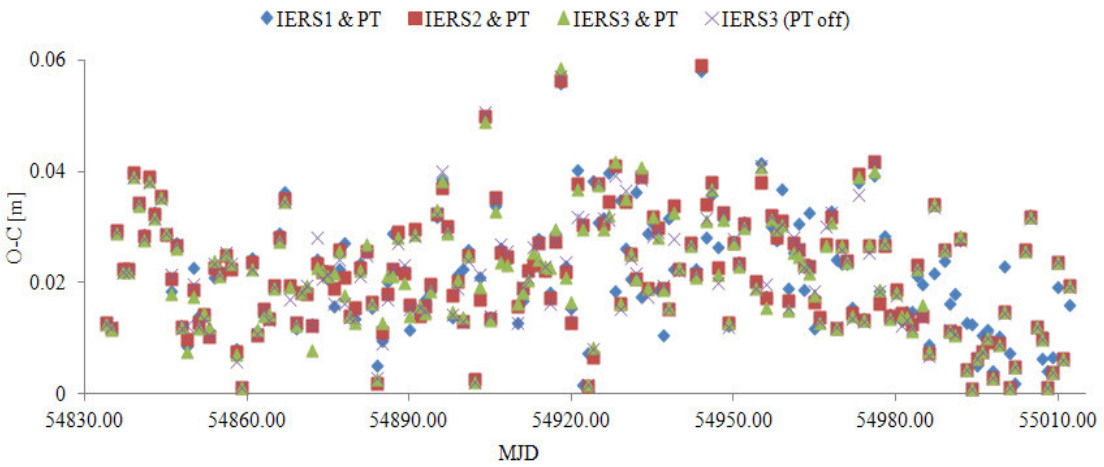

Figure 24: O-C residuals derived from LAGEOS 1 data based on the GRIM5C1 gravity field model.

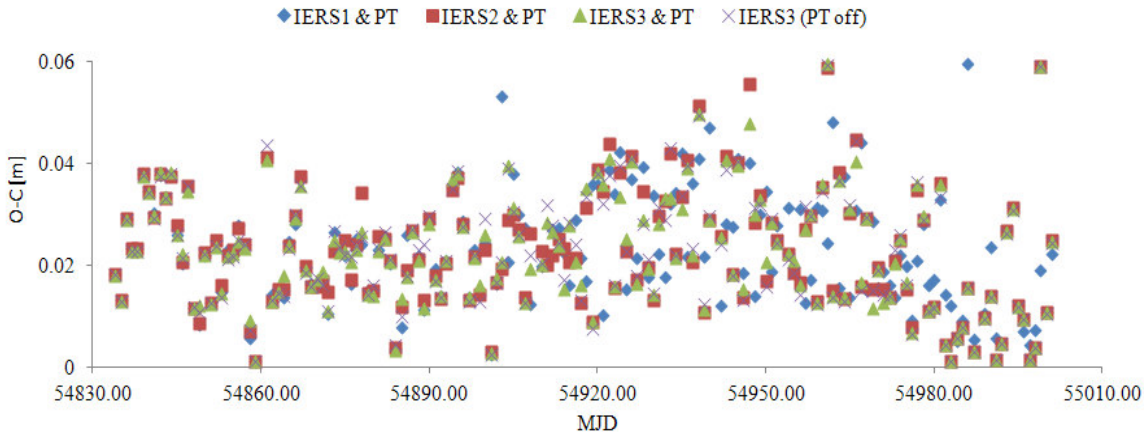

Figure 25: O-C residuals derived from LAGEOS 1 data based on the EIGEN-CG03C gravity field model.

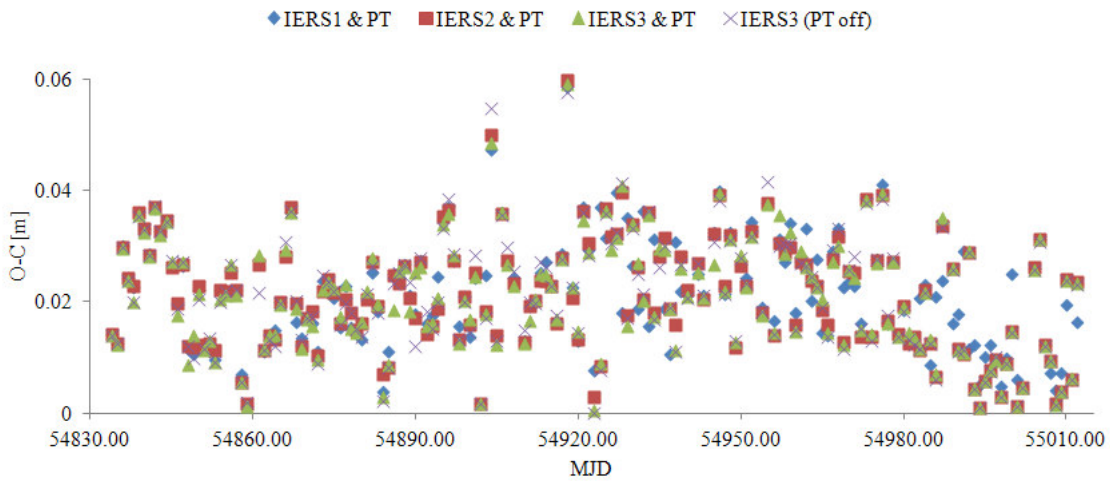

Figure 26. O-C residuals derived from LAGEOS 1 data based on the AIUB-CHAP01S gravity field model.

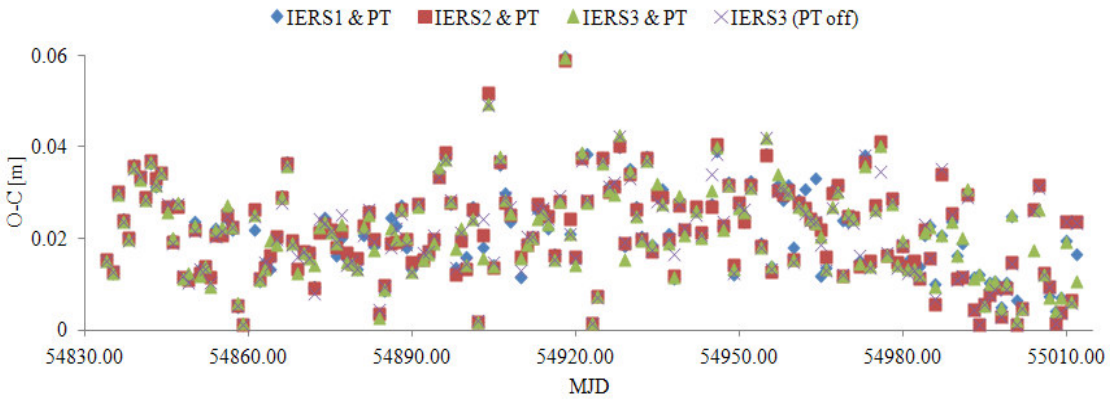

Figure 27. O-C residuals derived from LAGEOS 1 data based on the AIUB-GRACE01S gravity field model.

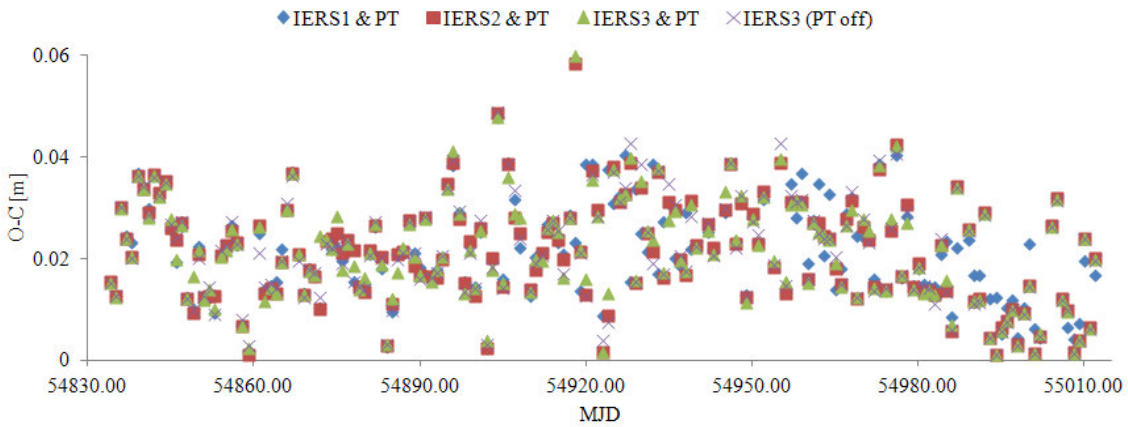

Figure 28. O-C residuals derived from LAGEOS 1 data based on the EGM2008 gravity field model.

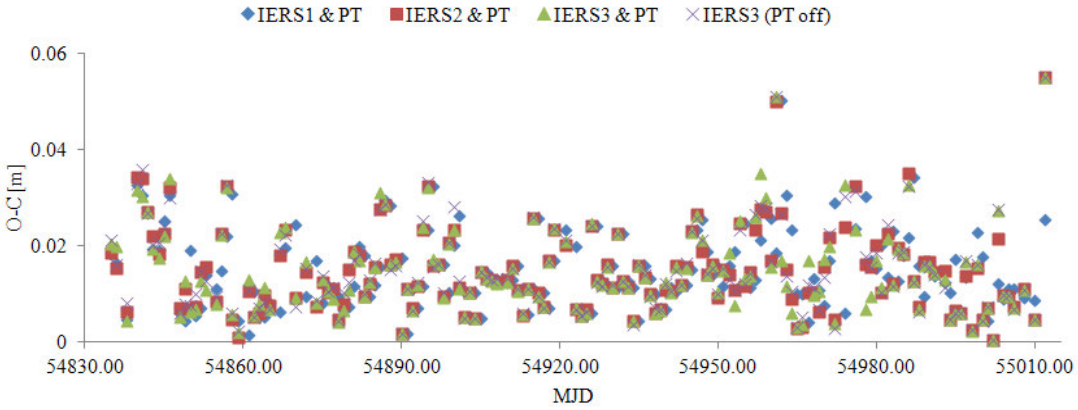

Figure 29. O-C residuals derived from LAGEOS 2 data based on the GRIM5C1 gravity field model.

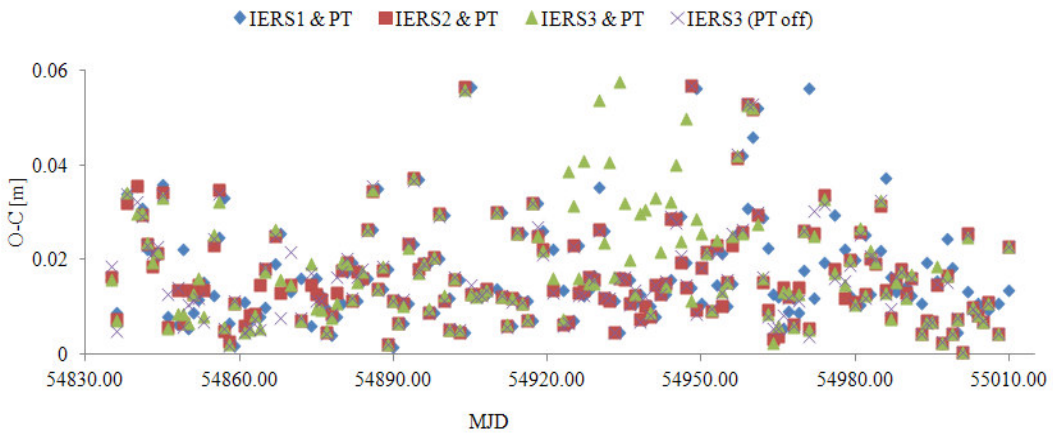

Figure 30. O-C residuals derived from LAGEOS 2 data based on the EIGEN-CG03C gravity field model.

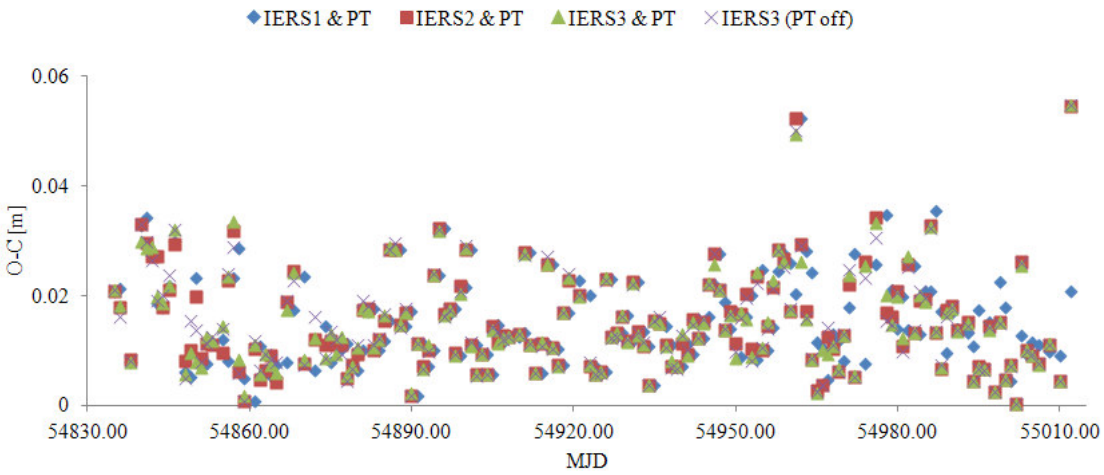

Figure 31. O-C residuals derived from LAGEOS 2 data based on the AIUB-CHAMP01S gravity field model.

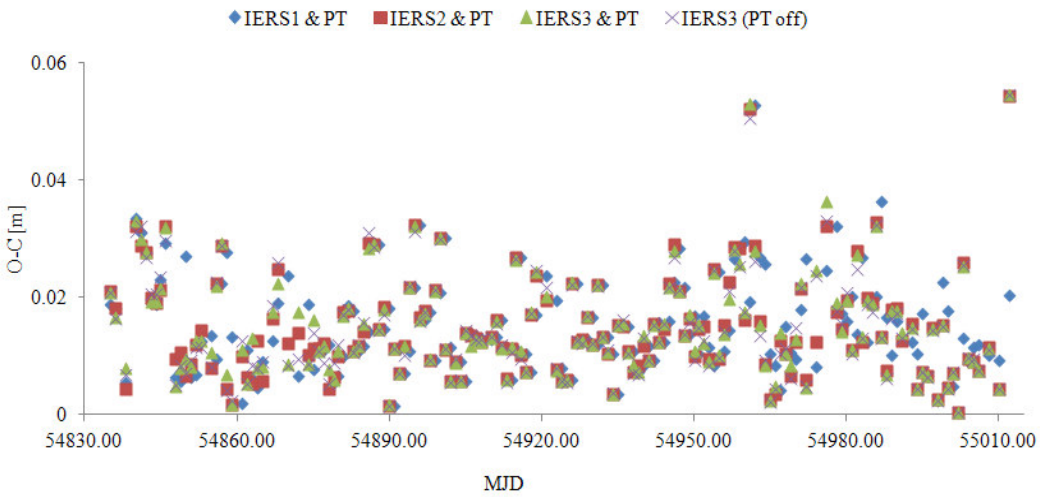

Figure 32. O-C residuals derived from LAGEOS 2 data based on the AIUB-GRACE01S gravity field model.

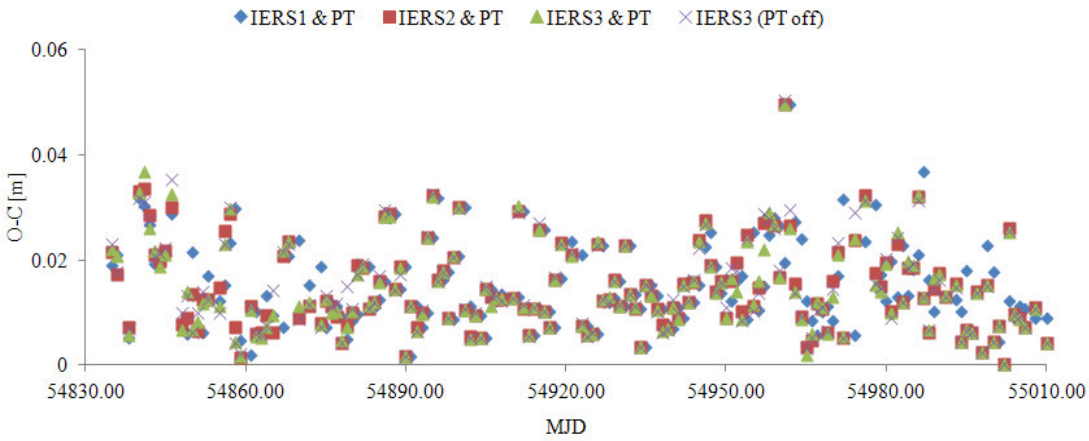

Figure 33. O-C residuals derived from LAGEOS 2 data based on the EGM2008 gravity field model.

Appendix A6

This appendix presents phase synchronizations derived between J_2 and LOD and J_2 and AAM geophysical parameters as discussed in Chapter 6.

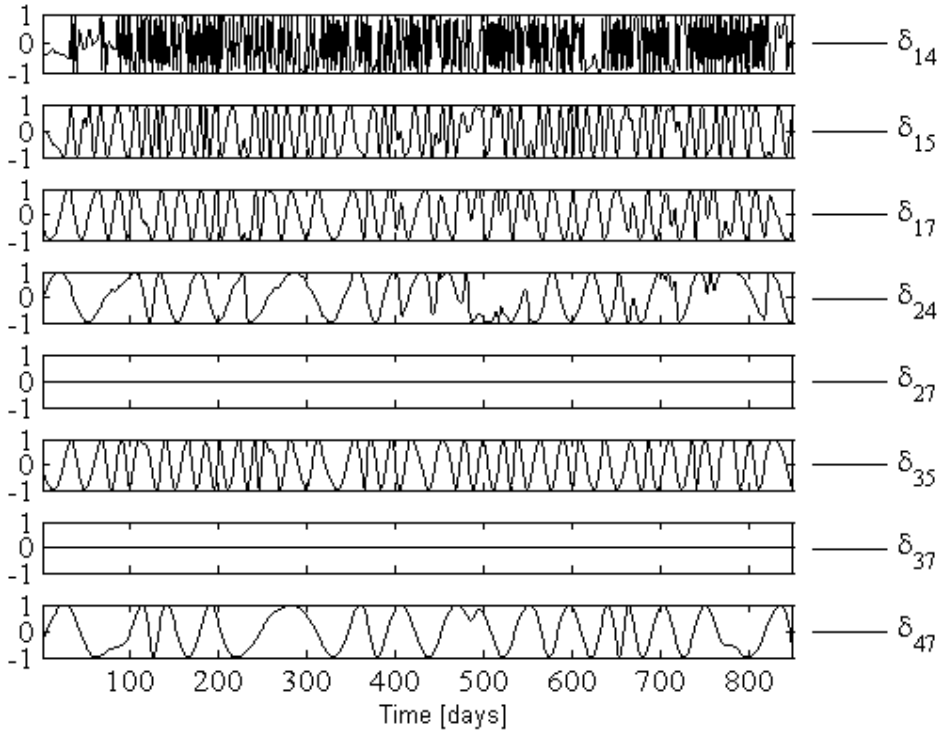

Figure 34. Phase synchronization of J_2 (computed from LAGEOS 1 based on the EGM96 gravity field model) and LOD signals.

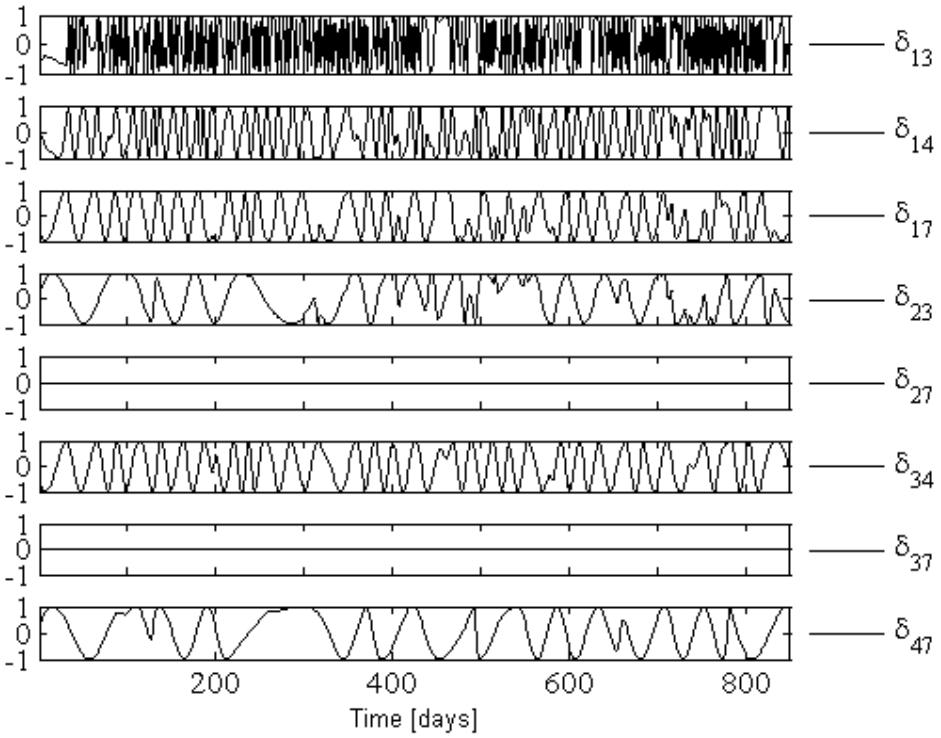

Figure 35. Phase synchronization of J_2 (computed from LAGEOS 1 based on the GRIM5C1 gravity field model) and LOD signals.

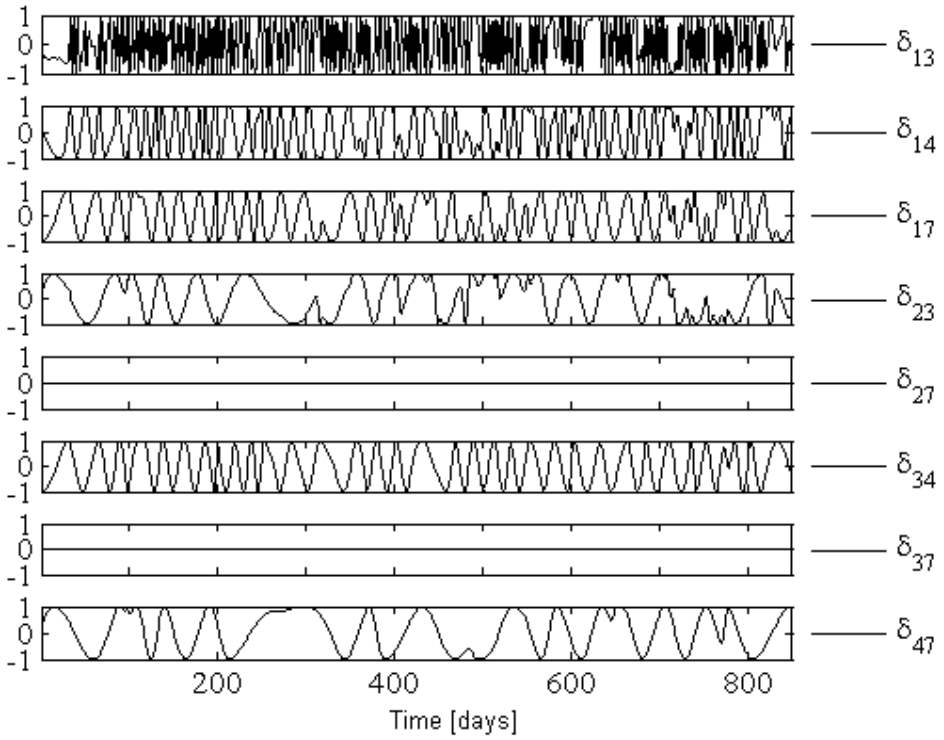

Figure 36. Phase synchronization of J_2 (computed from LAGEOS 1 based on the GGM03C gravity field model) and LOD signals.

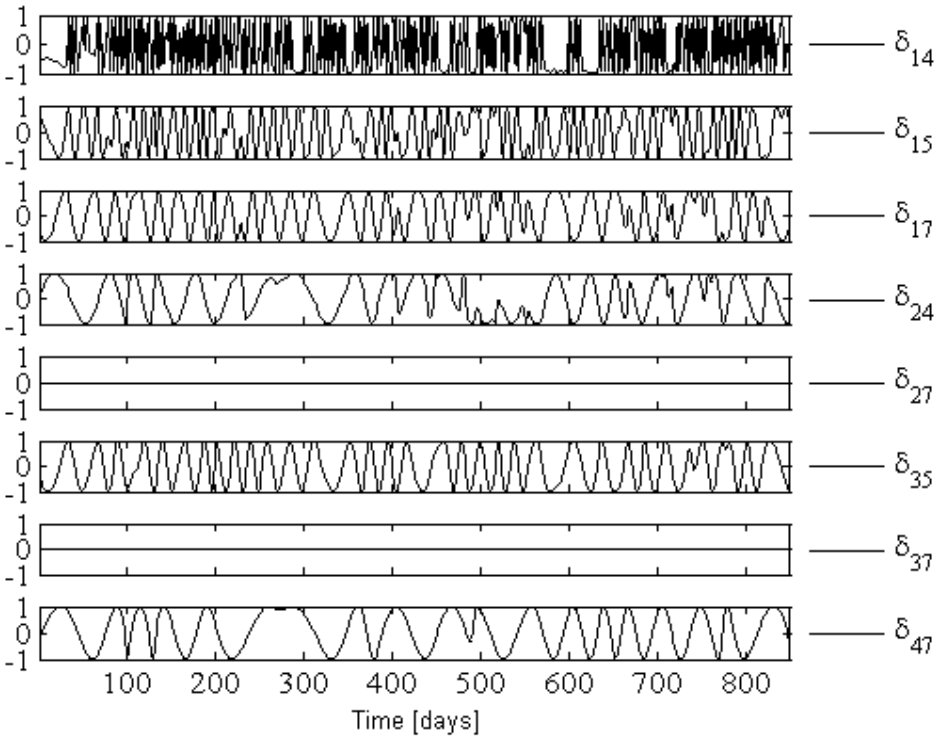

Figure 37. Phase synchronization of J_2 (computed from LAGEOS 1 based on the AIUB-GRACE01S gravity field model) and LOD signals.

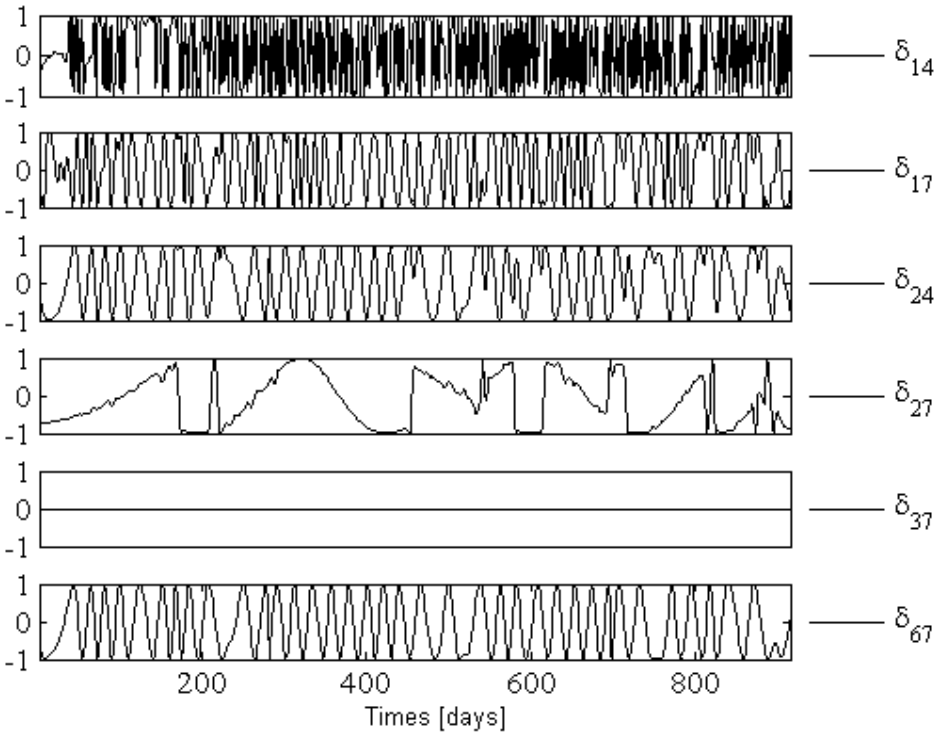

Figure 38. Phase synchronization of J_2 (computed from LAGEOS 2 based on the EGM96 gravity field model) and LOD signals.

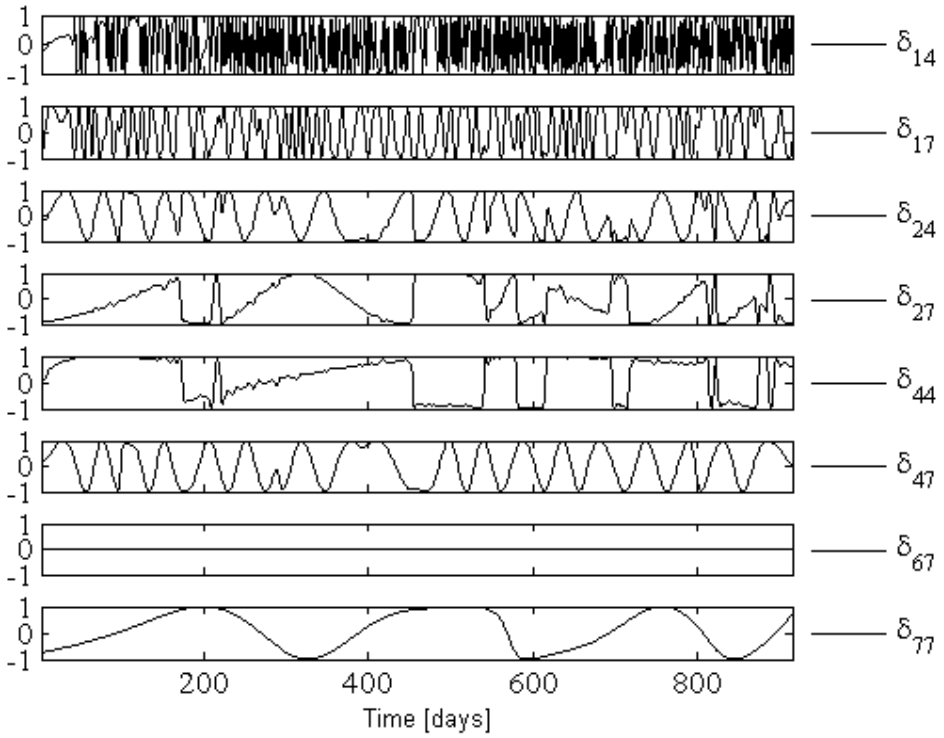

Figure 39. Phase synchronization of J_2 (computed from LAGEOS 2 based on the GRIM5C1 gravity field model) and LOD signals.

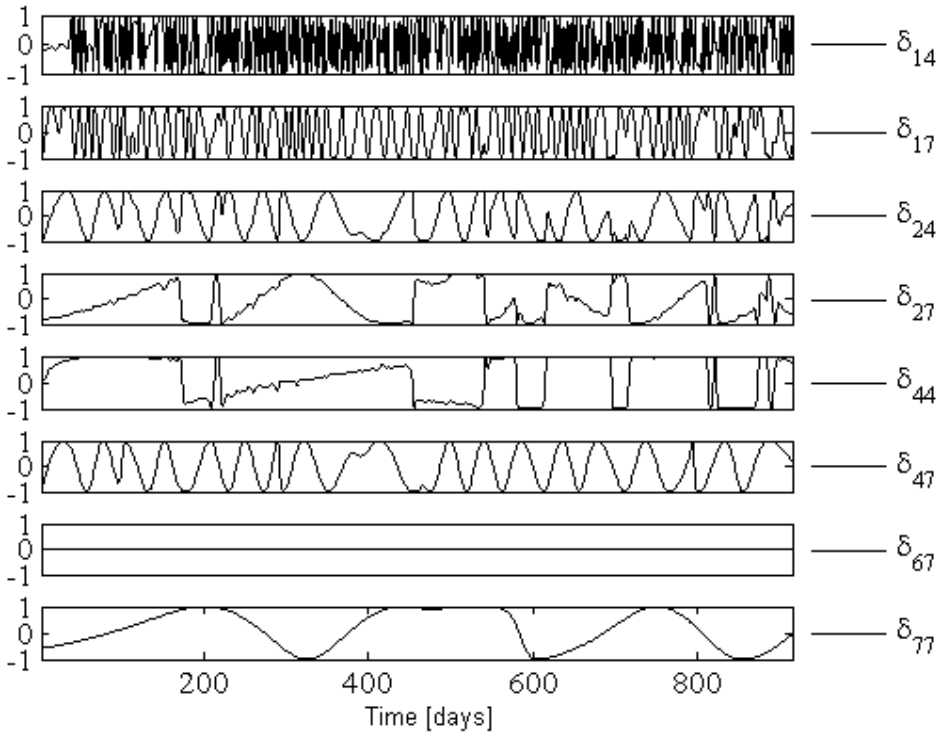

Figure 40. Phase synchronization of J_2 (computed from LAGEOS 2 based on the GGM03C gravity field model) and LOD signals.

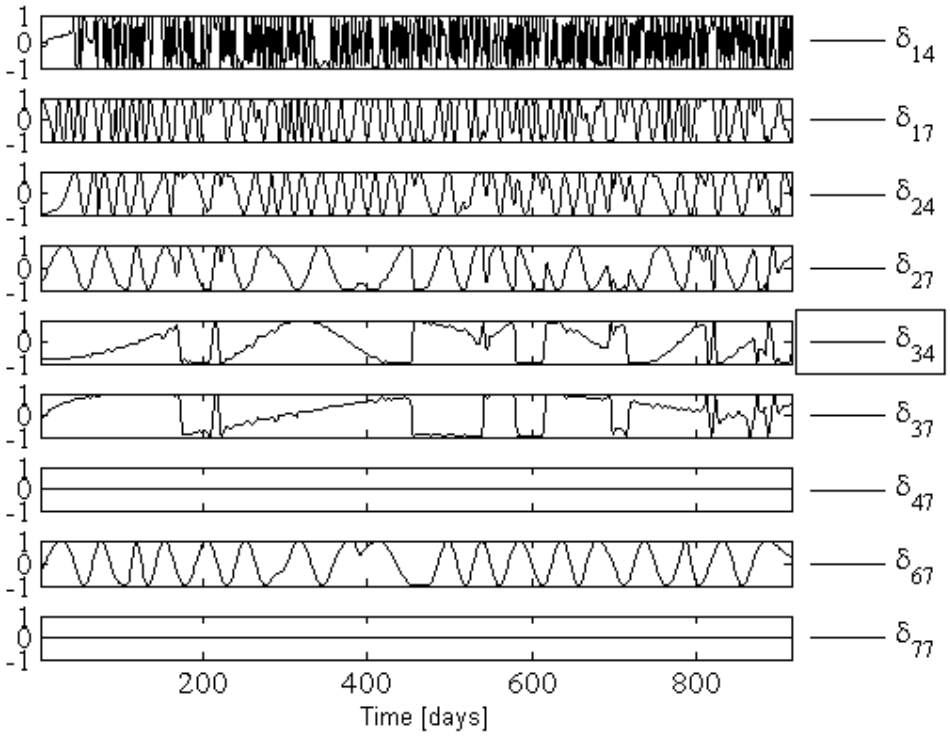

Figure 41. Phase synchronization of J_2 (computed from LAGEOS 2 based on the AIUB-GRACE01S gravity field model) and LOD signals.

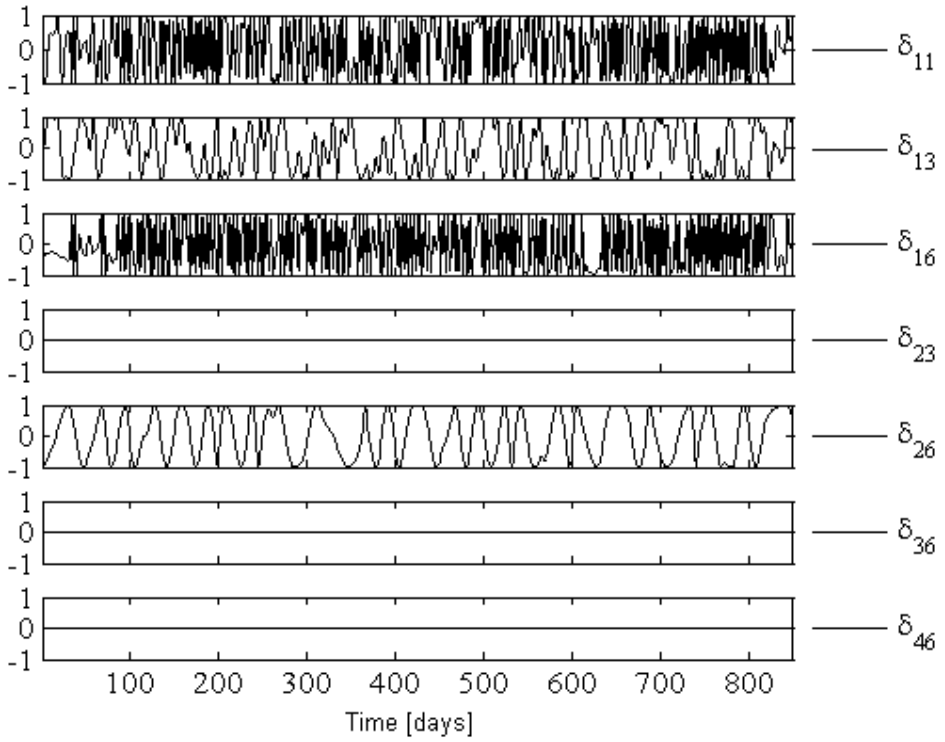

Figure 42. Phase synchronization of J_2 (computed from LAGEOS 1 based on the EGM96 gravity field model) and AAM signals.

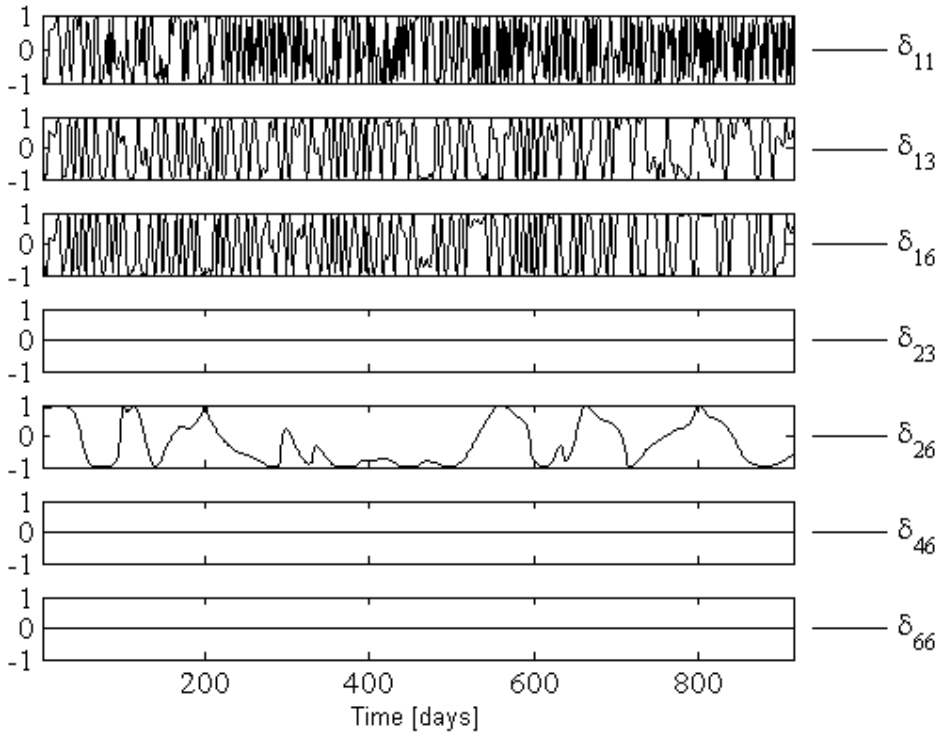

Figure 43. Phase synchronization of J_2 (computed from LAGEOS 1 based on the GRIM5C1 gravity field model) and AAM signals.

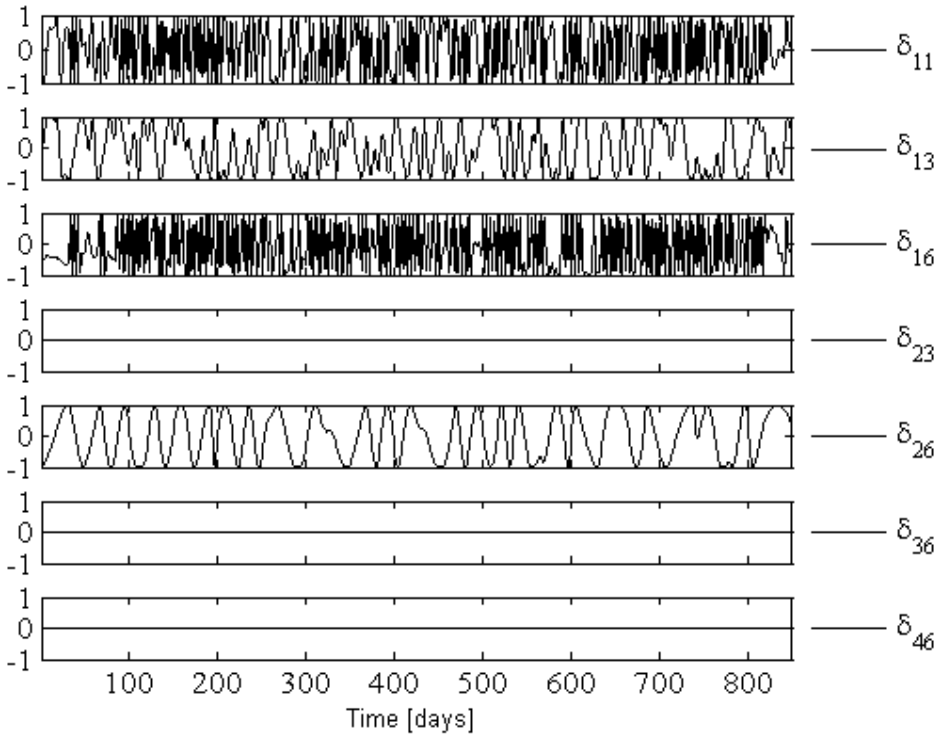

Figure 44. Phase synchronization of J_2 (computed from LAGEOS 1 based on the GGM03C gravity field model) and AAM signals.

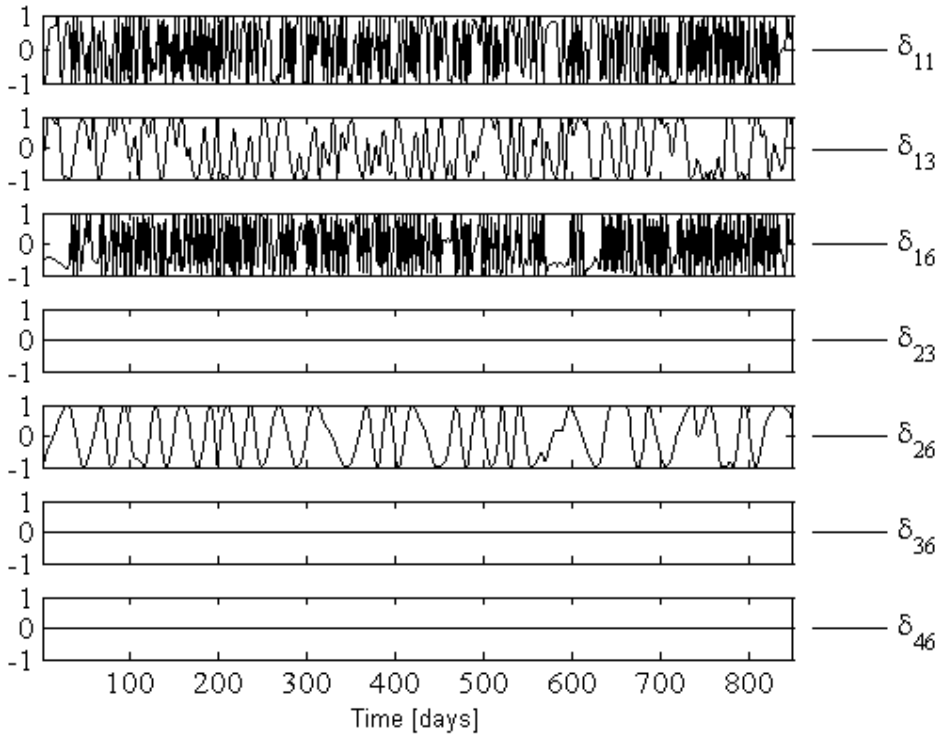

Figure 45. Phase synchronization of J_2 (computed from LAGEOS 1 based on the AIUB-GRACE01S gravity field model) and AAM signals.

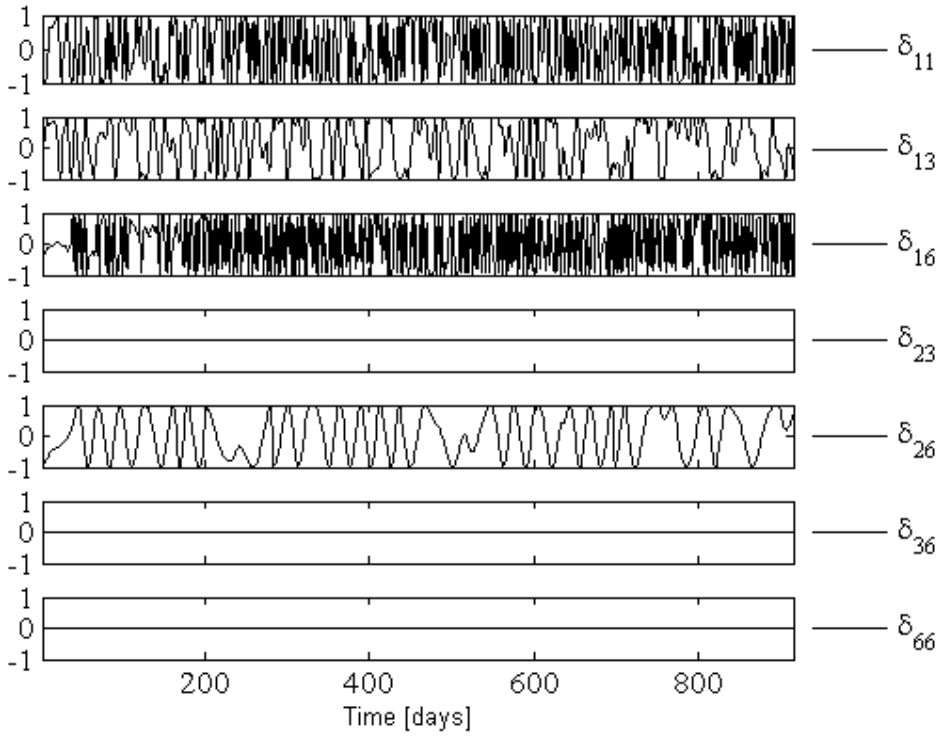

Figure 46. Phase synchronization of J_2 (computed from LAGEOS 2 based on the EGM96 gravity field model) and AAM signals.

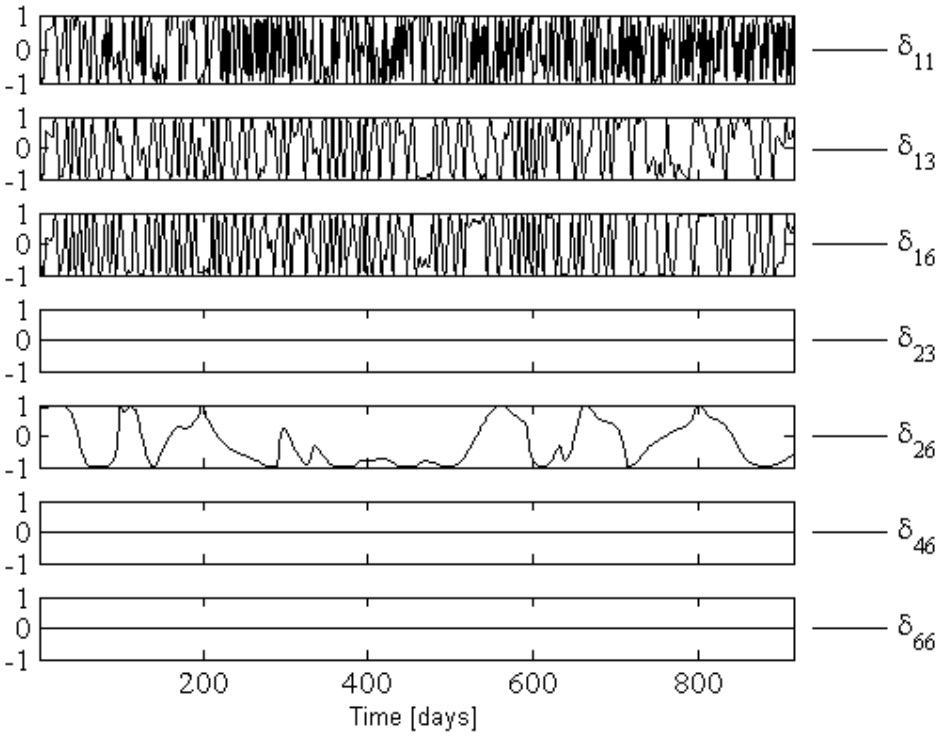

Figure 47. Phase synchronization of J_2 (computed from LAGEOS 2 based on the GRIM5C1 gravity field model) and AAM signals.

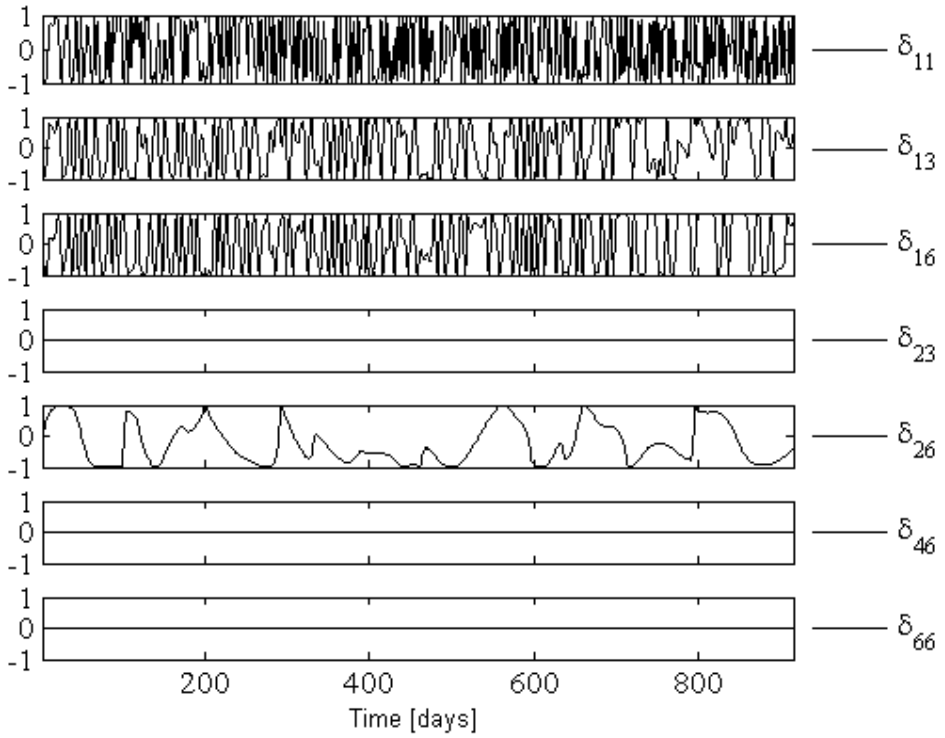

Figure 48. Phase synchronization of J_2 (computed from LAGEOS 2 based on the GGM03C gravity field model) and AAM signals.

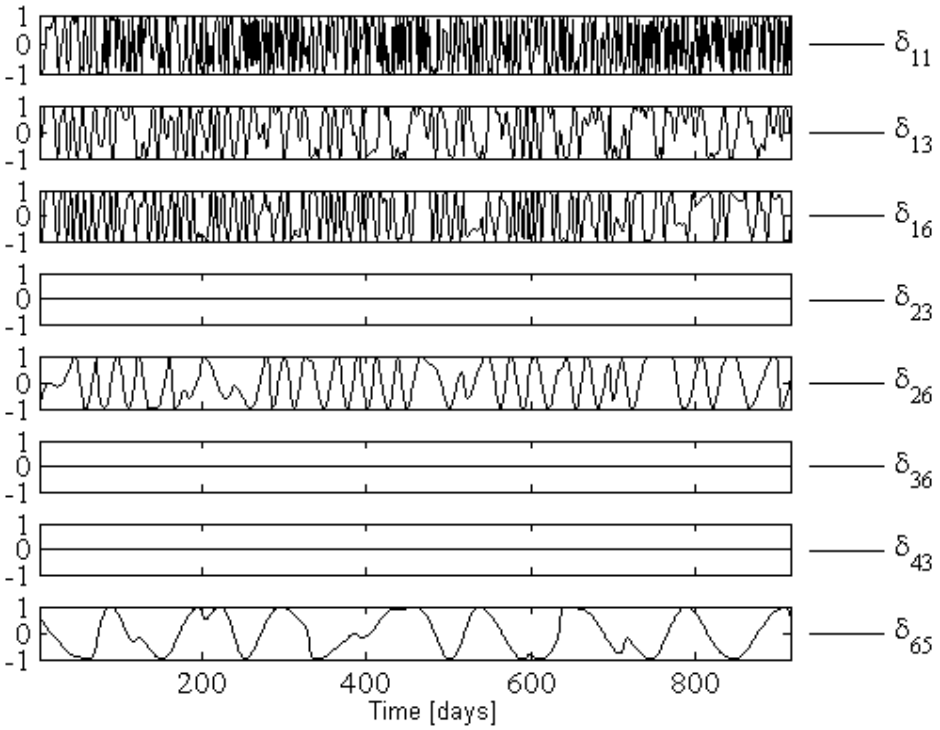

Figure 49. Phase synchronization of J_2 (computed from LAGEOS 2 based on the AIUB-GRACE01S gravity field model) and AAM signals.